Miniaturized Antennas for Platform-level Integration Scenarios

by

Wonbin Hong

A dissertation submitted in partial fulfillment
of the requirements for the degree of
Doctor of Philosophy
(Electrical Engineering)
in The University of Michigan
2009

Doctoral Committee:
Professor Kamal Sarabandi, Chair
Professor Eric Michielssen
Assistant Professor Anthony Grbic
Assistant Professor Max Shtein

To my brother Wonhyung Hong, my mother Misoon Hwang and my father Kyung Hong with love and gratitude.

ACKNOWLEDGEMENTS

Many hands and hearts have contributed to the completion of this studies. I first thank my family, to whom I dedicate this dissertation. They are constant reminders of how fortunate I am.

I am immensely grateful to Dr. Kamal Sarabandi, my advisor and role model. Under his generous and faithful guidance, I have learned about passion, persistence and patience.

I also thank Dr. Eric Michielssen, Dr. Anthony Grbic and Dr. Max Shtein for their support and advice while serving as my dissertation committee members. Sincere thanks are given to Dr. Mahta Moghaddam and Dr. Michael P. Flynn for their kind assistance and encouragements.

A special thanks is extended to Dr. William J. Chappell of Purdue University for his recommendation of the University of Michigan for graduate studies.

I have been extremely fortunate to have worked together with very astute and generous people. Dr. Nader Behdad, Dr. Dan Shi, Dr. DaHan Liao, Young Jun Song and Jongsuek Oh have all taught me many things while we endured countless days and nights in the lab. I will always value these times.

My journey has been a quite life altering experience largely due to the friends I have met along the way. Jorge Pernillo, Ben Chen, Lawrence Wu, Sami Azhari, Mohammed El-Tanani, Razi-Ul Haque, Dr. Karl Brakora, Nathan Falkiewicz, Scott Brumm, Sungwoo Cho and Jae-sun Seo have had a profound impact on my past, present and future. I am certain our friendships will continue well beyond this chapter of my life. Dr. Adib Nashashibi, Dr. Leland Pierce, Michael Thiel, Farhad Bayatpur, Karla D. Johnson, Dr. Xun Gong, Dr.

Hakan Bagci, Khaled Obeidat, Mustafa Rangwala, Dr. Francessco Andriulli, Dr. Mojtaba Dehmollaian, Dr. Alfred Xinen Zhu, Dr. Jia-Shiang Fu, Jane Whitcomb, Danial Ehyaie, Dr. Alireza Tabatabaeenejad, Yuriy Goykhman, Ju Seop Lee, Dr. Sang June Park, Dr. JunYoung Park, Dr. Jonghoon Choi, Line van Nieuwstadt, Nicole Campbell, Jackie Vitaz, Mehrnoosh Vahidpour, Dr. Amelia Buerkle, Adel Elsherbini, Olupelumi Osoba, and Hatim Bukhari have been key members of the family at the University of Michigan. Thanks to them, my days here were never uninteresting. I also express gratitude to friends and colleagues I am most certain I have left out with a mixture of sincere regret. Nevertheless, having met these people is by far the most treasured memories of this journey.

Wonbin

Spring, 2009,

Ann Arbor.

TABLE OF CONTENTS

LIST OF TABLES

Table

LIST OF FIGURES

Figure

CHAPTER 1

Introduction

1.1 Motivation

Antenna enables wireless signal transmission and reception through radiative coupling. In conjunction with advances in high-speed integrated circuits, packaging, power management etc., antenna has been the catalyst in the growth of wireless communication. In applications ranging from wireless handheld devices to satellite communication systems, an antenna can never be omitted. These antennas can generally be classified into two types based on their functional mechanism - resonant antenna (i.e. standing wave antenna) and non-resonant antenna (i.e. traveling wave antenna). The resonant antenna is the most fundamental type of an antenna. Electromagnetic resonance occurs when a sinusoidal current distribution is created across the aperture of a resonant antenna [1]. To satisfy the the electromagnetic resonance condition, dimension of a resonant antenna must be a fraction of its wavelength at resonance. Thus, as the operational frequency of a resonant antenna increases, the dimension decreases accordingly. A number of resonant antennas can be interconnected to form a non-resonant antenna which is typically multiple wavelengths in dimension. Naturally, the two antenna types exhibit very different behavior from one another. The selection criteria between the two is based on the application of the wireless communication system is to operate. This dissertation focuses on the study of resonant

antennas for a series of application scenarios. Therefore resonant antenna will henceforth be addressed as antenna.

Since the ”Birth of Radio” in the late nineteenth century, wireless communication frequency spectrum has rapidly expanded. In the beginning, the majority of application scenarios were concentrated in the LF, MF, and HF bands. Consequently, antennas have historically appeared to be the largest component in a wireless communication device. Such tendency continues to remain intact even in present day, where sophisticated wireless communication devices are extensively used in much higher frequency bands ranging up to microwave frequencies and beyond. This can be largely attributed to increasingly miniaturized and integrated wireless communication components, leaving the reduced antenna dimension still relatively bulky and large in comparison. An antenna protruding from a surface of a wireless communication device or a system platform remains a common sight as shown in Figure 1.1. Accepting such protrusion of the antenna has been widely regarded as a bothersome necessity. The significant profile of these antennas adversely effects important factors of the device such as usability, packaging, ergonomics and design. Therefore, antenna miniaturization is imperative in the present day Information Era where wireless communication devices are omnipresent.

1.2 Approach

Studies regarding antenna miniaturization can generally be categorized into two methods: 1) Miniaturizing the antenna topology using space filling compression technique and 2) Antenna miniaturization using magneto-dielectric materials. The two methods are visualized in Figure 1.2. The first method involves reducing the physical dimension of the antenna by modifying the antenna topology. For instance, a variety of space filling compression techniques have been studied to reduce the vertical profile of monopole antennas [2, 3, 4]. The dimension of a wire monopole antenna is greatly reduced by folding the

Figure 1.1: Commonly used antennas for wireless communication scenarios.

monopole antenna geometry through several iterations. However, the height reduction using these techniques are limited to $\lambda/5$ or larger. In [5, 6] various fractal antennas are further investigated and the resonant properties, bandwidth, and the impedance matching of compressed omnidirectional antennas are reported.

The second approach involves achieving antenna miniaturization through loading the antenna with relatively high permittivity and/or high permeability materials [7, 8]. Traditionally, high permittivity materials have been used to decrease the dimension of the antenna. In [9], a planar inverted F antenna is loaded with high permittivity material for size reduction purposes. Externally perforated high dielectric constant substrates are implemented to miniaturize the dimensions of patch antennas in [10]. In addition, artificial high-permeability materials have been proposed to further decrease the antenna dimension while realizing enhanced bandwidth. Such materials are usually designed by introducing a resonant type circuit in a dielectric material. As a result, the artificial material tends to behave as a magnetic material over a certain frequency band. For instance, in [11], electromagnetic band-gap (EBG) structures utilizing magneto-dielectrics have the dual benefit of

improving band-gap rejection levels while achieving size reduction.

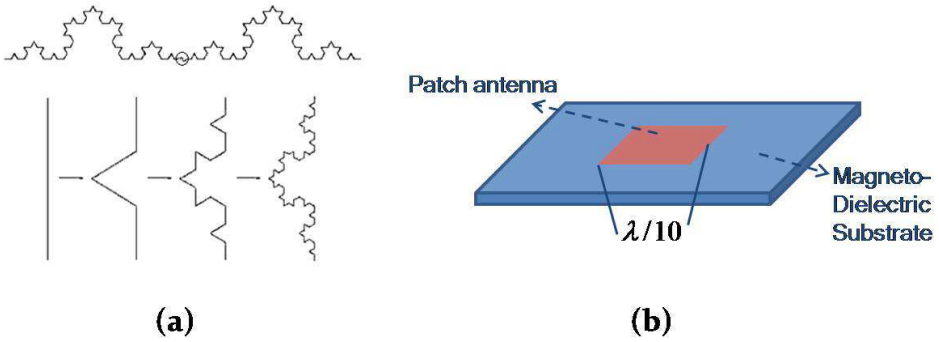

Figure 1.2: Traditional antenna miniaturization methods. (a) Space filling compression technique. (b) Magneto-dielectric materials.

The reduced real estate of antenna geometries have eased the integration task of antennas on wireless communication devices and platforms. However, significant changes in antenna behavior is typical when an antenna is placed in close proximity to nearby structures. For instance, a drastic deterioration of input impedance matching is observed in Figure 1.3. Such phenomenon has resulted in the emergence of platform-level embedded antennas in recent years. A variety of system-level embedded antenna designs have been reported for various application scenarios ranging from health care to Radio Frequency Identification (RFID) [12, 13]. In [14] a folded dipole is design to feature sufficient radiation efficiency despite operating very close to a conductive platform. A slotted waveguide planar antenna is embedded into the vehicle roof for receiving satellite TV while the vehicle is in motion in [15]. For consumer electronics, an embedded quad-band Wireless Local Area Network (WLAN) antenna for laptop antenna has been reported [16]. It is anticipated that the demand for full-level integration of miniaturized antennas will continue to grow as wireless communication continues to mature.

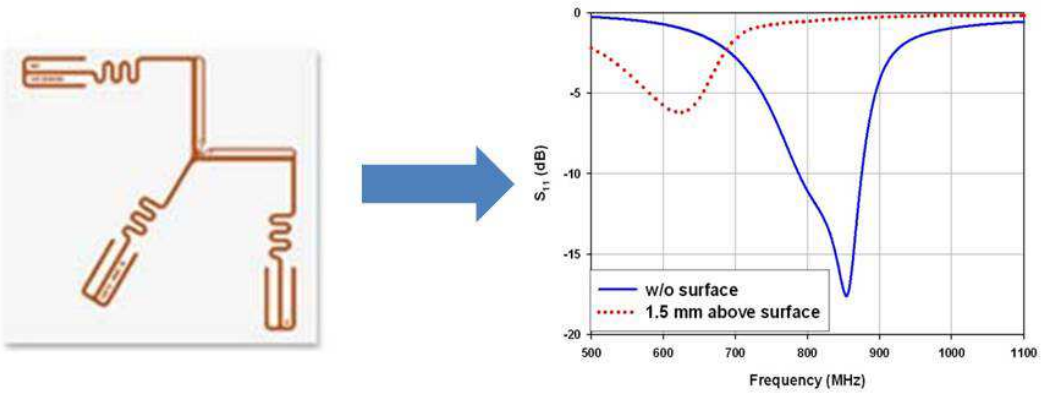

Figure 1.3: Effect of conductive surface on the input impedance of a commercial RFID antenna

1.3 Dissertation Overview

This dissertation introduces a variety of antenna miniaturization methods for platform-level integration scenarios. Like any other 'solution', antenna miniaturization and integration are intrinsically dependant on the 'problem'. In this instance, the problem can be defined as an application scenario for a wireless communication system. An application scenario specifies the required performance parameters, shown below for miniaturized antennas.

- Polarization: To ensure reliable signal transmission and reception, antenna polarization is specified for a majority applications, ranging from terrestrial communications, ad-hoc networks to polarimetric synthetic aperture radar (SAR). When communicating with an unknown transceiver such as RFID, linear polarizations are typically used.

- Bandwidth: The theoretical relationship between bandwidth and dimension of a resonant antenna has been established by Chu [17]. Depending on the application scenario, a miniaturized antenna with a narrow or wide bandwidth is required. For example, for Unattended Ground Sensor (UGS) networks used for perimeter security and area surveillance, a relatively low data rate is sufficient. Thus a narrow-band minia-

turized antenna is preferred. In contrast, transmission and reception of multimedia signals such as voice, video and Global Position Systems (GPS), require higher data rates and therefore demanding increased antenna bandwidths.

- Pattern: For an a priori located wireless communication device, it is beneficial to design an antenna with a pattern that is directive in the known direction. However for application scenarios where the wireless communication device is to operate in an unknown environment, an omnidirectional antenna is advantageous.

Once the required performance parameters are established, an approach to miniaturize and integrate the antenna with the wireless communication platform is devised. The details of the approaches that are used in this dissertation is outlined in the following sub-sections.

1.3.1 Chapter 2: The Miniaturized Cavity-backed Slot Antenna

A technique for reducing the dimensions of the cavity of a cavity-backed slot antenna is presented. This method facilitates proper fabrication and integration of miniaturized slot antennas on multi-layer substrates. This is accomplished by replacing the solid metal around the traditional slot antennas with a specific metallic pattern that can be viewed as a series of parallel strip lines placed around the slot antenna. This metallic pattern is then modified by designing the parallel strips in a compact fashion to reduce the overall antenna dimensions and obtain a reduced-size cavity-backed slot antenna. It is shown that, for a simple straight slot antenna, the overall occupied volume of the modified cavity backing the slot antenna can be reduced by more than 65% without effecting the high radiation efficiency of the antenna. A number of traditional cavity backed slot antennas and the proposed modified cavity backed slot antennas are designed, fabricated, and measured. The reduced-size cavity-backed slot antennas show a very low input VSWR, low cross polarized radiation levels, and high radiation efficiency. Despite their small ground plane, the proposed cavity backed slot antennas have front-to-back ratio (FTBR) values in the

range of 6-7 dB.

1.3.2 Chapter 3: Platform Embedded Slot Antenna backed by Shielded Parallel Plate Resonator

The objective of devising an electrically small cavity-backed slot antenna in Chapter 2 is further investigated. A new cavity architecture for applications in design of resonator-backed slot antennas with a height less than $\lambda/15$ profile is presented. This architecture renders cavity heights as low as $\lambda/130$ and small lateral dimensions. Miniaturization of the supporting cavity resonator is achieved by meandering the passage from the bottom of the cavity resonator to the slot aperture. Unlike conventional cavity resonators, the proposed design operates in a TEM mode which allows for wider bandwidth operation and miniaturization of lateral dimensions. Ultrasonic consolidation technique is employed to fabricate the complicated cavity structure monolithically. Measurements verify the proposed antenna exhibits excellent gain and FTBR. Wide-band mode of the antenna is achieved by using a carefully designed microstrip feed across the slot aperture which facilitates a fictitious short along the slot aperture. The antenna is then flush-mounted onto an arbitrarily built metallic platform and is shown to feature consistent impedance matching. The FTBR is found to improve when the antenna is embedded into the platform. The same antenna architecture is redesigned for VHF band operation using standard multi-layer PCB technology and consistent functionality is verified.

1.3.3 Chapter 4: The Cavity-backed Composite Slot Loop Antenna (CBCSLA)

For near-ground wave propagation applications where both the transmit and receive antennas are placed near the surface of the earth, it is shown that propagation path loss for vertically oriented antennas is by many orders of magnitude lower than any other an-

tenna orientation configuration. For air or ground vehicle applications it is beneficial to use low-profile antennas that can produce vertical polarization with omni-directional radiation pattern. Also for applications such as network of Unattended Ground Sensors, low-profile antennas are highly desired. As wireless communication devices continue to evolve, the large dimension of the antenna is frequently problematic.

In Chapter 4, a novel miniaturized cavity-backed composite slot loop antenna with low profile and omnidirectional radiation similar to a short dipole is presented. The antenna displays vertical polarization while having less than $\lambda/100$ dimension in height. The geometry of the antenna is inspired by a small magnetic loop which is realized using a slot configuration on metallic ground. Since a small slot loop antenna cannot be impedance matched, a composite geometry is devised that acts like as a small slot loop and can easily be impedance matched in this configuration. The diameter of the CBCSLA can be made as smaller than $\lambda/10$. The feeding mechanism is designed such to create a circumferentially-constant current distribution around the composite loop while effectively matching to a 50Ω coaxial feed from the antenna center. Additional methods are discussed to further enhance the bandwidth and achieve a dual-band response. The antennas are designed, fabricated, and measured. It is shown that despite their small lateral dimension and extremely small height, the miniaturized cavity-backed slot loop features extremely good input impedance match, uniform radiation pattern, low cross-polarization levels and expected gain.

1.3.4 Chapter 5: The Multi-element Monopole Antenna

In continuation of Chapter 4, a low-profile, electrically small antenna with omnidirectional vertically polarized radiation similar to a short monopole antenna is presented. The antenna exhibits less than $\lambda/40$ dimension in height and $\lambda/10$ or smaller in lateral dimension. The antenna is matched to a 50Ω coaxial line without the need for external matching. The geometry of the antenna is derived from a quarter-wave transmission line resonator fed at an appropriate location to maximize current through the short-circuited end. To improve

radiation from the vertical short-circuited pin, the geometry is further modified through superposition of additional resonators placed in a parallel arrangement. The lateral dimension of the antenna is miniaturized by meandering and turning the microstrip lines into the shape of a multi-arm spiral. The meandering between the short-circuited end and the feed point also aids in the impedance matching. Through this technique, spurious horizontally polarized radiation is also minimized and a radiation pattern similar to a short dipole is achieved. The antenna is designed, fabricated and measured. Parametric studies are performed to explore further size reduction and performance improvements. Based on these studies, a dual-band antenna with enhanced gain is realized. The measurements verify that the proposed fabricated antennas feature excellent impedance match, omnidirectional radiation in the horizontal plane and low levels of cross-polarization.

1.3.5 Chapter 6: Applications of the Multi-element Monopole Antenna

In Chapter 6, the Multi-element monopole antenna introduced in Chapter 5 is integrated with a wireless communication platform for two separate application scenarios. In the first application, the multi-element monopole antennas are redesigned at 2.45 GHz to realize a Small radio repeater. Two identical antennas are fabricated to form receiving and transmitting antennas. The Small radio repeater consists of two electrically small, vertically polarized antennas and an amplifier. The signal received from the receiving antenna is amplified before retransmitting the signal via the transmitting antenna. The Small radio repeater is fabricated monolithically and features a compact and sturdy geometry. The measured gain indicates the design antenna meets the required wireless link budget.

In the second application, the multi-element monopole is redesigned and fully integrated onto a 2.45 GHz RF front-end transmitter circuitry. The integration of the multi-element monopole antenna greatly reduces the overall volume of the RF transmitter, designed for in-door image transmission. The effects of the Printed circuit board (PCB)

layout of the RF front-end circuitry is considered during the antenna design process. Measurement confirms good agreement with computer simulations of the designed antenna.

1.3.6 Chapter 7: Frequency Reconfigurable Miniaturized Antenna

In Chapter 7, a compact multi-band antenna with electronic frequency tuning capability is designed and measured. Due to its operational frequency and miniaturized dimension, the antenna can be used as an active RFID antenna. The geometry of the antenna is confined within a 50 $mm \times 50$ mm platform, several orders smaller compared to conventional active RFID antennas. The presented antenna operates at 430 MHz, 900 MHz, and 2.45 GHz band and displays a wide operational bandwidth utilizing both capacitive loading and fictitious short circuit technique. Frequency tuning capability is achieved through the implementation of varactor diodes on the antenna topology. Operating frequency of the antenna can be controlled by controlling the DC bias voltage of the varactor diode. The antenna consists of three sub-level antennas with separate connectors allowing for ease of frequency band selection via a switching network. The measured tri-band reconfigurable antenna has very low input VSWR, high levels of port-to-port isolation and sufficient gain.

CHAPTER 2

The Miniaturized Cavity-backed Slot Antenna

2.1 Introduction

The electric field distribution of slot antennas can be derived from complementary wire antennas as established by Booker's extension of Babinet's principle [1]. In scenarios where the slot is cut in an electrically large metallic surface, the average electric current density for slot antennas is generally lower than that of its counterparts, wire antennas. This translates to slot antennas featuring higher bandwidth and efficiency compared to wire antennas. This comparison remains fairly consistent as the dimension of the antennas becomes smaller, as shown in a recent study that miniaturized slot antennas have higher bandwidth and efficiency compared to electrically small wire type antennas [18]. A number of different techniques for designing highly efficient miniaturized slot antennas have been reported [18, 19, 20, 21].

One drawback of slot antennas, is their inherent bi-directional radiation. In many applications, the antenna needs to be located in close proximity to earth or conductive bodies, be mounted on a platform, or be integrated with the rest of the transceiver in a multi-layer structure. Traditionally to alleviate the adverse effect of the interactions between a slot antenna and the structures behind it, a shallow cavity is placed behind the slot antenna as depicted in Figure 2.1.

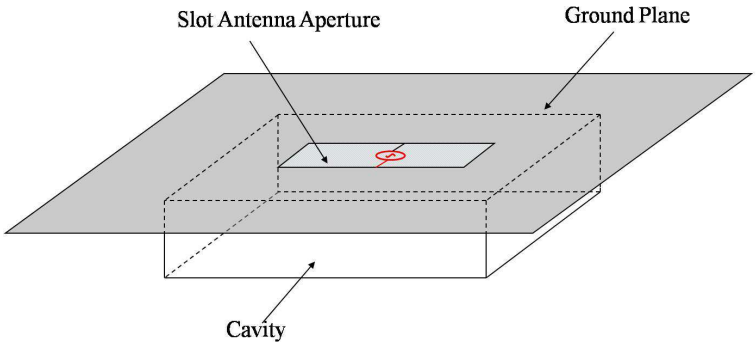

Figure 2.1: Cavity-backed slot antenna.

Cavity-backed slot antennas (CBSA) are among the most basic types of aperture antennas and have been extensively studied both analytically and experimentally [22]. The admittance of a rectangular slot antenna, backed by a rectangular cavity has analytically been derived in [23] and experimentally verified in [24]. In [25], the admittance of a cavity-backed slot antenna (CBSA) is mathematically related to the admittance of an ordinary slot antenna, the results are later experimentally verified in [26]. Aperture field and circuit parameters of CBSA have also been investigated [27]. Size reduction of the CBSA is achieved through dielectric and ferrite loading in the cavity. Experimental results are compared to theoretical values for such loading techniques in [28]. In addition to its basic form, variations of the ordinary CBSAs have been used for a number of different applications. In particular, active and circularly polarized CBSA designs have been studied [29, 30]. In [31], wider slot geometry backed by a cavity is used to increase the bandwidth. In another attempt to increase the bandwidth and directivity of the naturally narrow-band CBSAs, a log-periodic arrangement is considered in [32] to achieve a wideband end-fire CBSA that has a fractional impedance bandwidth greater than 64%. Feed modification is performed in [33] by using a T-bar shape feed to enhance the bandwidth and improve the relative gain.

In this chapter, we present a method for reducing the cavity dimensions of a CBSA and examine the performance of such antennas. The technique is based on substituting the cavity structure with a series of miniaturized transmission line type resonators. Basically, the slot antenna is initially designed using a finite width metallic strip connected to a num-

ber of closely spaced parallel short-circuited microstrip lines with the same physical and electrical length as the width of the ground plane. These parallel lines are then meandered to reduce their physical length, while maintaining their electrical length, resulting in an overall reduction in the physical dimensions of the cavity-backed slot antenna. In what follows, first the method for modifying the structure of an ordinary CBSA is presented in Section 2.2. The cavity miniaturization technique is presented in Section 2.3. In both sections, simulation and measurement results of the antennas are presented and discussed.

2.2 Cavity-Backed Slot Antennas with Modified ground Planes

In this chapter, we use an off-centered open-circuited microstrip line, with a line impedance of 50Ω to feed the cavity backed slot antenna. The slot and the microstrip line are printed on the two different sides of a thin dielectric substrate with relative dielectric constant of ε_{ra}. This substrate is then placed on the cavity such that the slot is sandwiched between the bottom of the cavity and the microstrip line. The cavity itself is filled with a dielectric material with relative dielectric constant of ε_{rc}. The length of the open-circuited microstrip line, L_m, and its location, L_f, can be tuned to match the antenna's input impedance to that of the microstrip feed. In order to have an efficient radiator, the cavity width must be chosen close to $\lambda_c/2$ at the frequency of operation, where $\lambda_c = \lambda_0/\sqrt{\varepsilon}_{rc}$ is the wavelength inside the cavity and λ_0 is the wavelength in free space. At this frequency, the slot antenna has an approximate length of $\lambda_g/2$, where λ_g is the guided wavelength along the slot, which is in generally different from λ_c. Such a cavity-backed slot antenna is designed and simulated using a Method of Moments (MoM) based commercial simulation tool [34]. The rectangular slot has dimensions of $L_s = 50$ *mm* and $W_s = 2$ *mm* and is fabricated on a 0.5 *mm* thick RO4003 substrate from Rogers Corp. The substrate has a relative dielectric constant of $\varepsilon_{ra} = 3.4$, loss tangent of $\tan\delta_a = 0.0027$, and overall dimensions of $L_g = 53$ *mm* and

$W_g = 46$ *mm*. The cavity is fabricated by machining a piece of 6.35 *mm* thick TMM3 substrate and metallizing its sides. The material inside the cavity, TMM3, has a dielectric constant of $\varepsilon_{rc} = 3.3$ and loss tangent of $\tan\delta_c = 0.0020$. The antenna is fed using an off-centered open-circuited microstrip line, with an impedance of 50Ω, and it is matched to 50Ω by optimizing the length of the open-circuited stub, L_m, and the feed location, L_f, using full wave simulations. The complete geometrical dimensions and physical parameters of this antenna are listed in Table 2.1.

Parameter	L_s	W_s	L_g	W_g	L_c	W_c
Value	50	2	53	46	53	46
Parameter	L_m	L_f	h_c	h_a	ε_{rc}	ε_{ra}
Value	18	2.4	6.35	0.5	3.3	3.4

Table 2.1: Physical dimensions of cavity backed slot antennas of Section 2.2. All dimensions are in *mm*.

The fabricated ordinary cavity backed slot antenna operates at 2.25 GHz and there is a good agreement between the measured and simulated results. The radiation patterns of the antenna are measured in the E-plane (y-z plane) and H-plane (z-x plane) inside the anechoic chamber of the University of Michigan. It is observed that the antenna has low levels of cross polarized radiation in both E- and H-planes and it has a front-to-back ratio of about 8.6 dB. The front-to-back ratio, for fixed cavity dimensions, can be increased by increasing the dimensions of the antenna's ground plane. This, however, will increase the overall dimensions of the antenna, which may not be desirable in certain applications.

In order to evaluate the the miniaturization potential of this cavity backed slot antenna, it is important to first study the flow of electric current in the ground plane around the slot antenna. As observed in Figure 2.2, the electric current can be decomposed into two components: one that circulates around the slot, which is mainly responsible for creating a resonant condition and one that flows perpendicular to the slot. It is this latter component that is mainly responsible for radiation from the slot antenna. The electric current flowing parallel to the slot, along its length on one side and has the same magnitude as the current

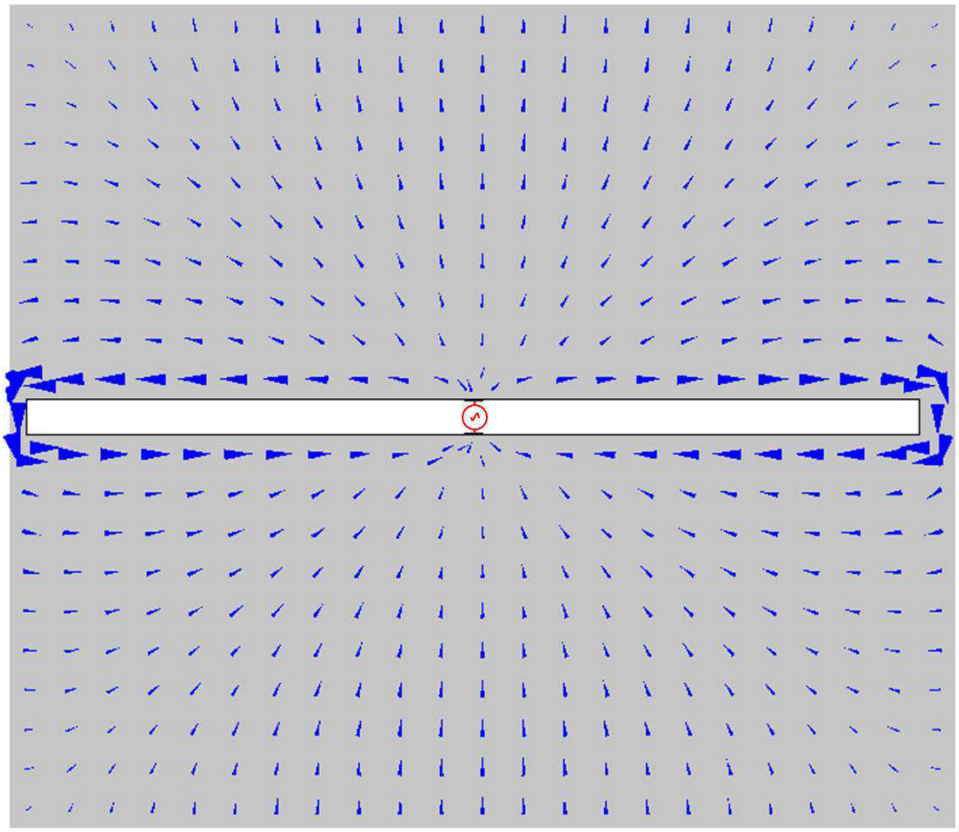

Figure 2.2: The electric current distribution in the ground plane around a slot antenna.

that is flowing parallel to the slot on the other side but these two components are 180° out of phase and hence, they do not contribute to far field radiation. As a first step towards reducing the dimensions of this antenna,the uniform metallic plane around the slot antenna is replaced with a loop defining the slot and a number of strips perpendicular to the slot as shown in Figure 2.3.

Here, the metallic loop around the slot supports the circulating component of the electric current and the parallel metallic strips support the normal component of the electric current. Since the parallel strips carry the radiating component of the electric current, their total number plays an important role in the radiation efficiency of the antenna. If the number of these strips is high enough, the response of the antenna will not be significantly different from the ordinary ground plane CBSA. However, decreasing the number of strips decreases the number of available paths for the normal component of the electric current

and consequently, decreases the density of the radiating current and reducing the radiation efficiency of the antenna. In this chapter, we take an experimental approach to validate this hypothesis by designing and fabricating three CBSAs with modified geometry each having one, five, and thirty strips of equal widths. The differences between these three antennas are the number of strips, the length of the open circuited microstrip feed, L_m, and the feed location, L_f. The geometrical values of these parameters and antenna dimensions are presented in Table 2.2 and in Figure 2.3.

Antenna Type	L_m	L_f
CBSA with 1 Strip	6.4 *mm*	1.2 *mm*
CBSA with 5 Strips	21.7 *mm*	2.9 *mm*
CBSA with 30 Strips	20 *mm*	2.9 *mm*
Ordinary CBSA	18 *mm*	2.4 *mm*

Table 2.2: Feed network parameters of CBSA with different ground plane configurations as discussed in Section 2.2.

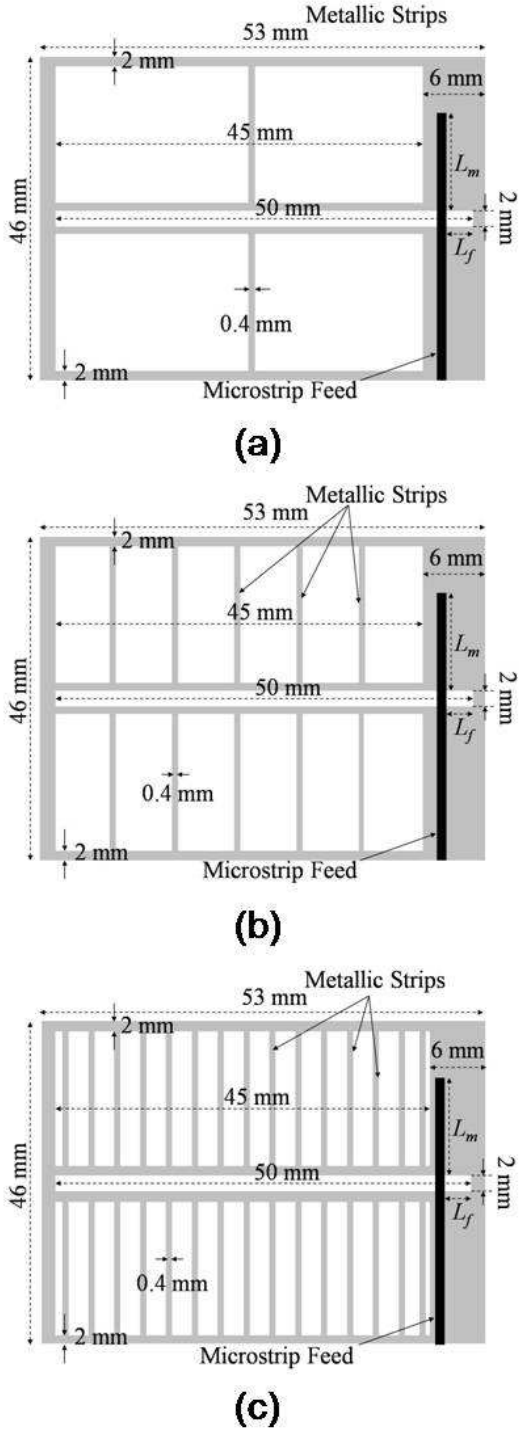

Figure 2.3: Topology of the modified ground plane of the microstrip-fed CBSA. The continuous ground plane is replaced with metallic strips normal to the slot antenna. (a) Modified CBSA with one strip, (b) Modified CBSA with five strips, (c) Modified CBSA with thirty strips.

The input reflection coefficients of these antennas are measured using a calibrated HP8720D vector network analyzer and the results are presented in Figure 2.4. It is shown that all three antennas can easily be matched to 50Ω by tuning the location (L_m) and length (L_f) of the open-circuited microstrip line. The difference in the resonant frequencies can be explained by the variations of L_m and L_f and deviations caused during the fabrication process.

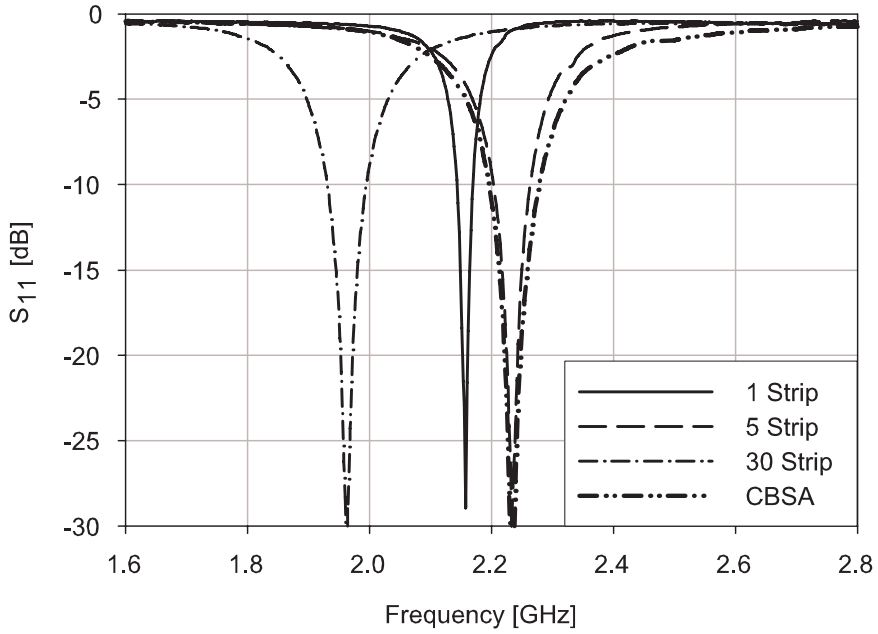

Figure 2.4: Measured S_{11} response of the ordinary CBSA and cavity-backed slot antennas with modified ground plane (Section 2.2). The topology of the antenna is shown in Figure 2.3.

The far field co-polarized and cross-polarized radiation patterns of these antennas are measured in the E- and H-planes (y-z and z-x planes) inside the anechoic chamber of the University of Michigan. Figure 2.5 (a)-(c), show the measured patterns of the cavity backed slot antennas with one strip, five strips, and thirty strips respectively. It is seen that the antenna patterns are similar to each other and to that of the ordinary CBSA. Furthermore, in all the measured results, low levels of cross-polarized radiation at bore-sight, are observed. The cross-polarized radiation is mostly caused by the close proximity of the coaxial cable that feeds the antenna to the antenna iteself. The front-to-back ratio (FTBR) of the antennas

are extracted from the measured radiation patterns and are presented in Table 2.3. It is seen that the FTBR of the antennas are not significantly affected by the number of strips. The gain of the antennas are also measured inside the anechoic chamber using a standard double-ridged horn antenna as the reference, the results are also presented in Table 2.3 along with the calculated directivity values obtained from full-wave simulations. Using the measured gain and calculated directivity values, the antenna efficiency is computed and the results are also presented in Table 2.3. As expected, the antenna gain, efficiency, and bandwidth are considerably affected by the number of strips. As the number of strips is increased both the antenna gain and bandwidth increase and approach the maximum values provided by the ordinary CBSA. As mentioned previously, increasing the number of paths of normal for the component of the electric current causes the antenna to radiate more efficiently and hence, for fixed physical dimensions, increases its gain. Furthermore, since a greater portion of the power delivered to the antenna is radiated, the ratio of stored energy to that of the radiated power (antenna Q) decreases or equivalently its bandwidth (BW) increases [17]. This explains why the ordinary CBSA and the CBSA with one strip have respectively the maximum and minimum bandwidth values.

Antenna Type	BW (%)	Gain (dBi)	Directivity (dBi)	η_{rad}	FTBR (dB)
1 Strip CBS	1.2	3.4	5.8	58%	8.0
5 Strips CBS	2.9	4.1	5.8	68%	9.0
30 Strips CBS	3.4	5.5	5.8	93%	7.9
Ordinary CBS	4.0	5.5	5.8	93%	8.6

Table 2.3: Radiation parameters of cavity backed slot antennas of Section 2.2.

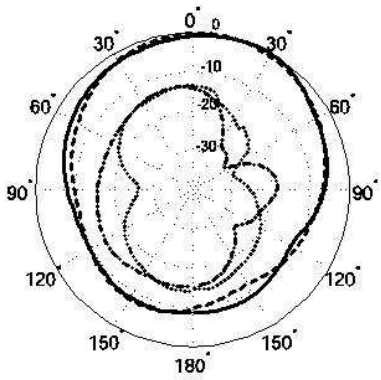

(a)

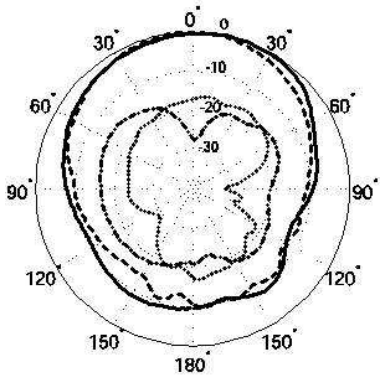

(b)

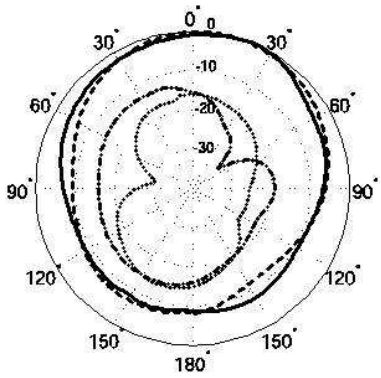

(c)

Figure 2.5: Measured radiation patterns of the cavity-backed slot antennas with modified ground plane studied in Section 2.2. (a) CBSA with one strip, (b) CBSA with five strips and (c) CBSA with thirty strips. Solid line: E-Plane Co-Pol, Dash-dotted line: E-Plane Cross-Pol, Dash-dashed line: H-Plane Co-Pol, and Dotted line: H-Plane Cross-Pol.

2.3 Reduced-Size Cavity-backed Slot Antenna

In this section, the CBSAs of the previous section will further be modified to reduce cavity dimensions and hence, significantly reduce overall size. The basic idea is to design the strips of the modified CBSA presented in the previous section in a compact fashion while maintaining their electrical length.

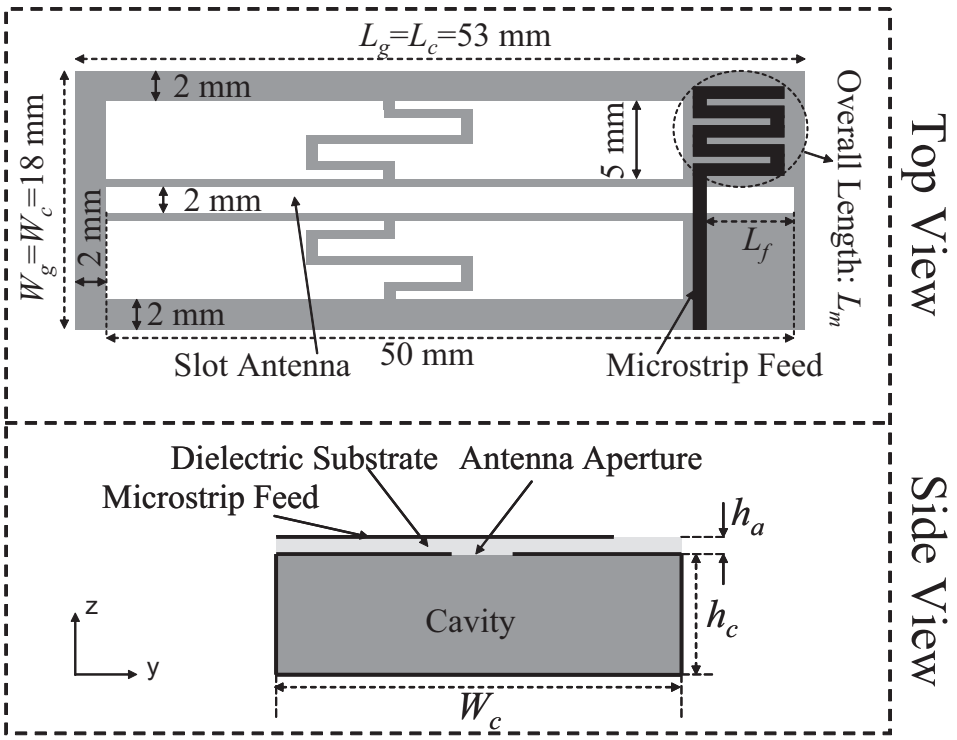

Figure 2.6: Topology of the reduced-size-cavity backed slot antenna. The antenna shown is a obtained from the CBSA with one strip in Section 2.2 by meandering the strip such that it maintains its electrical length. The microstrip feed is also meandered to conserve space.

Figure 2.6 shows the reduced-size version of the modified CBS antenna with one strip. Here, the strip is turned into a meander line to reduce the cavity width. The antenna is fed with a 50Ω microstrip line connected to a 75Ω open-circuited microstrip line that is meandered to conserve space, but has an overall length of L_m. The location of the microstrip feed, L_f, and the length of the open circuited stub, L_m, are tuned to match the input impedance of the antenna to that of the line impedance. A total of five different reduced-size cavity-

backed slot antennas (RS-CBSA) with different parameters are designed, fabricated, and measured. In all of the antennas, the slot antenna and the microstrip feed line are etched on two different sides of a 0.5 mm thick RO4003 substrate with a dielectric constant of $\varepsilon_{ra} = 3.4$, loss tangent of $\tan\delta_a = 0.0027$, and ground plane size of 53 $mm \times 18$ mm. Four of the antennas have cavity depth of 6.35 mm and one of them has cavity depth of 3.18 mm. Similar to the previous section, the cavities are machined out of 6.35 mm or 3.18 mm thick pieces of TMM3 substrate and the sidewalls are metallized. The geometrical parameters of the antennas are given in Table 2.4 and Figure 2.6.

Antenna Type	L_m (mm)	L_f (mm)	$L_c \times W_c \times h_c (mm^3)$
1 Meander	43.0	5.3	$53 \times 18 \times 3.18$
1 Meander	43.0	5.4	$53 \times 18 \times 6.35$
2 Meanders	52.0	6.9	$53 \times 18 \times 6.35$
3 Meanders	52.0	6.9	$53 \times 18 \times 6.35$
4 Meanders	52.0	6.9	$53 \times 18 \times 6.35$

Table 2.4: Feed network and physical dimensions of miniaturized-cavity backed slot antennas of Section 2.3.

The input reflection coefficients of the RS-CBSAs are measured using a calibrated HP8720D vector network analyzer and the measurement results are presented in Figure 2.7. It is observed that the antennas are very well matched to 50Ω independent of the number of meander lines.

The co- and cross-polarized radiation patterns of the antennas are measured in the E- and H- planes (y-z and z-x planes respectively). As an example, the normalized radiation patterns of the antenna with two meandered lines and cavity depth of 6.35 mm are shown in Figure 2.8. As is observed from this figure, the cross-polarized radiation levels are small at bore-sight. As in the previous case, the major contributor to the cross-polarized radiation is the close proximity of the coaxial cable feeding the antenna to the antenna itself.

The maximum gain of the RS-CBSAs are measured in the anechoic chamber using a standard double-ridged horn antenna as a reference and the results are presented Table 2.5. The directivity of the antennas are calculated using full-wave simulations in IE3D [34].

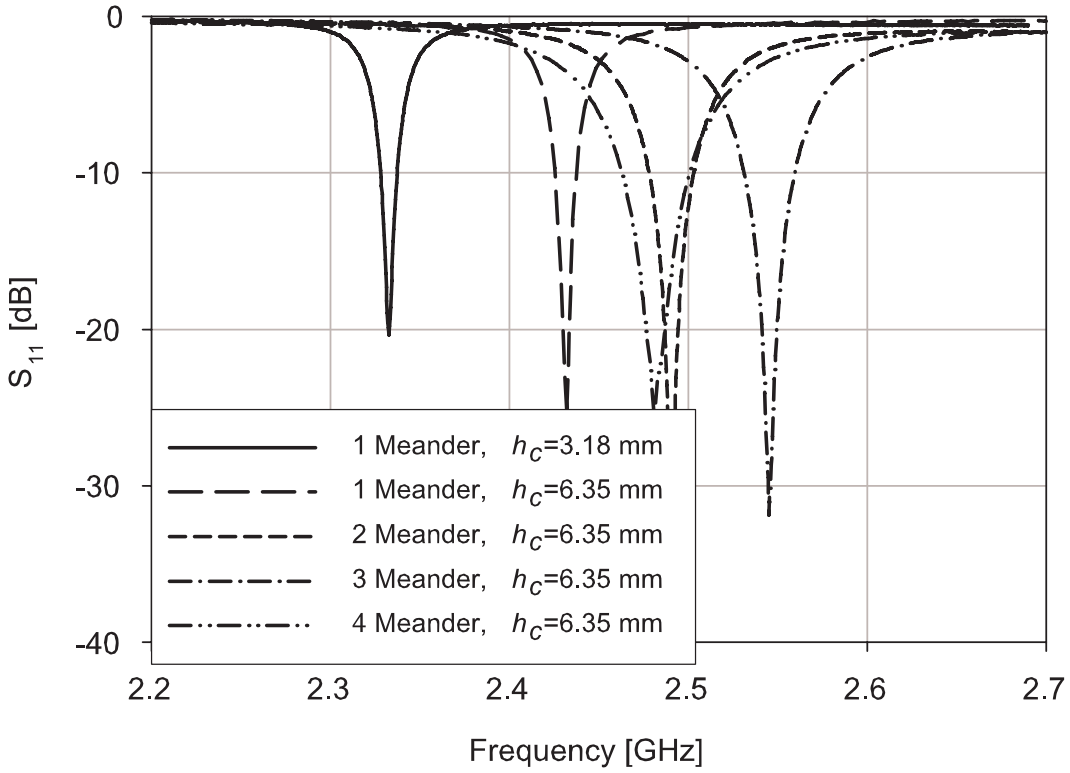

Figure 2.7: Measured return loss of the RS-CBSA of Section 2.3. The antenna topology is shown in Figure 2.6; feed network parameters are given in Table 2.4.

Using the measured gain and computed directivity values, the efficiency of the antennas are calculated and the results are presented in Table 2.5. It is observed that, as the number of meander lines and the cavity depth increase, the gain and efficiency of the antennas increase as well. This agrees with the previous observations in this chapter. The FTBR of the antennas are extracted from the measured radiation patterns and the results are presented in Table 2.5. The FTBRs of the RS-CBSAs are slightly smaller than the CBSAs studied in Section 2.2. This is caused by the significant decrease in the width of the antennas compared to the CBSAs of Section 2.2. Specifically, the total occupied volume of the miniaturized CBSAs has been reduced by 65% compared to the CBSAs presented in the previous section.

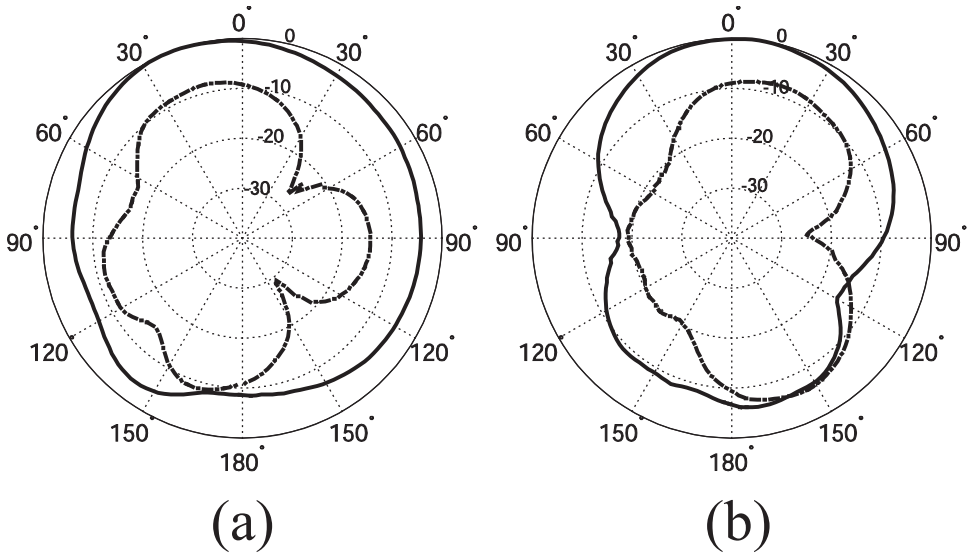

Figure 2.8: Measured radiation patterns of the reduced-size-cavity backed slot antenna that has a ground plane with two meander lines in the (a) E-Plane and (b) H-Plane. Solid Line: E-Plane, Co-Pol, Dash-dotted line: E-Plane, Cross-Pol, Dash-dashed line: H-Plane, Co-Pol, and Dotted line: H-Plane, Cross-Pol.

Antenna Type (h_c)	BW (%)	Gain (dBi)	Directivity (dBi)	η_{rad}	FTBR (dB)
1 Meander, (3.18 *mm*)	0.4	-2.3	4.0	23%	6.1
1 Meander, (6.35 *mm*)	0.5	-0.7	3.7	36%	6.0
2 Meander, (6.35 *mm*)	1.0	1.2	3.7	56%	7.5
3 Meander, (6.35 *mm*)	1.2	2.85	3.7	82%	7.4
4 Meander, (6.35 *mm*)	1.6	3.5	3.7	95%	7.0

Table 2.5: Radiation parameters of the miniaturized-cavity backed slot antennas of Section 2.3.

2.4 Summary

This chapter introduces a technique for reducing the dimensions of a cavity-backed slot antenna. The method is based on replacing the metallic ground plane around slot antennas with a series of ground plane backed, parallel metallic strips and designing these strips in a compact fashion. It is shown that using this technique, the overall occupied volume of a modified cavity backed slot antenna can be reduced by more than 65%. Furthermore, despite its reduced physical dimensions, the antenna can present a front-to-back ratio as high as 7 dB with relatively low levels of cross-polarized radiation, excellent impedance

matching, and high radiation efficiency.

CHAPTER 3

Platform Embedded Slot Antenna backed by Shielded Parallel Plate Resonator

The miniaturized CBSA features significant size reduction in conjunction with sufficient radiation performance. However, the issue of narrowband bandwidth common to CBSAs is still present. The modified ground plane with numerous meandered lines employed to reduce the width of the cavity greatly compresses the CBSA size. Thus, bandwidth enhancement through additional modification of the meandered microstrip feed and antenna aperture is determined to be limited. Continuing the efforts of Chapter 2, a different approach to reduce the profile of a CBSA is explored. The antenna ground plane remains largely unmodified while the cavity structure is extensively examined for a low-profile antenna with wide-band behavior.

3.1 Introduction

Historically, radiation performance of an antenna has been considered one of the highest priorities in determining antenna type and placement on a wireless communication system platform. At low RF frequencies such as HF- UHF bands, the size of antennas is relatively large. This has motivated significant research on antenna miniaturization. The

literature concerning antenna miniaturization can be categorized into the following two, different general approaches: 1) techniques based on antenna topology [21, 19, 3, 6, 35] and 2) methods based on use of materials [36, 37, 38, 9, 10]. In this chapter the focus is on miniaturizing the effect of the platform on antenna performance and reducing antenna effect on the platform aesthetic or other physical characteristics, such as aerodynamic drag. Significant interactions exist between the antenna and the platform where the antenna is placed. Such interactions can result in significant pattern, impedance matching, and gain degradation of the antenna once the antenna is integrated with the rest of the wireless communication system including the platform. Various studies have been done to characterize the effect of the platform for a variety of scenarios. Investigations regarding the effect of the mounting location for a whip antenna on an automobile vehicle are reported [39, 40]. In [41], it is postulated that the performance level of the HF antenna is highly dependent on the structure of the ship that the antenna is mounted on; this investigation includes scaling the entire ship to facilitate the design of the HF antenna.

Practical problems are encountered when antennas are integrated with circuit boards. These problems are carefully considered in [42, 43]. In [44] it is shown that the electrical performance of an antenna in a mobile handset terminal is primarily affected by non-electrical aspects of the handset design. These studies collectively indicate strong likelihood of radiation performance differences between an antenna in an open-space environment and the antenna being integrated with the rest of the wireless communication system across a broad spectrum of scenarios. In addition to radiation performance of the antenna, the overall mechanical complexity, ergonomics, aerodynamic drag etc. are considered during the antenna design process. For instance, whip antennas for vehicles are becoming increasingly scarce due to its negative impact on overall aesthetics despite their sufficient functional performance. Another scenario where antenna performance is often prioritized at the expense of other key parameters is low frequency synthetic aperture radar (SAR). For aviation applications, low frequency SAR antennas are typically mounted onto

the fuselage or the aircraft wings. It is also very difficult to attain vertical polarizations without significantly protruding the fuselage which adversely affects aerodynamic drag of the entire aircraft. An embedded antenna for commercial electronic devises are discussed in [16, 45, 46]. A series of possible solutions in designing an integrated paste-on antenna in a least intrusive and mechanically viable way for the E-2C Hawkeye aircraft is investigated in [47]. Therefore as wireless communication systems become increasingly diverse, versatile, and integrated, system level approach in antenna design is becoming increasingly demanding. For integration scenarios, slot antennas tend to be more advantageous over wire antennas since the wireless communication platform where the slot antenna is integrated into can be utilized for improved performance. As a result, slot antennas tend to exhibit greater efficiency compared to conventional wire antennas. For complex platform, system level approach in antenna design can require significant processing power often beyond the capacity of commercial EM solvers. This problem is exacerbated for scenarios where the wireless communication platform is electrically large. Slot antennas with high level of isolation which do not require system level design and the associated computational costs are favorable. Designing a shield (cavity) with dimensions comparable to wavelength to suppress backward radiation of a slot antenna is a common solution [1]. While this yields high isolation level, the design is intrusive because of it's extensive height of the antenna platform. Height reduction of the cavity is achieved by operating a cavity-backed slot antenna above its second resonance in [48]. In [49], it is demonstrated that the profile of a conventional cavity can be further reduced through modification of the cavity topology. In Chapter 2 of this dissertation, the dimension of the cavity-backed slot antenna is miniaturized by replacing the metal ground plane around the slot aperture with specially designed metallic patterns.

This paper presents an antenna that features a low-profile dimension suitable for platform-embedded scenarios. The antenna consists of a slot aperture backed by a Shielded parallel plate resonator. Integrated with the slot aperture, the proposed antenna functions similar to

a conventional cavity-backed slot antenna while having small lateral dimensions as well as vertical height less than $\lambda/15$. To fabricate the structure of the shielded parallel plate resonator without material support, the structure is designed and fabricated using Ultrasonic consolidation technology. The details of the proposed antenna is presented in Section 3.2. The measured antenna features high levels of gain, low levels of cross polarizations, and FTBR. The bandwidth of the antenna is enhanced by creation of an additional fictitious resonance close to the principle resonance and exhibits a wide-band mode. An arbitrary metallic platform is built and the Shielded parallel plate resonator-backed slot antenna is flush-mounted on the platform and the isolation levels are evaluated in Section 3.3. The proposed antenna is also redesigned and demonstrated for VHF applications using low-cost standard Printed circuit board (PCB) technology.

3.2 The Shielded Parallel Plate Resonator-backed Slot Antenna

Slot antennas are highly useful for applications where antennas must be mounted on a platform which requires minimum height profile. In addition slot antennas have inherently higher radiation efficiency than their counterpart wire antennas. However, the difficulties of implementing a slot antenna on a platform represent two challenges. Firstly, slot antennas at resonance will direct half of the radiated power in the undesired direction into the platform. Secondly, the backward radiation significantly increases the sensitivity of slot antenna to its environment. The input impedance, radiation pattern and gain of the slot antenna tends to significantly alter as a function of the platform. As a result, conventional slot antennas are generally designed to function in conjunction with a predefined platform. To mitigate these difficulties, unidirectional $\lambda_s/2$ resonant slot antennas are usually designed over a cavity resonator operating at a proper mode coherent with the field distribution over the slot. Consider a conventional cavity resonator-backed slot antenna as shown in Figure 3.1.

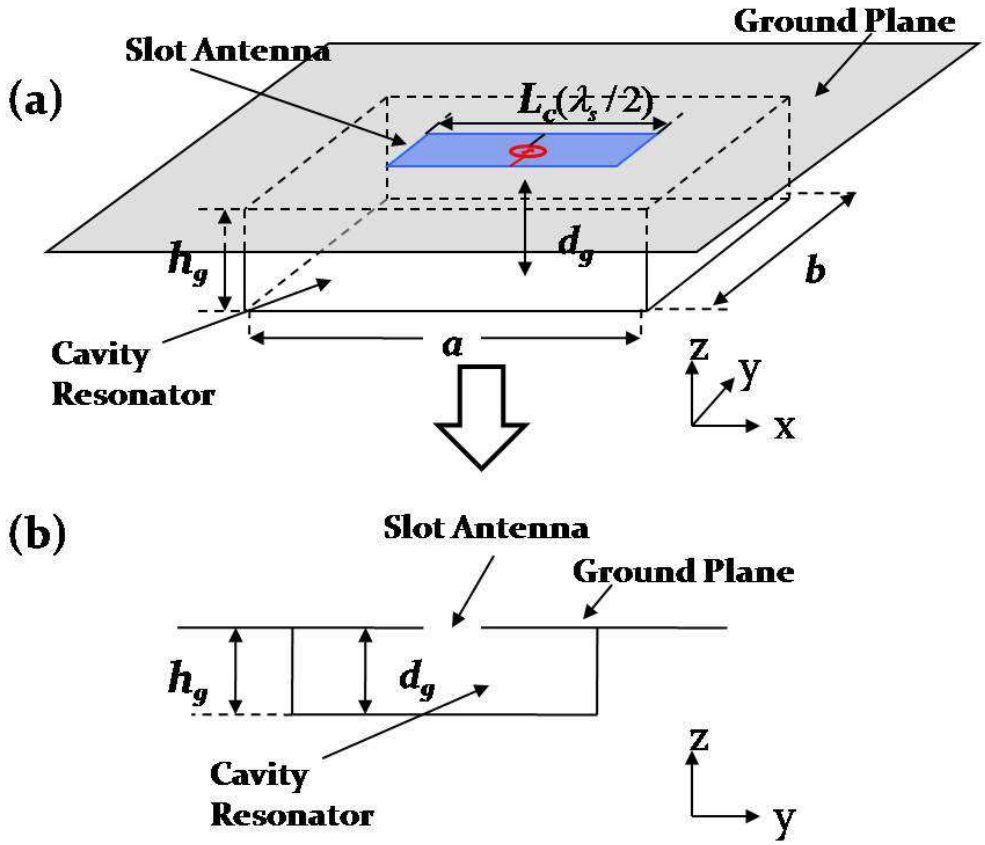

Figure 3.1: Topology of the cavity resonator-backed slot antenna. (a) 3-D View. (b) Topology in the y-z plane.

If we assume $h_g > a > b$ for the cavity resonator dimension in Figure 3.1, the propagating conditions within the cavity resonator can be expressed as

$$k_z = \sqrt{k^2 - k_x^2 - k_y^2}. \tag{3.1}$$

where

$$k_x = \frac{m\pi}{a}, \qquad k_y = \frac{n\pi}{b}, \qquad k_z = \frac{p\pi}{h_g} \tag{3.2}$$

If we assume the cavity resonator-backed slot antenna operates in the lowest-order (dominant) TE_{101} mode then, $m = 1$, $n = 0$, $p = 1$. Classical studies by Cockrell [24] and Long [25] have shown theoretically and experimentally that the susceptance of the cavity resonator backed- $\lambda_s/2$ slot antenna becomes negligible when h_g becomes $\lambda_g/4$ where λ_g is the guided wavelength. This can be explained by modeling the cavity resonator as a short-circuited transmission line of electrical length $\lambda_g/4$ in parallel with the open slot antenna. However as previously shown, this can only be achieved for specific cavity resonator modes. As a result, conventional cavity resonator backed-slot antennas feature narrow antenna bandwidth. In addition, the $\lambda_g/4$ height of the cavity resonator may be considered physically large especially at low frequencies when placed on a platform. Excavation of a $\lambda_g/4$ trench may also be difficult in many situations. The physical height of the cavity resonator can be further reduced using magneto-dielectric loading, but this leads to additional material loss and degradation of antenna gain.

3.2.1 Design of the Shielded Parallel Plate Resonator

We are looking for an alternative topology for a cavity resonator backed-slot antenna having small lateral dimensions and low vertical profile. For conventional cavity resonator-backed slot antennas shown in Figure 3.1, the height h_g of the cavity resonator is equal to the distance (d_g) from the slot aperture to the cavity resonator ground. These two parameters can be differentiated as shown in Figure 3.2 by devising a cavity resonator consisting of metallic parallel plates with fixed spacing (g) within the structure. By enclosing the parallel plate resonator in the z-x plane, the Shielded parallel plate resonator operates in the TEM mode. Hence, proper operation is achieved by adjusting the distance from the slot aperture to the resonator ground (d) to be $\lambda/4$ where λ is free space wavelength. As a result, the height (h) of the cavity resonator is significantly reduced through folding the parallel resonator multiple times. In addition, performance is independent of the longitudinal dimension since cutoff frequency is nonexistent for the Shielded parallel plate resonator.

The top ground plane supports electric currents moving perpendicular to the slot which are responsible for far-field radiation. The size of the slot ground plane and its symmetry around the slot determines the bandwidth and radiation efficiency [18]. The bandwidth is also determined by the volume occupied by the back resonator.

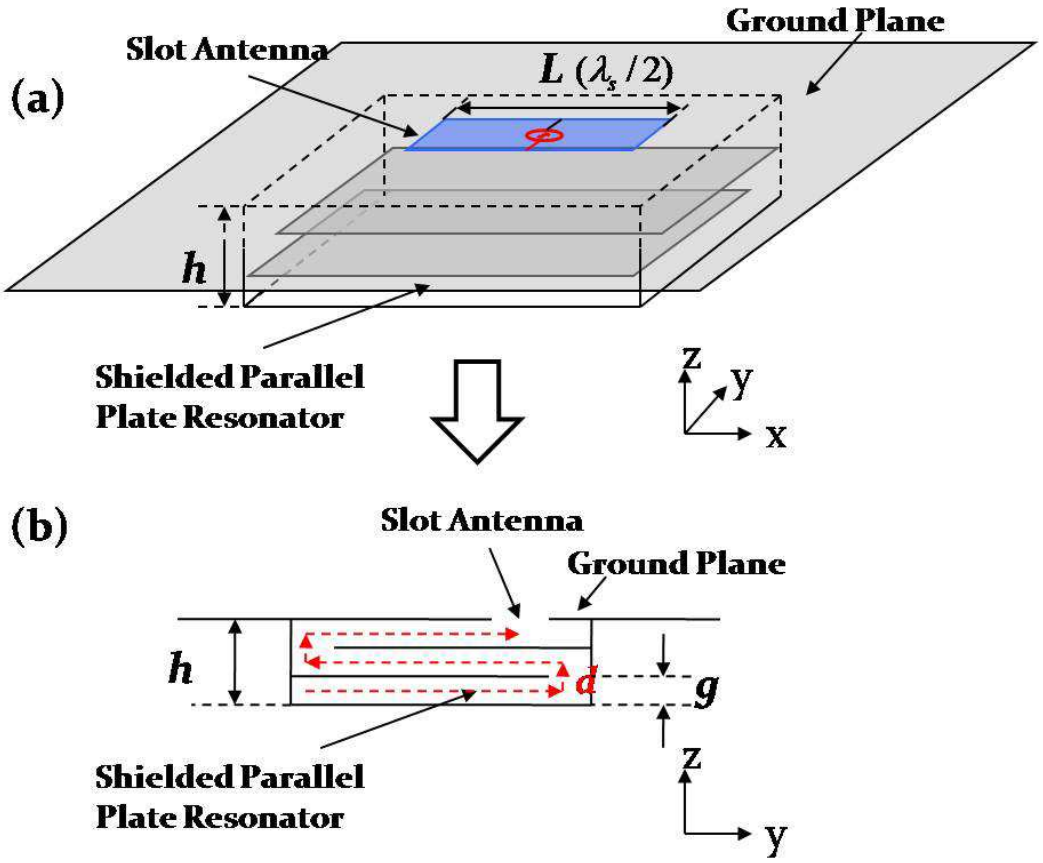

Figure 3.2: The rudimentary concept of the slot antenna backed by Shielded parallel plate resonator. (a) 3-D View. (b) Topology in the y-z plane.

To fully utilize the overall surface and increase the volume of the Shielded parallel plate resonator without increasing the height profile, dual resonator architecture with a metallic center pillar that separates the resonators is conceived as shown in Figure 3.3. The parallel plates combined with the center pillar forms two sub-resonators that are identical in dimension and each behave as a $\lambda/4$ resonator. The dimensions d and h are further optimized by considering the effect of the spacing g using Ansoft HFSS. The optimized Shielded parallel plate resonator is presented in Figure 3.4. The Shielded parallel plate

resonator is fabricated by Solidica of Ann Arbor, MI employing Ultrasonic consolidation technique. The technique involves merging layers of metal from conventional aluminium foil sheets using an ultrasound welding method [50]. The process produces metallurgical bonds and is capable of fabricating complex 3-D metallic topologies monolithically. The height of the completed Shielded parallel plate resonator (h) is less than $\lambda/15$, and less than $\lambda/8$ in width. The complete geometrical dimensions and physical parameters are listed in Table 3.1.

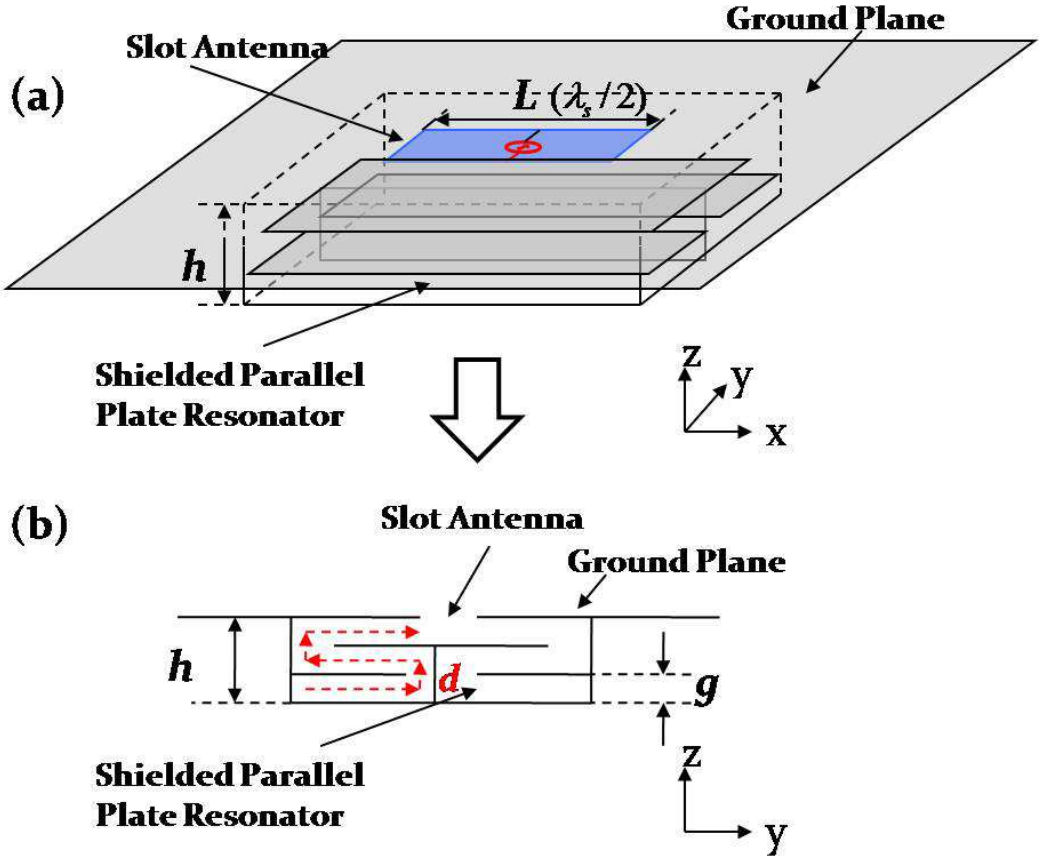

Figure 3.3: Topology of the slot antenna backed by Shielded parallel plate resonator. (a) 3-D View. (b) Topology in the y-z plane.

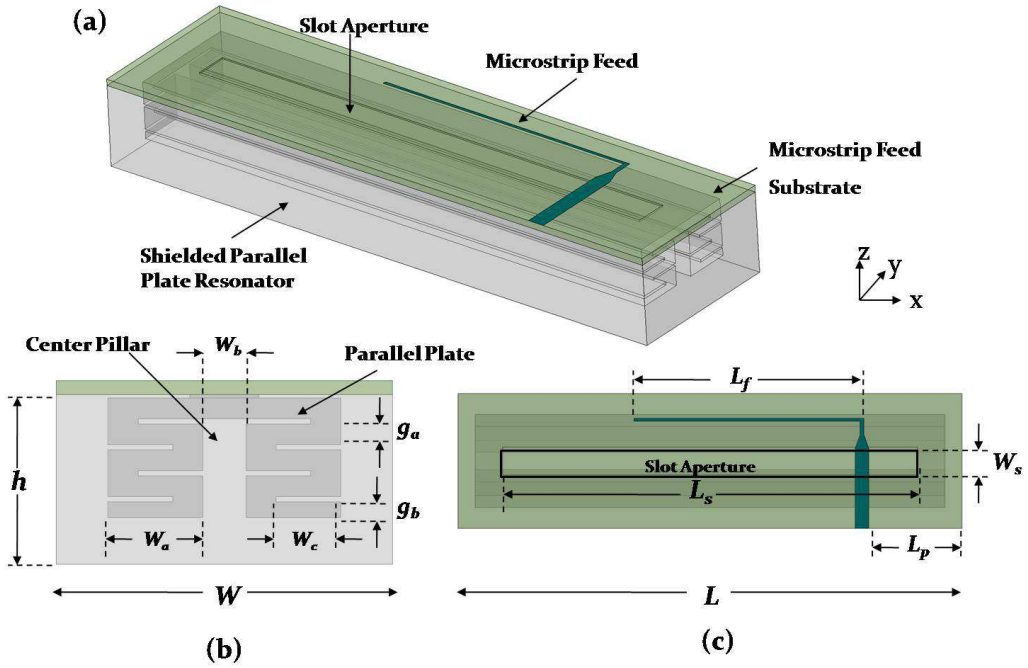

Figure 3.4: The optimized Shielded parallel plate resonator-backed slot antenna. (a) 3-D View. (b) Side view (y-z plane). (c) Top view (x-y plane).

h	W	W_a	W_b	W_c
9.8	19.5	5.5	2.5	3.75
L	L_s	W_s	g_a	g_b
73	60	4	1.2	0.9

Table 3.1: Design parameters of the optimized Shielded parallel plate resonator-backed slot antenna (*mm*).

3.2.2 Design of a Wideband slot aperture on the Shielded Parallel Plate Resonator

The slot aperture is designed and fabricated on the top surface of the Shielded parallel plate resonator. An off-centered 50Ω microstrip feed connected to a open-circuited 110Ω microstrip is designed to excite the slot aperture. It has been reported in [51] that the bandwidth of a slot antenna in open-space can be enhanced to feature wide-band or dual-band behavior with consistent radiation behavior. Similarly, the microstrip feed can be adjusted so the Shielded parallel plate resonator-backed slot antenna features a second

fictitious resonant frequency slightly above the first resonant frequency. Values for l_f and l_p shown in Figure 3.4 are chosen to merge the two resonances to achieve a wide-band mode. The simulated input reflection coefficients of the antenna as a function of parameters l_f and l_p are presented in Figure 3.5 and Figure 3.6. The optimized values of l_f and l_p are 33 *mm* and 12.5 *mm* respectively. The microstrip feed is fabricated on a 0.8 *mm* thick RO4003 from Rogers Corp. substrate with dielectric constant of $\varepsilon_f = 3.4$, and loss tangent of $\tan\delta_f = 0.0027$. The substrate is then placed on the Shielded parallel plate resonator such that the slot aperture is sandwiched between the bottom of the proposed resonator and the microstrip feed susbtrate. The slot aperture excited by the microstrip feed is presented in Figure 3.4 (c).

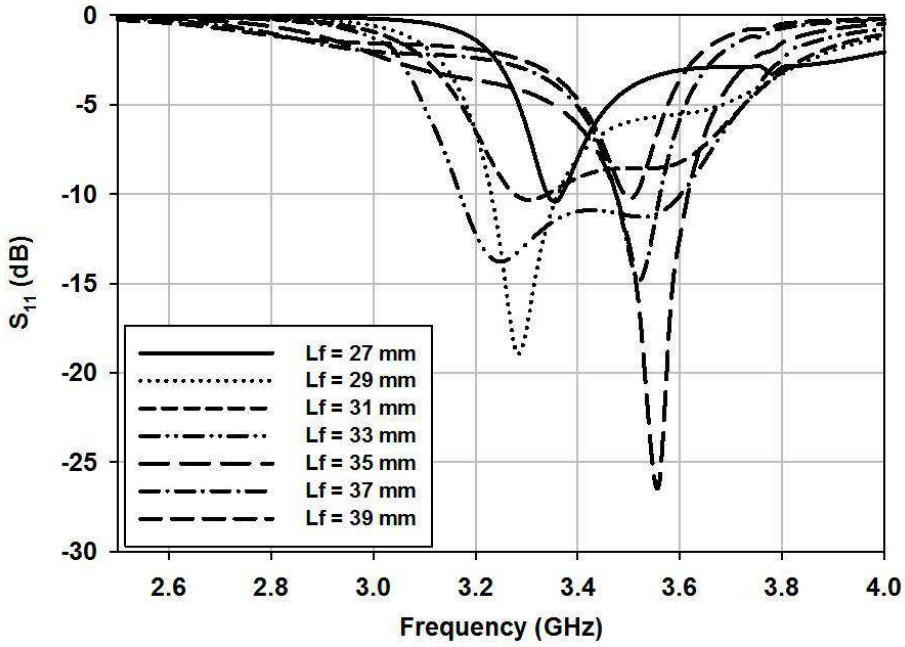

Figure 3.5: Simulated input reflection coefficients of the Shielded parallel plate resonator-backed slot antenna as a function of L_f with L_p = 12.5 *mm*.

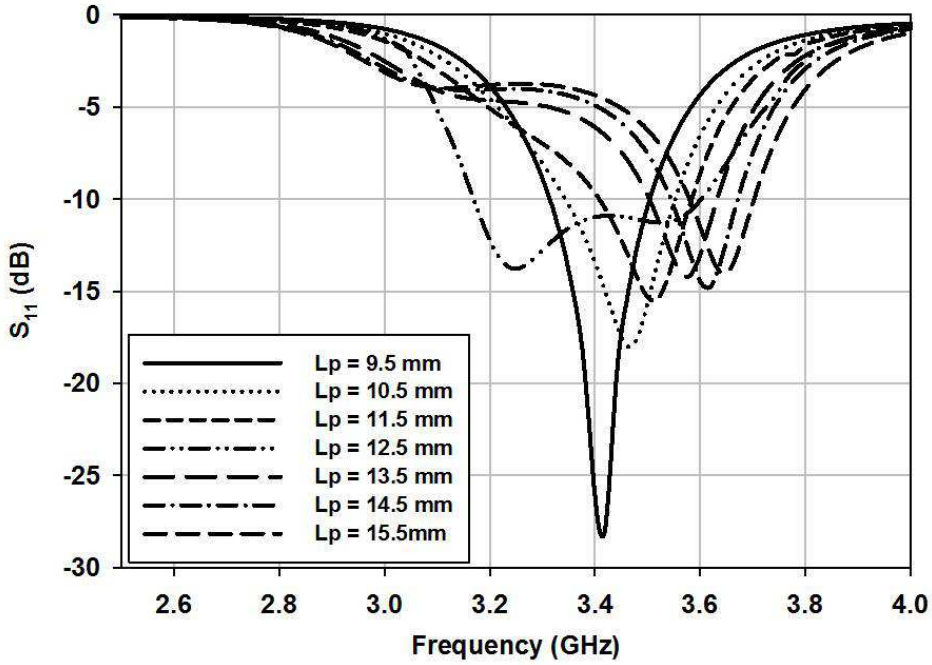

Figure 3.6: Simulated input reflection coefficients of the Shielded parallel plate resonator-backed slot antenna as a function of L_p with $L_f = 33\ mm$.

3.2.3 Measurements and Discussion

An SMA connector is connected to the microstrip feed of the Shielded parallel plate resonator-backed slot antenna. The measured input reflection coefficient is measured using a calibrated HP8729D vector network analyzer and the measured and simulated results are presented in Figure 3.7. The difference in the overall shape of the input reflection coefficient curve can be mostly attributed to deviations caused during the fabrication process, the effect of the SMA connector, and material tolerance levels. Nonetheless simulated and measured results both display more than 14% 2:1 VSWR indicating that the measured result is a product of the merge of the two resonances that can be clearly observed in the simulated result. The far field co-polarized and cross-polarized radiation patterns of the antenna are measured in the E- and H-planes inside the anechoic chamber of the University of Michigan and the results are presented in Figure 3.8. It is observed that the Shielded parallel plate resonator-backed slot antenna has low levels of cross polarizations and fea-

tures more than 7.0 dB front-to-back ratio (FTBR). The gain of the antenna is measured in the anechoic chamber using a standard double-ridged horn antenna as a reference and the results are presented in Table 3.2. The measurement indicates the proposed geometry of the Shielded parallel plate resonator behaves similarly as an effective cavity resonator while featuring very low profile.

Frequency (GHz)	Measured Gain (dBi)	FTBR (dB)
3.2	3.9	7.0
3.32	4.5	7.2
3.45	3.8	6.7

Table 3.2: Measured gain and FTBR of the Shielded parallel plate resonator-backed slot antenna studied in Section 3.2.

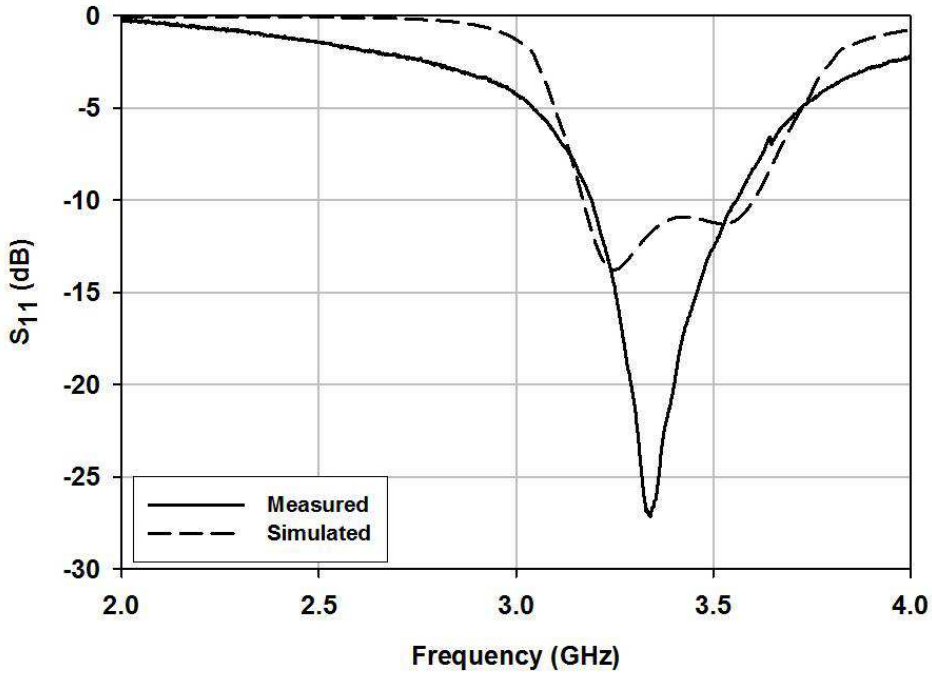

Figure 3.7: The measured and simulated input reflection coefficients of the Shielded parallel plate resonator-backed slot antenna.

As discussed earlier, since the Shielded parallel plate resonator operates in the TEM mode, the longitudinal length (L) of the structure can be further reduced without altering

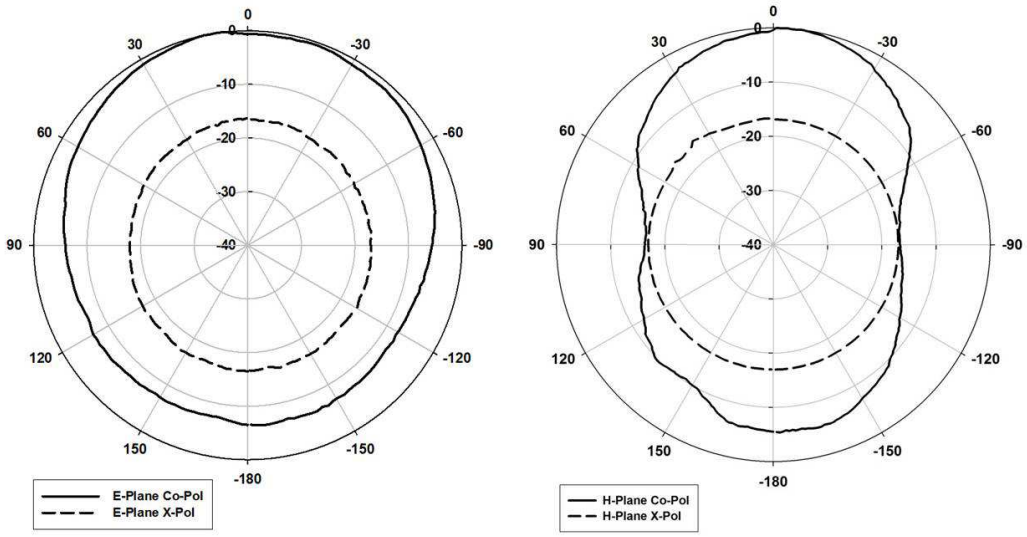

Figure 3.8: Measured radiation patterns of the Shielded parallel plate resonator-backed slot antenna studied in Section 3.2. E-Plane (Left). H-Plane (Right).

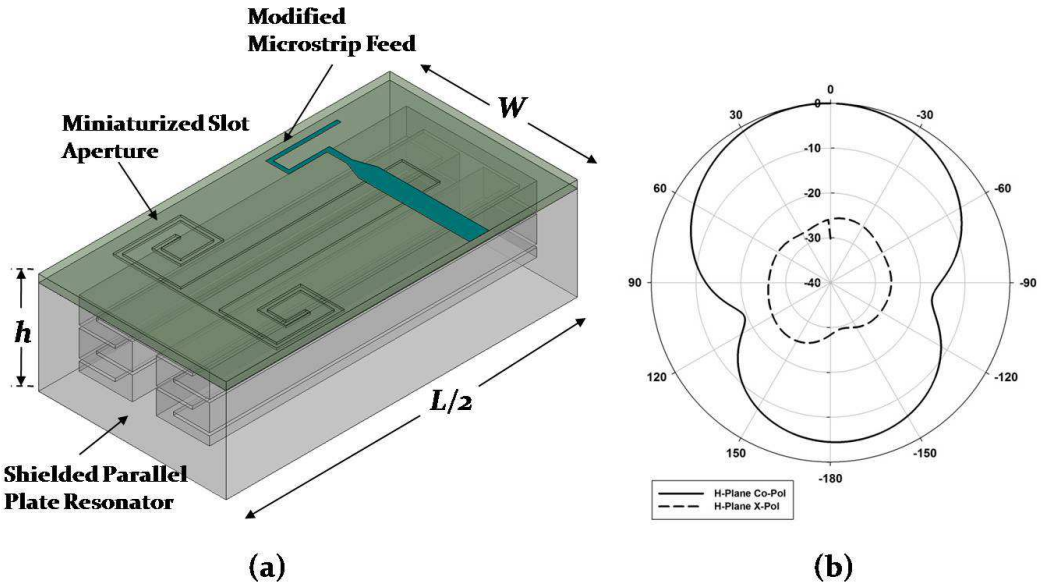

Figure 3.9: Miniaturized slot antenna backed by Shielded parallel plate resonator. (a) 3-D View. (b) Simulated radiation pattern (H-Plane).

the functionality. Studies in [21] and [19] have devised methods of miniaturizing the longitudinal length of a slot antenna while preserving the radiation patterns. A similar miniaturized slot antenna topology is adapted and backed by a Shield parallel plate resonator with half of the original longitudinal length ($L/2$). The rest of the design parameters for the

structure are unmodified. The miniaturized slot antenna backed by Shielded parallel plate resonator is designed and the radiation patterns are simulated as shown in Figure 3.9. The simulated patterns remain similar to that before miniaturization. The simulated bandwidth is found to decrease, which is in accordance with previous studies [21], [19].

3.3 Applications of the Shielded Parallel Plate Resonator-backed Slot Antenna

3.3.1 Demonstration of the Proposed Antenna Functioning as a Platform-Embedded Antenna.

The validity of the Shielded parallel plate resonator-backed slot antenna was confirmed in the previous section. Now we return to the original objective of successfully mounting the proposed antenna on a platform. First, a metallic platform of arbitrary dimensions is built. A trench with identical volume as that of the Shielded parallel plate resonator-backed slot antenna is then created on the top surface of the metallic platform. A small hole is drilled through the metallic platform for the placement of the semi-rigid feeding cable for the antenna structure. The antenna topology remains unmodified. The feeding network is redesigned using identical RO4003 substrate discussed in Section 3.2. The width (W_m) of the microstrip feed substrate is increased to accommodate for the semi-rigid coaxial cable which replaces the SMA connector. The modified feeding network is shown in Figure 3.10. Parameters l_{fm} and l_{pm} are slightly adjusted to achieve wide-band mode and the optimized values are 32.1 *mm* and 12.4 *mm* respectively.

The input reflection coefficient, radiation patterns in the E- and H-planes, and the gain are measured for the modified Shielded parallel plate resonator-backed slot antenna in open-space. The measurement process is repeated when the modified antenna is completely embedded into the metallic platform in a flush-mount fashion. Photographs of the metal-

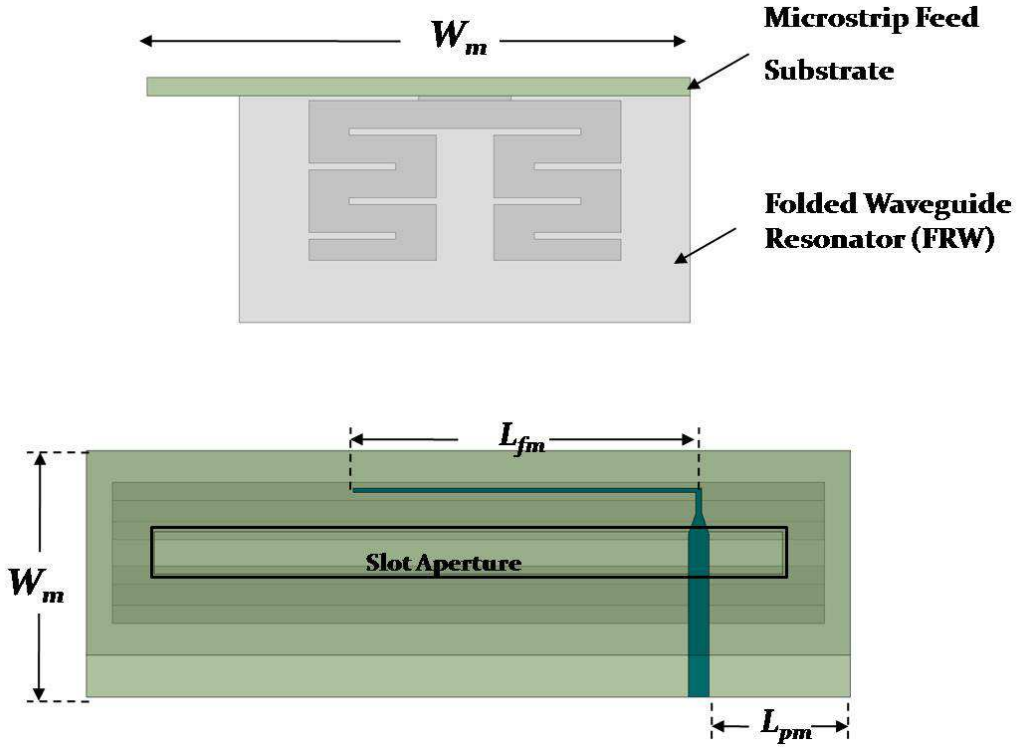

Figure 3.10: The Topology of the Shielded parallel plate resonator-backed slot antenna with modified microstrip feed network discussed in Section 3.3.

lic platform is presented in Figure 3.11 (a). The Shielded parallel plate resonator-backed slot antenna is first flush-mounted into the trench of the metallic platform as shown in Figure 3.11 (b). Then the modified feed network substrate is placed above the slot aperture and secured. A small through hole is drilled at the edge of the microstrip feed substrate to ensure connection to the center conductor of the semi-rigid coaxial cable. Lastly, the semi-rigid coaxial cable is inserted through the small hole in the metallic platform from the bottom and the tip of the center conductor is soldered to the microstrip feed. The measured input reflection coefficients of the proposed antenna in open-space case and platform-embedded case are presented in Figure 3.12. The measurement indicates that the resonant frequency and polarization of the antenna when embedded in the metallic platform are preserved. This confirms the proposed antenna features low levels of sensitivity to its platform while requiring minimum surface intrusion. When embedded, the modified Shielded parallel plate resonator-backed slot antenna is observed to have more 10% 2:1 VSWR bandwidth. The

difference in the magnitude of the input impedance matching can be mostly attributed to the deviations during the assembly process as the microstrip feed substrate and the semi-rigid coaxial cable must be separated from the antenna to be embedded in the metallic platform and then reinstalled afterwards. The measured E- and H- Plane far-field radiation patterns (normalized) for both cases are presented in Figure 3.13. As expected, it is observed that the metallic platform has significant effect on both planes of the far-field patterns. The metallic platform behaves as an electrically large ground plane that further suppresses the backward radiation of the Shielded parallel plate resonator-backed slot antenna. This is supported by the increase in directivity in the patterns when the antenna is embedded in the platform compared to antenna in open-space. The FTBR is measured to be 8.2 dB in open-space. Measurements indicate the FTBR is enhanced to 22 dB for the embedded case. The cross polarizations are also affected by the presence of the metallic platform, resulting in a slight increase in the direction of boresight. The measured gain and FTBR for both cases are summarized in Table 3.3.

Open-space			Platform-Embedded		
Frequency (GHz)	Gain (dBi)	FTBR (dB)	Frequency (GHz)	Gain (dBi)	FTBR (dB)
3.3	4.4	8.2	3.3	5.3	22.5
3.4	3.9	7.8	3.3	5.1	22.1
3.5	4.0	7.8	3.5	5.1	22.1

Table 3.3: Measured gain and FTBR of the Shielded parallel plate resonator-backed slot antenna in the presence of a metallic platform.

(a)

(b)

Figure 3.11: Photographs of the arbitrary metallic platform and the Shielded parallel plate resonator-backed slot antenna. (a) The antenna and the trench in the metallic platform can be observed. (b) The antenna is flush-mounted (embedded) into the metallic platform. The feeding network is not shown.

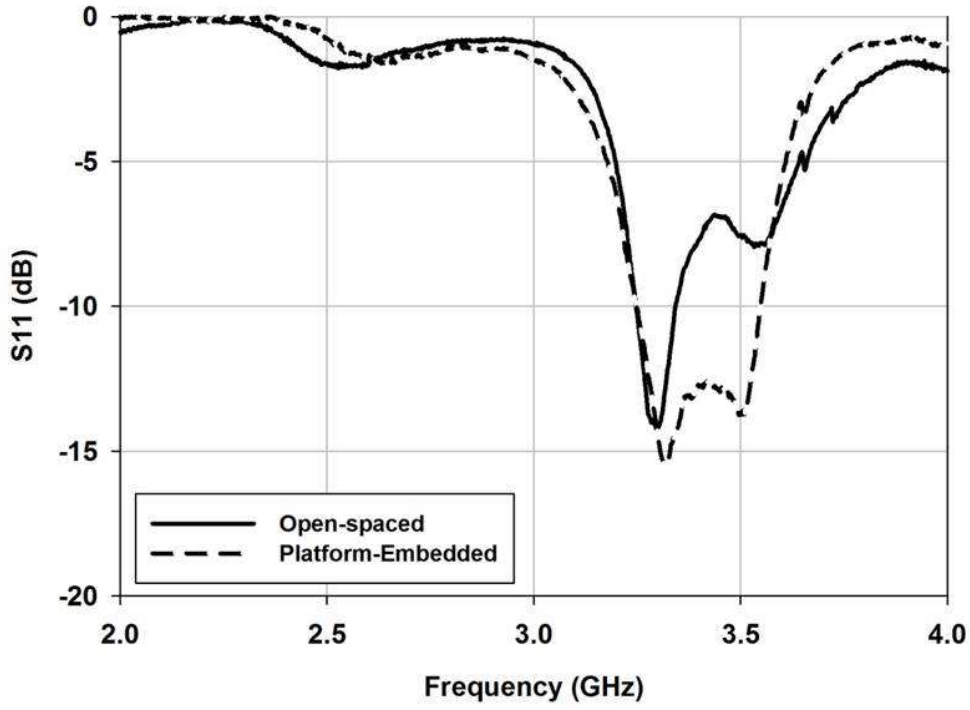

Figure 3.12: The measured input reflection coefficients of the Shielded parallel plate resonator-backed slot antenna in the presence of the metallic platform.

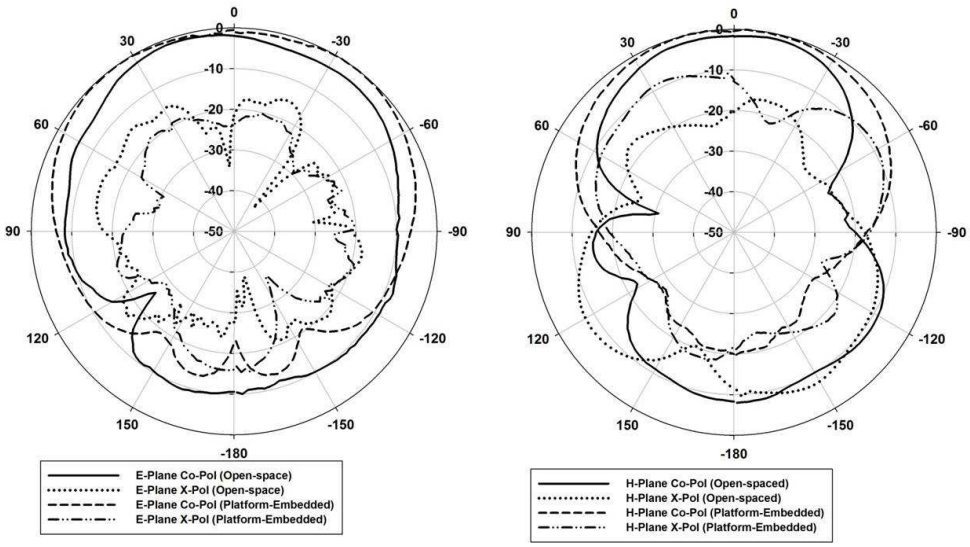

Figure 3.13: Measured radiation patterns of the Shielded parallel plate resonator-backed slot antenna in the presence of the metallic platform. E-Plane (Left). H-Plane (Right).

3.3.2 Designing The Shielded Parallel Plate Resonator-backed Slot Antenna using Printed Circuit Board (PCB) Technology.

The physical dimension of a conventional cavity resonator becomes increasingly problematic as the frequency of operation decreases. The Ultrasonic consolidation process employed in the previous section to fabricate the Shielded parallel plate resonator-backed slot antenna proves to be precise and reliable. However the current fabrication time and cost necessitate to further examine whether the FWRA can be designed using conventional multi-layer Printed circuit board (PCB) technology. The proposed antenna is scaled to operate in the VHF band using the original topology. The parallel plates are printed on 1.6 *mm* thick FR4 substrates with dielectric constant of $\varepsilon_a = 4.4$, and loss tangent of $\tan\delta_a = 0.02$. The center pillar and the side walls are constructed using Plated Vias with outer radius of 2.5 *mm*. To avoid the usage of Blind Vias, the Shielded parallel plate resonator is constructed by first fabricating two separate blocks, one representing the upper portion of the resonator, and the other representing the lower portion of the resonator that contains the center pillars. The fabrication process of the Shielded parallel plate resonator using PCB technology is visualized in Figure 3.14. Photograph of the fabricated Shielded parallel plate resonator-backed slot antenna using PCB technology is presented in Figure 3.15. The microstrip feed network is redesigned in a similar way as discussed in Section 3.3 using a 0.5 *mm* thick RO4003 from Rogers Corp. substrate with dielectric constant of $\varepsilon_f = 3.4$, and loss tangent of $\tan\delta_f = 0.0027$. Considering the physical dimensions of a 50Ω microstrip feed at VHF band, the slot aperture is matched to the 110Ω portion of the microstrip feed. The corresponding values for l_f (length) and l_p (position) defined in Section 3.2 for the microstrip feed are 102 *mm* and 52 *mm* respectively. The antenna is completed by stacking the microstrip feed substrate on the resonator. The completed dimension of the antenna using PCB technology is 365 *mm* $\times$ 150 *mm* $\times$ 8.5 *mm*. This corresponds to a cavity height of $\lambda/130$. The measured and simulated input reflection coefficients can be observed in Figure 3.16. The measurement confirms the mechanism and functionality of the pro-

posed antenna remain consistent after adapting a PCB technology approach. The operating frequency range of the redesigned Shielded parallel plate resonator-backed slot antenna is below the operating range of the anechoic chamber and therefore the measured patterns are omitted. Nevertheless, simulations show far-field radiation patterns similar to those previously presented.

3.4 Summary

A new class of low-profile resonator-backed slot antenna is presented and discussed. The proposed antenna is derived from a conventional cavity resonator-backed slot antenna. However, the proposed cavity resonator operates in the TEM mode. The proposed cavity resonator is modified to feature excellent gain and FTBR whilst having the height reduced to value as low as $\lambda/130$. The antenna bandwidth is further enhanced by the additional creation of a fictitious resonance that is merged with the principle resonance of the antenna. The electrically small dimensions of the antenna is advantageous for scenarios where the antenna must be integrated with the rest of the wireless communication platform with minimum intrusion. The Shielded parallel plate resonator-backed slot antenna is fully embedded into an arbitrary metallic platform. Measurements show consistency in input impedance matching of the proposed antenna for platform-embedded scenario indicating high levels of isolation. Significant increase in FTBR is observed. The antenna is redesigned for VHF applications and fabricated using conventional Printed circuited board (PCB) technology. Measurements support the possibility of using the Shielded parallel plate resonator-backed slot antenna using PCB technology for relatively low-cost application scenarios.

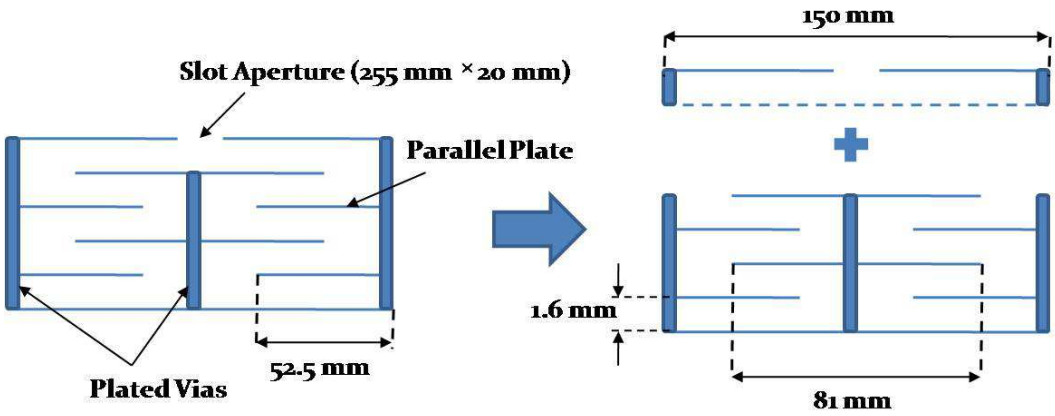

Figure 3.14: Side view of the Shielded parallel plate resonator-backed slot antenna using PCB technology.

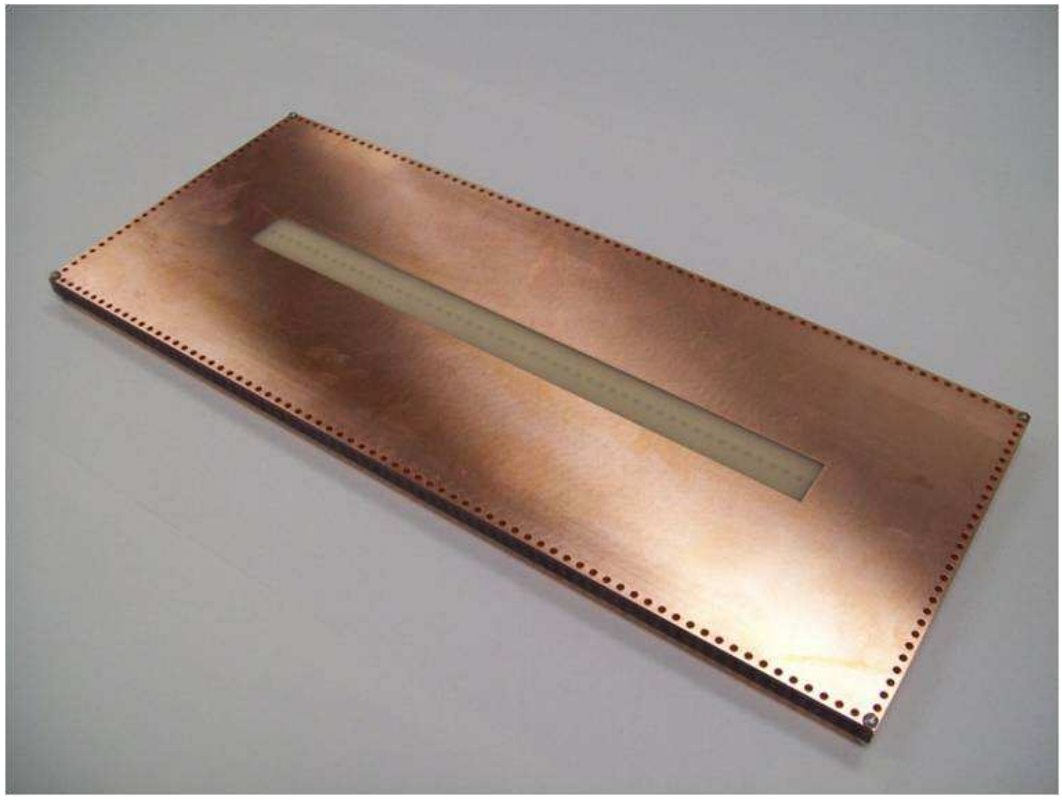

Figure 3.15: The fabricated Shielded parallel plate resonator-backed slot antenna using PCB technology.

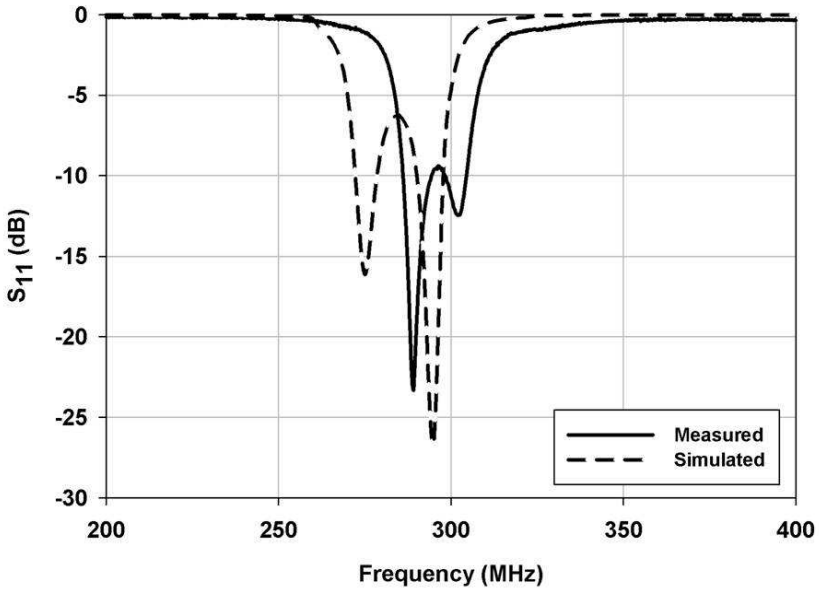

Figure 3.16: The measured and simulated input reflection coefficients of the Shielded parallel plate resonator-backed slot antenna using PCB technology.

CHAPTER 4

The Cavity-backed Composite Slot Loop Antenna

4.1 Introduction

Active and passive sensor technology is becoming increasingly pervasive. Unprecedented advances in smart packaging, power management and digital signal processing has enabled compact, robust sensors with identifying, tracking, and monitoring capabilities. Recently, such sensors have been shown to be potentially applicable in areas of agriculture, home automation, building monitoring and military surveillance. For military purposes, Unattended Ground Sensors (UGS) have proven to be worthy in various missions in the past [52, 53]. Deployment of UGS is ideal for monitoring troop encampments, supply routes, depots and hostile targets. Oftentimes, hand-emplaced or air-delivered sensor communication hardware requires to be implemented in environments where evading detection becomes of utmost importance. In addition, presently each soldier is packing over 15 *lbs* of sensor modules for hand-emplaced deployment in support of an operational strategy [52]. Future UGS hardware must be further miniaturized to reduce its weight and improve mobility and rigidity. For majority of UHF communication devices, the antenna is the largest component. Antenna miniaturization becomes a crucial task in many situations in achieving a low-profile, compact UGS module. An antenna with omnidirectional radiation pattern is required for situations where the modules are deployed swiftly and randomly through a

variety of methods such as air-delivered deployments. It has been shown that vertical polarization is less susceptible to path loss for both free space condition and non-line-of-sight conditions. The comparison of excess path loss as a function of distance for near-ground propagation is presented in Figure 4.1. Therefore vertical wire antenna is preferred for near-ground terrestrial communication scenarios. However, the large vertical profile of the antenna especially at relatively low frequency bands must be greatly reduced for practical usage. In addition, deployment of vertical antennas on a small transceiver requires proper mechanical support and packaging. Such antennas cannot be fabricated monolithically and have to be mounted on the transceiver package manually.

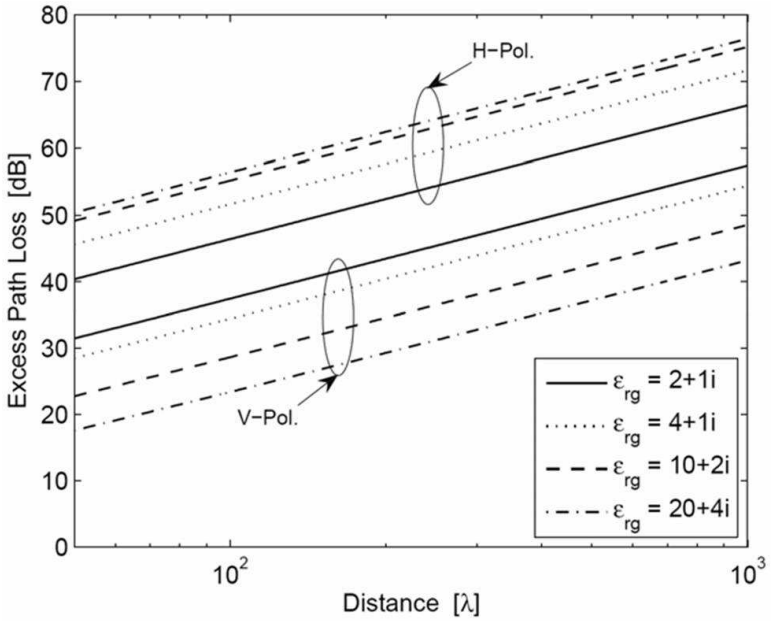

Figure 4.1: Excess path loss as a function of distance for vertical and horizontal polarizations. (Courtesy of Dr. DaHan Liao.)

Studies regarding planar antennas for wireless communications have been carried out extensively in the past [54, 55, 56, 57]. However, these antennas similar to a slot dipole have uniform radiation patterns in the plane perpendicular to the ground plane of the antennas. For finite size ground plane there are radiation nulls in the plane of the antenna ground. Therefore, these planar antennas [54, 55, 56, 57] are not suitable for omnidirectional antennas with low-vertical profiles for near-ground communications. Furthermore,

the performance of the antennas remain a function of the ground plane, indicating possible occurrence of ripples and edge diffraction when using relatively small ground planes.

To circumvent the limitations caused by ground planes, various semi-omnidirectional and omnidirectional 3D antenna structures with less dependence on the ground plane have been studied and proposed. A magnetic loop was emulated by implementing metallic patches on the exteriors of vertically-orientated dielectric rods [58, 59, 60, 61]. However, achieving low-profile remains an issue. To preserve the low-profile characteristics of planar antennas while mitigating the effects of the ground plane, implementation of metallic cavities or ground planes behind such antennas have been found to be effective.

Different types of cavity-backed slot antennas (CBSA) have been extensively studied both analytically and experimentally [62, 63, 64, 65]. The input impedance of a rectangular slot antenna, backed by a cylindrical cavity has been derived analytically using mode matching and complex Poynting theorem and verified experimentally in [64]. In addition to the conventional advantages of placing a cavity such as shielding, an air cavity is shown to reduce the phase noise of an active slot loop antenna in [65].

In this chapter, a miniaturized cavity-backed composite slot loop antenna (CBCSLA) with omnidirectional radiation in the horizontal plane with vertical polarization and extremely small height is proposed and presented. The concept is based on emulating a magnetic loop with close to uniform current distribution. The loop is further modified using geometrical symmetry to reduce the dimension of the loop to a fraction of the wavelength. For near-ground installation, a cavity is placed behind the loop to prevent cancellation of radiation in the horizontal plane. For this antenna, radiation is caused by strong electric currents flowing on the walls of the metallic cavity, radiating similar to a dipole antenna. Thus, a small omnidirectional antenna with high isolation levels to its surrounding environment is achieved. The method for modifying an ordinary slot loop antenna into the proposed antenna is presented in Section 4.2. Additional studies to improve the performance of the antenna is discussed. The simulation and measurement results of the antenna is presented

and discussed in Section 4.3. In Section 4.4, the topology of the antenna is further modified to realize dual-band operation.

4.2 Cavity Backed Slot Antennas with Modified Ground Planes

4.2.1 Antenna Design

The symmetry of Maxwell's equation can be used to replace a short vertical dipole antenna with a horizontal magnetic loop, which can be realized with a slot loop antenna. However the equivalence relation between a vertical dipole and a slot loop is only valid when the perfectly conducting ground plane is infinitely large. Using field equivalence principle, the slot can be covered with a perfect electric conductor with a magnetic current loop above and below. To satisfy the continuity of tangential magnetic field across the slot, the equivalent magnetic currents above and below the PEC have same magnitude but opposite directions. In case of finite size ground plane, cancellation occurs between the radiation of the magnetic loop currents on top of the ground plane and radiation of the magnetic loop current below the ground plane along this plane. That is, unlike the radiation pattern of a vertical dipole there is radiation null along the horizontal plane. Therefore, the ground effect must be shielded in order to alleviate the image cancellation phenomenon and preserve the characteristic behavior of the circular slot antenna. It has been found that by implementing a circular slot on the top surface of a metallic cavity, the omnidirectional radiation pattern can be preserved assuming constant current distribution around the slot [66] can no longer radiate. In addition to achieving omnidirectional behavior, placement of the cavity also preserves the input impedance of the slot antenna, therefore minimizing the sensitivity of the antenna to its surrounding environment.

Despite the implementation of the cavity, there are additional issues that must be ad-

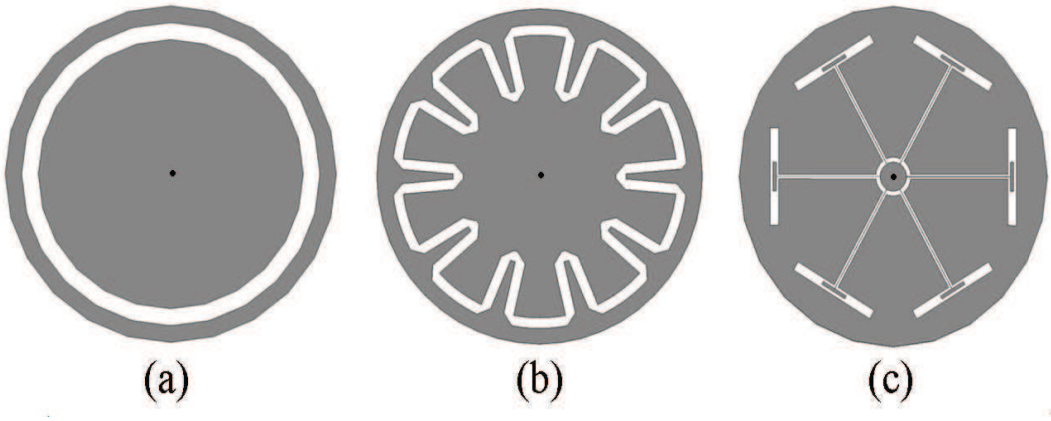

Figure 4.2: Topology of cavity-backed slot loop antennas. (a) Original slot loop. (b) Modified slot loop for size reduction. (c) Sectionized slot loop for input impedance matching.

dressed to effectively realize the magnetic dipole antenna. First, a constant current distribution around the circular slot must be assured to achieve omnidirectional radiation in the horizontal plane. Figure 4.2 (a) shows the geometry of a slot loop antenna. However there is much difficulty to match a small cavity backed slot loop antenna to a transmission line. The small slot loop has an open-circuit characteristic and low radiation resistance. To ensure effective radiation off a small loop, significant magnetic current has to be induced in the loop. Without an external matching network, this can only be accomplished if the structure is at an electromagnetic resonance condition. But we are looking for antennas with small electrical dimensions. By modifying the loop in a compact fashion as shown in Figure 4.2 (b) the dimension can be greatly reduced. However, omnidirectionality and feeding remains problematic. Therefore, to accomplish resonance and achieve sufficient input impedance matching, the magnetic loop can be sectionized into a number of $\lambda/2$ slot antennas around a circle. Figure 4.2 (c) shows the conceptual geometry of the proposed composite slot loop antenna. Of course this geometry is electrically large and has to be modified, but is shown here to show the feed mechanism. As shown, each slot antenna is capacitively fed with a stub. Such structure eases the difficulty of matching the composite slot loop antenna.

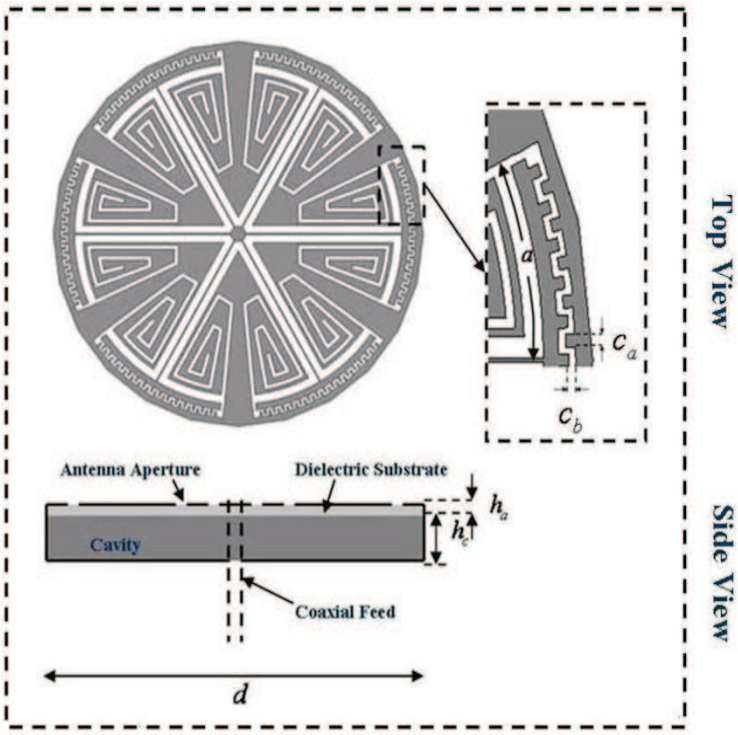

Figure 4.3: Topology of the reduced-size-cavity-backed composite slot loop antenna. The corrugated capacitive stub is shown in the top right corner.

The next step is to miniaturize the geometry of the antenna. It has been shown that the physical dimension of a resonant slot antenna can be reduced significantly by loading a short slot section by inductive loads on the edges [21]. The spiral-like geometry of the inductive slotlines are designed for miniaturization purposes. In this chapter, a similar technique is applied to design a compact, omnidirectional antenna. The dimension of the proposed six-element composite slot loop antenna is reduced significantly. Figure 4.3 shows the modified geometry of the proposed miniaturized slot loop antenna. In addition to miniaturization, by folding the edges of each slot antenna in a spiral-shape fashion in close proximity to one another, an omnidirectional behavior can be achieved. Basically, the magnetic currents flowing on the folded edges are negated with the magnetic currents flowing on the edges of the adjacent slot antenna. Therefore the outer rings of the folded slots are left to display a circular current distribution, similar to a slot loop antenna. However, each segment of the antenna is at its fundamental electromagnetic resonance ensuring

significant current flow that give rise to high radiation resistance and negligible reactance near the resonance. The antenna is then placed on the top surface of a cylindrical-shaped cavity. The sidewalls and the bottom of the cavity is metallized. This implementation allows the electric currents on the surface of the circular slot antenna to flow along the very short sidewalls of the cavity ($\ll 0.01\ \lambda$), creating a radiation behavior similar to that of a vertical wire. This is another physical explanation of how a cavity-backed small magnetic loop antenna radiates vertical polarization in the plane of the antenna.

4.2.2 Antenna Feed and Matching

Electrically small antennas often require large impedance transformation matching circuit due to their low resistance and high reactance. When using external matching networks, even those with relatively high Q components, significant loss due to resistance is commonplace. Therefore it is desired to match an electrically small antenna with passive elements while preserving its small dimension. For the miniaturized composite slot loop antenna, a coax feed is used to feed the antenna from the center of the geometry. The coax feed is connected to six co-planar wave guides (CPW) to feed each of the slots separately. In order to match the six parallel CPW lines to the 50Ω coax feed, the CPW must be adjusted to 300Ω. Typically for low dielectric constants, the center conductor of the CPW at high impedance is rather narrow for electrically small antennas, sometimes beyond the fabrication capability. As a result, the width and the gap of the CPW lines were modified to 200Ω CPW lines. At the edges of each CPW lines, stubs are attached to feed each of the slots capacitively. Miniaturized slot antennas fed at the center near their resonance show relatively high input impedance and therefore it is easier to match them to high impedance transmission lines. As seen from Figure 4.3, the coupling stubs are corrugated in order to control the capacitance and thus, improve impedance matching to the slot. The impedance matching is adjusted by modifying parameters c_a and c_b in corrugation of the stubs.

4.3 Antenna Simulation and Measurement

The proposed miniaturized cavity-backed slot loop antenna is designed and simulated using method of moments (MoM) based commercial simulation tool [34]. The length of the slot line, the width of the CPW lines, and the dimension of the corrugated matching stubs were computed and optimized using full wave simulations. Impedance matching is initially achieved by simulating the antenna structure using perfect conductor (PEC) material settings in order to exclude ohmic loss and loss from dielectric. Infinite substrates are used in the MoM solution to reduce the high memory requirement and simulation time. After matching is optimized, loss parameters are introduced to estimate the efficiency of the antenna with exact substrate dimension using Ansoft's HFSS. To confirm the intended current distribution and pattern behavior, the magnetic current distribution on the slot structure of the antenna is simulated and shown in Figure 4.4. It is clearly demonstrated that the magnetic currents along the circular arc of individual elements are all traveling in the same direction with uniform magnitude. Also, the magnetic current flowing along the spiral arms of adjacent elements are in opposite directions. The simulation result using of the radiation pattern in the far field using HFSS is shown in Figure 4.5. It has been proven in Chapter 2 that bandwidth and radiation efficiency of a cavity-backed antenna can be improved by increasing the height of the cavity.

To study the effect of the height of the cavity on the slot loop geometry, an additional antenna having pertinent dimension and topology with a cavity height (h_c) twice as high is designed and simulated. The slot length and corrugations on the matching stub are adjusted to compensate the change of resonant frequency caused by the increase cavity height. The physical properties of the antennas are presented in Table 4.1. Parameters h_a and h_c are shown in Figure 4.3.

The designed antenna is then built and fabricated on a $0.5mm$ thick RO4003 substrate (h_a) from Rogers Corp. The substrate has a dielectric constant of $\varepsilon_a = 3.4$ and loss tangent of $\tan\delta_a = 0.0027$. The fabricated miniaturized slot loop antenna has an overall diameter

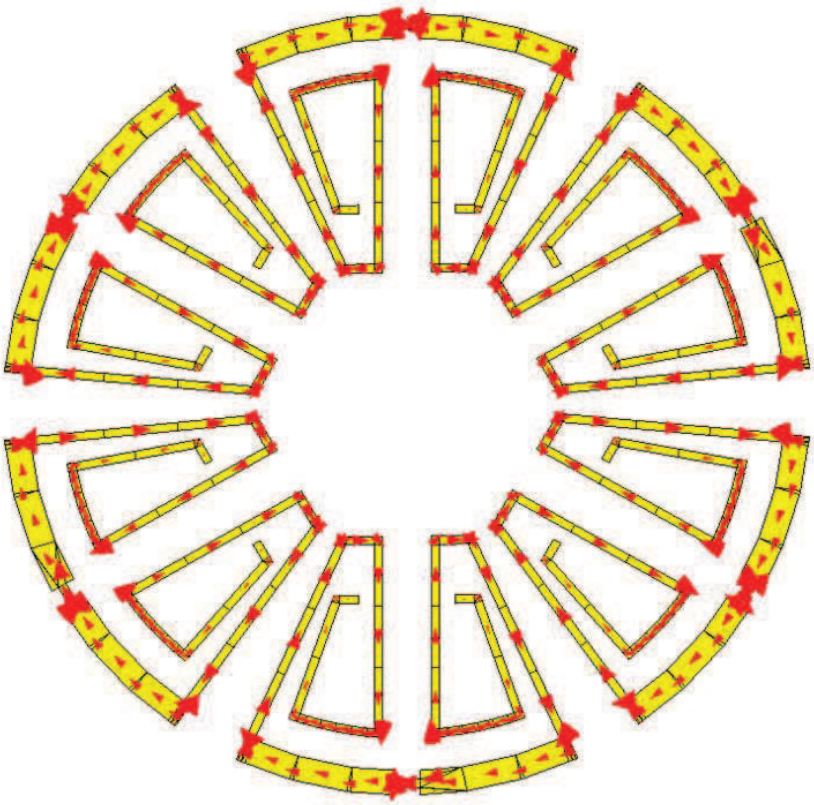

Figure 4.4: Simulated magnetic current distribution of the reduced-size-cavity-backed composite slot loop antenna.

of $10cm$, less then $\lambda/7$ in electrical dimension. Via holes are drilled along the edges of the antenna platform and wires are soldered. The cylinder-shaped cavity is fabricated by machining a piece of $6.35mm$ thick TMM3 substrate (Rogers Corp), which has a dielectric constant of $\varepsilon_c = 3.3$ and loss tangent of $\tan\delta_c = 0.0020$. The bottom of the cylindrical cavity is metallized to create an electrical ground. The fabricated antenna substrate is then placed on top of the cylindrical cavity and the wires fastened through Via holes to the antenna are soldered to the bottom surface of the cavity to electrically connect the antenna to the cavity. Finally, a Via hole at the center of the cavity-backed antenna is drilled and a coax feed is connected from the bottom of the cavity. The fabrication process is repeated for the antenna with cavity height of $12.7mm$. The photograph of the fabricated antenna is shown in Figure 4.6.

Antenna Type	c_a	c_b	h_a	a	d
CBCSLA with $h_c = 6.35mm$	1.2	0.7	0.5	18.3	100
CBCSLA with $h_c = 12.7mm$	0.6	0.6	0.5	18.3	100

Table 4.1: Physical dimensions of cavity backed slot loop antennas. All dimensions are in *mm*

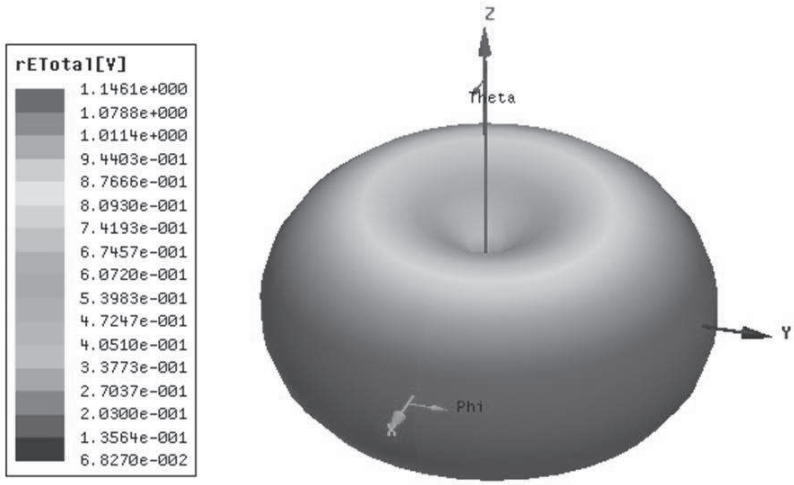

Figure 4.5: Simulated radiation pattern of the reduced-size-cavity-backed composite slot loop antenna.

The input reflection coefficients of the fabricated antennas are measured using a calibrated HP8720D vector network analyzer and the results are shown compared to simulations in Figure 4.7 and Figure 4.8. The slight deviation between simulation and measured results is caused by possible errors associated with the numeric simulations, fabrication errors and material tolerances. Both antennas display more than -10 dB reflection coefficients at resonance, indicating good impedance matching. The CBCSLA is designed assuming the antenna will be placed on a large ground plane. However, it is important to mention that impedance matching varies slightly as a function of the ground plane size when the dimension of the ground plane is comparable to the dimension of the CBCSLA. In this case the induced current on the small ground plane attached to the CBCSLA modifies the radiation to some extent. In situations where only small area of ground plane is available on the platform, in order to reduce the effect of the finite ground plane a thin layer of dielec-

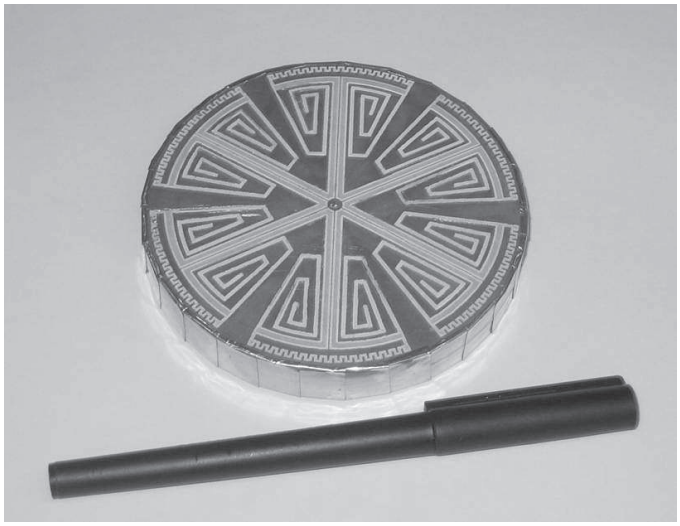

Figure 4.6: Photograph of the fabricated of the reduced-size-cavity-backed composite slot loop antenna. The coaxial feed is not shown.

tric is placed between the CBCSLA and the finite ground plane. To demonstrate this, we consider the CBCSLA designed in the previous example over a finite ground plane using a teflon dielectric spacer of thickness of $2mm$ and diameter of $50mm$. The setup is shown in Figure 4.9. The input reflection coefficients of the antenna on a finite ground plane with and without the dielectric spacer is simulated as a function of the radius of the ground plane and the results are shown in Figure 4.10. The simulated results indicate the effect of the finite ground plane can be minimized by placing an insulating layer between the CBCSLA and the finite ground plane. The far-field co-polarized ($|E_\theta|^2$) and ($|E_\phi|^2$) radiation patterns of the antennas are measured in the anechoic chamber at the University of Michigan. The measured E- and H-planes of the antennas with cavity height of $6.35mm$ and $12.7mm$ are presented in Figure 4.12 and Figure 4.13, respectively. For the E-planes, nulls can be seen at $\Theta = 90^\circ$, resembling that of a wire dipole antenna. Therefore if the antenna is placed on a large ground plane, a greater null will be displayed.

As observed from Figure 4.13, the measured antennas display an omnidirectional radiation behavior. Cross-polarization radiations are mostly caused by the close proximity of the feed network cable. Relatively high levels of currents from the electrically small antenna

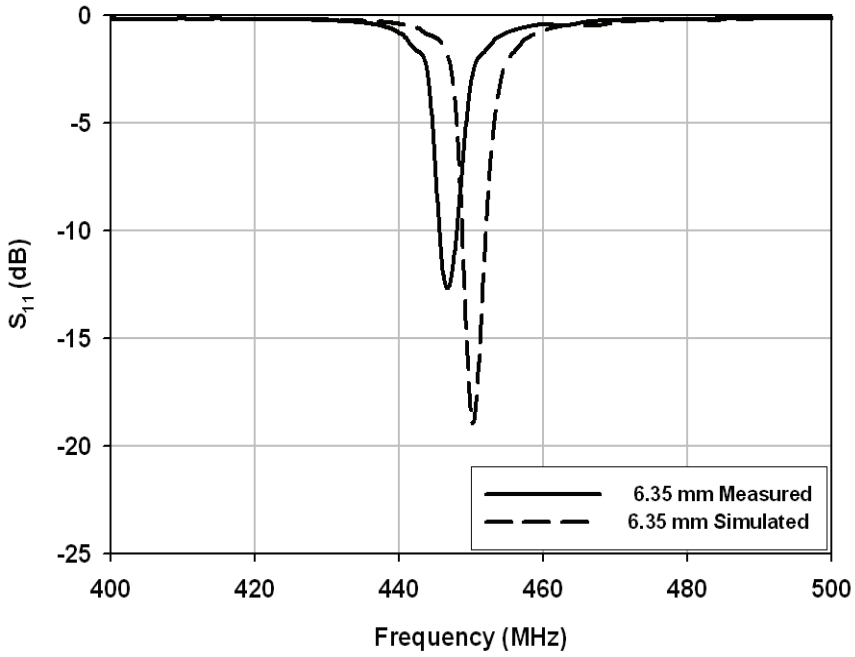

Figure 4.7: Measured and simulated S_{11} response of the reduced-size-cavity-backed composite slot loop antenna with $h_c = 6.35mm$.

are induced on the nearby cable, causing the currents on the cable to reradiate. This can be confirmed by the change of cross-polarization pattern in Figure 4.13 as the orientation of the cable connected to the measured antennas are changed. Despite the effect of the feeding network, the measured cross polarization radiations remains significantly lower in the H-plane.

Antenna Type	BW (%)	Gain (dBi)	Directivity (dBi)
CBCSLA with $h_c = 6.35mm$ $(\lambda/120)$	0.7	-3.7	1.6
CBCSLA with $h_c = 12.7mm$ $(\lambda/60)$	1.1	-1.5	1.6

Table 4.2: Radiation Parameters of the reduced-size CBCSLAs

The gain of the antennas are measured in the anechoic chamber using a dipole antenna with known gain as a reference and the results are presented in Table 4.2. The directivity of the measured antennas are computed using numerical simulations, and the efficiencies of the antennas are calculated. It can be observed that by increasing the height of the

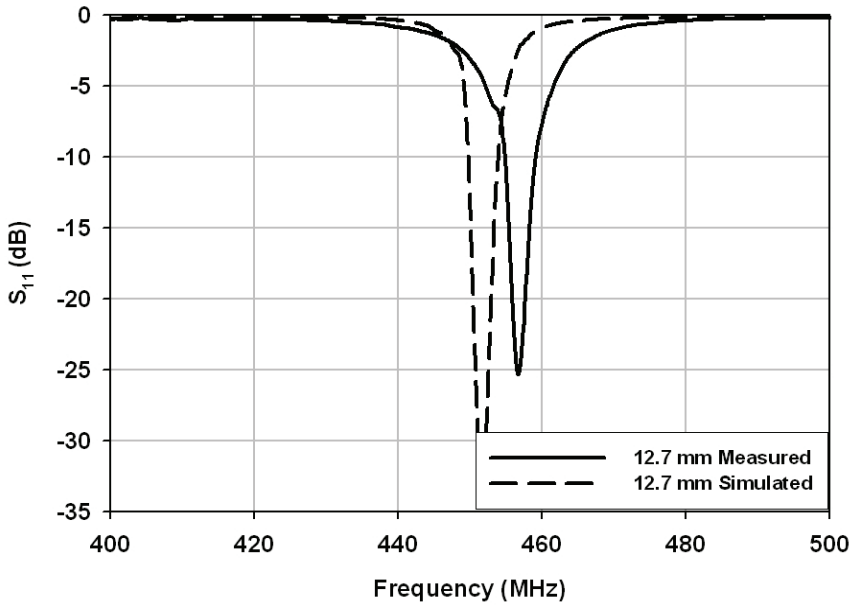

Figure 4.8: Measured and simulated S_{11} response of the reduced-size-cavity-backed composite slot loop antenna with $h_c = 12.7mm$.

cavity, the 2:1 VSWR bandwidth is improved and the gain of the antenna increases by 2.2 dB. The improved bandwidth and efficiency remains relatively lower than that of a half wave wire dipole antenna. This can be explained due to the relatively large amount of energy trapped inside the cavity (high Q). As ε increases, the fields generated by the antenna tends to be stored within the dielectric material, causing less fields to radiate into the far-field region. However, the measured antenna is several orders of magnitude smaller compared to traditional dipole antennas. The bandwidth and efficiency of the cavity-backed miniaturized composite slot loop antenna can be further improved through various methods such as higher quality dielectric, increasing the height of the cavity, or introducing certain boundary conditions such as perfect magnetic conductor (PMC) at the bottom of the cavity.

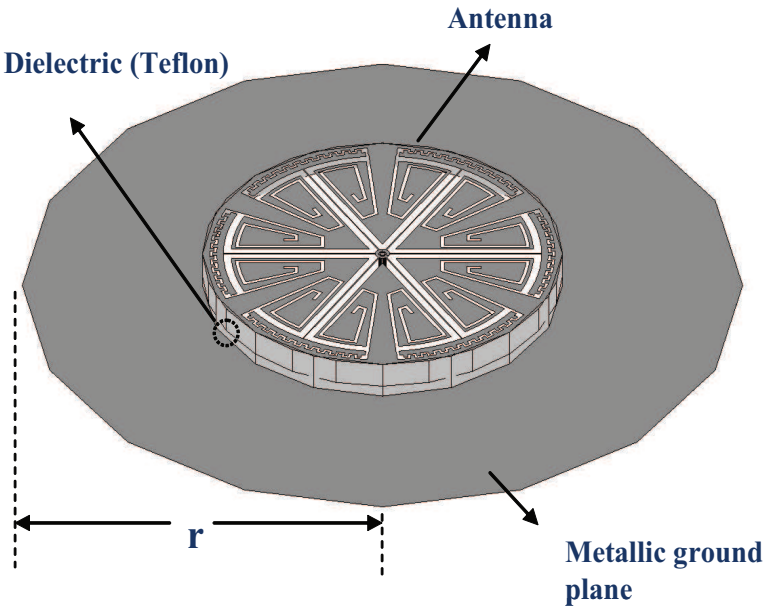

Figure 4.9: Simulation setup of the CBCSLA on a metallic ground plane. A cylindrical dielectric spacer is placed between the CBCSLA and the ground plane.

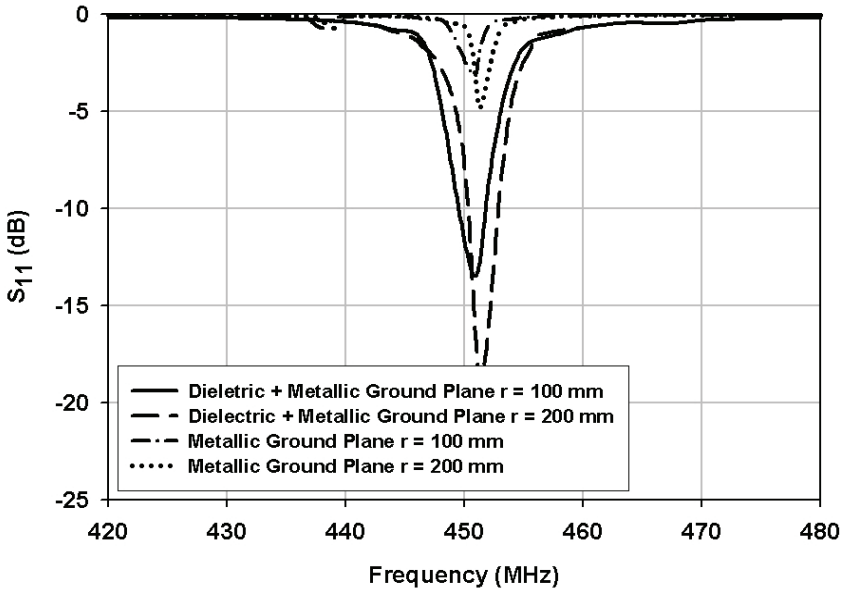

Figure 4.10: Simulated S_{11} responses of the CBCSLA on a metallic ground plane as function of the dimension of the ground plane. Responses with and without a dielectric spacer between the CBCSLA and the ground plane are presented. The radius of the CBCSLA is 50mm .

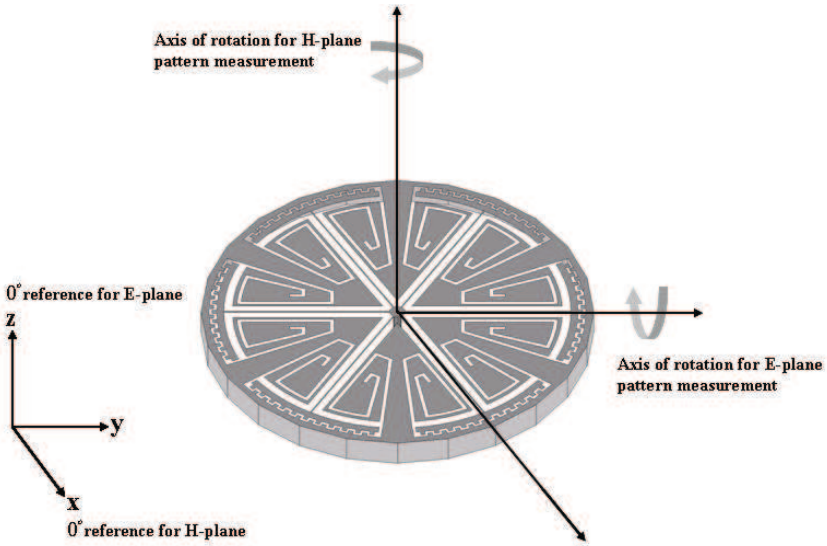

Figure 4.11: Characterized E- and H-plane pattern measurement setup of the fabricated antenna. Co- and cross-pol patterns are measured in these two planes.

Figure 4.12: Measured E-plane radiation patterns of the reduced-size-cavity backed composite slot loop antennas (a) $h_c = 6.35mm$. (b) $h_c = 12.7mm$. Solid Line: Co-Pol, Dash line: Cross-Pol.

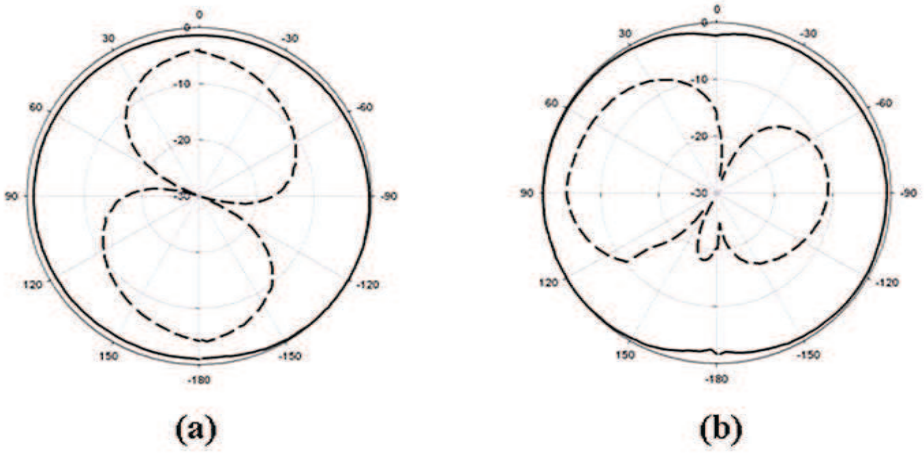

Figure 4.13: Measured H-plane radiation patterns of the reduced-size-cavity backed composite slot loop antennas (a) $h_c = 6.35mm$. (b) $h_c = 12.7mm$. Solid Line: Co-Pol, Dash line: Cross-Pol.

4.4 Dual-band Antenna Design

Antennas with multiple frequency operation capabilities are of great interest in numerous wireless applications. Multi-band antennas can be used for transmitting and receiving at different frequencies or used for multiple applications simultaneously, making such antennas versatile and efficient. In this section, the geometry of the cavity-backed miniaturized composite slot loop antenna is further investigated to achieve dual band capabilities while retaining its characteristic behaviors and small physical dimension.

As mentioned earlier, the six miniaturized slots determine the resonance of the proposed antenna. Therefore, if the folded slot elements are of different length, multiple resonant conditions can be achieved. Naturally, matching the antenna at different frequencies become an important task. Parasitic coupling mechanism is a common technique that is used to achieve broadband/multiband antennas due to its absence of transmission zeros. The miniaturized CBCSLA is further modified by varying the lengths of three non-adjacent slots to resonate at higher frequency. The three non-adjacent slots are parasitically coupled

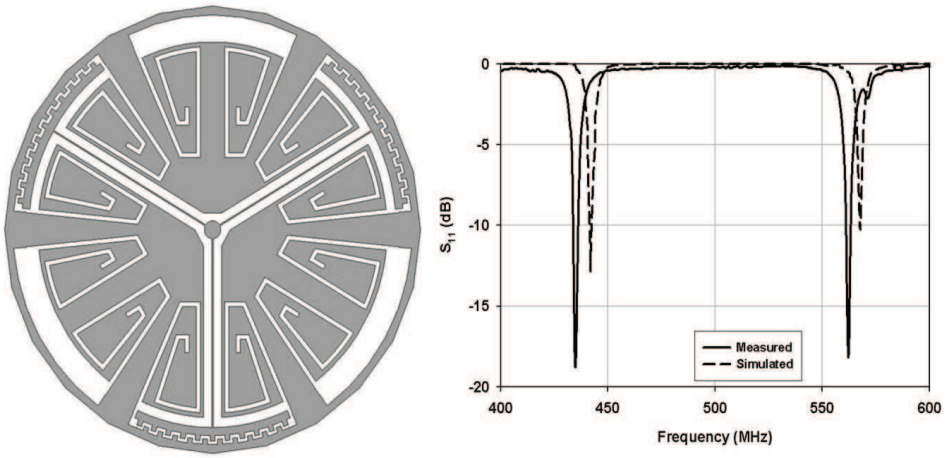

Figure 4.14: Topology of the fabricated dual-band CBCSLA and its S_{11} response.

to the original three slot elements which are fed through the identical feeding mechanism as the single band CBCSLA. Matching at both frequencies is achieved identically as well, by adjusting the dimension of the capacitive stubs. The overall physical dimension of the antenna remains the same as before the modification. The dual band CBCSLA is designed and fabricated, and the topology and measured and simulated input reflection coefficients are shown in Figure 4.14. The measured radiation parameters are presented in Table 4.3.

Center Frequency	BW (%)	Gain (dBi)	Directivity (dBi)
434 MHz	0.7	-3.4	1.8
562 MHz	0.5	-3.2	1.7

Table 4.3: Radiation Parameters of the dual band CBCSLA with $h_c = 6.35\ mm$

However, sectionizing the original six element spiral slots to different lengths to achieve multiple resonances makes it difficult to achieve the desired omnidirectional radiation behavior. A semi-constant current distribution on the outer rings of the antenna is no longer achieved at a particular resonant frequency due to different electrical behaviors of adjacent slot elements. Thus, pattern distortion and rise of cross-pol levels are expected. To preserve the dipole-like pattern while achieving a dual-band operation, two different sets of three-element folded slots are designed to interwind each other to reduce the physical dimension while achieving the desired current distribution. One set of folded slot elements

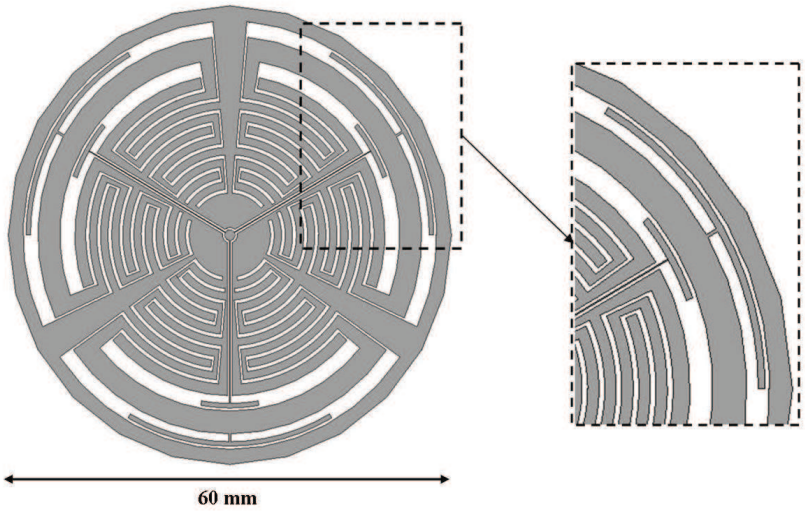

Figure 4.15: Topology of the modified dual-band CBCSLA. The matching stubs are shown in the right.

are parasitically coupled to the other, which is fed through the CPW-coaxial connection as before. Matching is achieved by controlling the dimensions of the capacitive stubs for both frequencies. The topology of the modified dual-band CBCSLA is shown in Figure 4.15. The antenna is simulated and its input reflection coefficients and magnetic current distribution are shown in Figure 4.16. The antenna displays resonant behavior at 467 MHz and 736 MHz with 0.6% and 0.5% 2:1 VSWR respectively. The simulated magnetic current distribution presented in Figure 4.17 behaves similar to that of the single-band CBCSLA. Figure 4.18 indicates the simulated patterns of the dual-band CBCSLA also resemble the measured patterns of the single-band CBCSLA. Therefore, by using similar geometry, miniaturized cavity-backed composite slot loop antennas with multi-band capabilities can be achieved while minimizing pattern distortions.

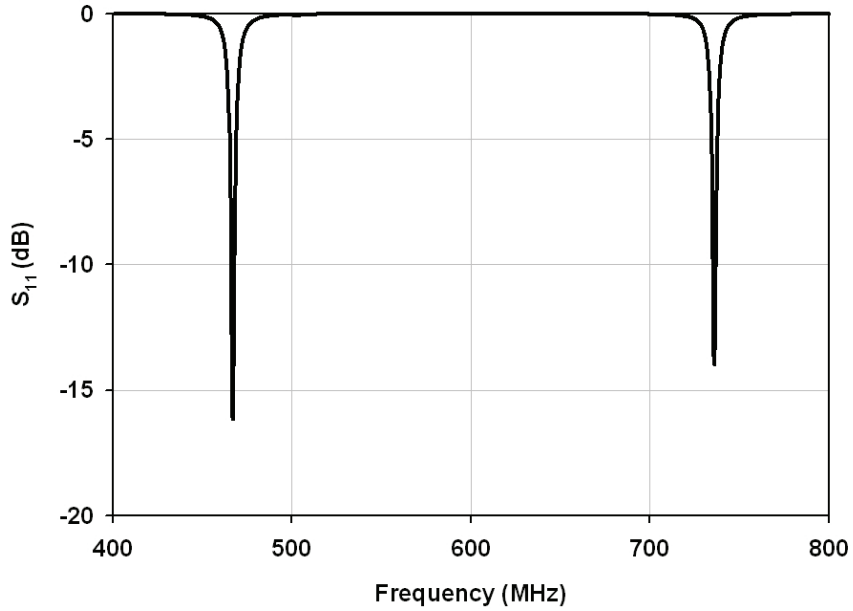

Figure 4.16: Simulated S_{11} response of the modified dual-band CBCSLA.

4.5 Summary

A process for designing a new class of miniaturized low profile antennas with vertical polarization is proposed and discussed in this chapter. Through this method, a composite magnetic loop with close-to-constant current distribution is realized. The loop is easily matched by adjusting the geometry of the feed. The antenna's lateral dimension is significantly reduced by modifying the geometry of constituent resonant slot sections. The cavity-backed composite slot loop antenna displays omnidirectional radiation behavior in the vertical polarization plane, emulating a dipole antenna with a vertical height less than $\lambda/100$. Such radiation performance with very low profile enables the proposed antenna to be applicable for automotive and Unattended Ground Sensor network modules. Despite its small physical dimension, the antenna displays excellent matching, high directivity and moderate efficiency. Furthermore, additional techniques are introduced and proposed to improve the performance of the antenna and achieve dual-band operation capabilities.

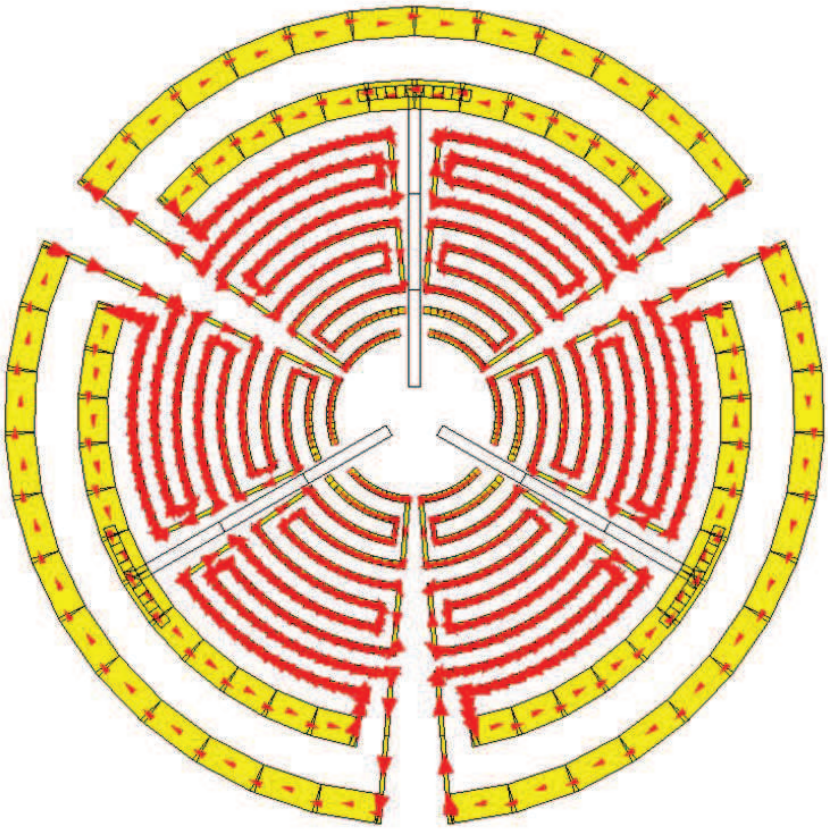

Figure 4.17: Simulated magnetic current of the modified dual-band CBCSLA.

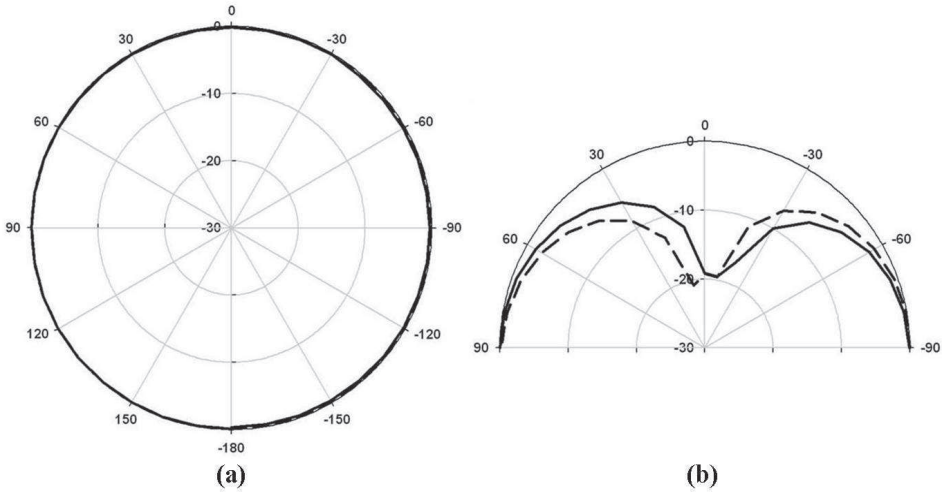

Figure 4.18: Simulated radiation patterns of the modified dual-band CBCSLA (a) H-Plane. (b) E-Plane. Solid Line: 467 MHz, Dash line: 736 MHz.

CHAPTER 5

The Multi-element Monopole Antenna

The cavity-backed composite slot loop antenna (CBCSLA) introduced in the previous chapter involves modification of the slot aperture topology. Measurement confirms behavior similar to that of an ordinary infinitesimally small dipole antenna. However, the CBCSLA requires a relatively complicated and multi-step fabrication process involving extensive machining and lithography. In this chapter, we resort to the complementary equivalent of a slot antenna - a half-wave dipole antenna to devise an antenna design that has similar performance as that of a CBCSLA while simplifying the topology and fabrication process.

5.1 Introduction

The half-wave dipole antenna is perhaps one of the most fundamental and commonly used antennas ever since the discovery of electromagnetic wave radiation. From the early stages to present, the dipole antenna and its variations have been extensively used in the field of wireless communication for its simple geometry and reliability. In addition when the antenna is vertically mounted, the dipole antenna features an omnidirectional radiation pattern, making it useful for terrestrial applications, non-line-of sight conditions, and situations where transceiver modules are often deployed randomly. Monopoles that emulate virtually identical performance behaviors as that of a dipole antenna are often used at lower

frequencies. Therefore it is imperative to further investigate methods of realizing extremely short monopole antennas with very small lateral dimensions. This will allow integration of such antennas with the wireless device package or platform.

A variety of space filling compression techniques have been studied to reduce the vertical profile of monopole antennas [2, 3, 4]. The dimension of a wire monopole antenna is greatly reduced by folding the monopole antenna geometry through several iterations. In [35], metallic paths patterned after Peano and Hilbert curves are used to greatly reduce the vertical profile of monopole antennas. The Peano-curve top-loaded monopole features a vertical height of approximately $\lambda/12$ while featuring excellent monopole radiation pattern. In addition, a meandered monopole antenna is further modified by extending a conductor line for the end of a rectangular meander monopole to achieve a dual-band operation [67]. In [5, 6], various fractal antennas are further investigated and the resonant properties, bandwidth, and impedance matching of compressed omnidirectional antennas are reported.

The vertical height of a monopole antenna can also be reduced through antenna loading techniques. In [68], the antenna is loaded with a dielectric cylinder and a dual-band behavior is realized. A monopole antenna is inductively loaded and its electrical characteristic is studied [69, 70]. In [71, 72, 73, 74, 75, 76], low-profile, omnidirectional antennas are devised by capacitively loading monopole antennas with modified disks. The heights of the proposed antennas are in the range of $\lambda/10$. In addition, these antennas feature excellent operational bandwidth. However, the lateral dimension of the antennas are comparable to wavelength. Nonetheless, the impact of the Goubau antenna [76] is significant in the antenna community due to the fact that it closely approaches Chu's fundamental limit. However, because of its complex geometry, the Goubau antenna is difficult to be analyzed using conventional methods. In [77], the Goubau antenna is thoroughly analyzed using full-wave simulations. Recently, artificial electromagnetic materials such as electromagnetic band-gap (EBG) structures have been incorporated with conventional wire antennas to feature a low-profile antenna that behave equivalent to a vertical monopole antenna [78].

This chapter presents a low-profile antenna with omnidirectional vertically polarized radiation similar to that of a traditional monopole antenna using a different approach. The proposed antenna is realized by modifying the geometry of a quarter-wave microstrip type resonator to emulate an electrically small antenna with a very small vertical profile. The concept is based on superposition of multiple quarter-wave segments that are meandered and spiraled around to virtually negate the radiation from horizontal currents above the ground plane. As a result, the antenna features a vertically polarized radiation in the horizontal plane. The design and miniaturization method for the antenna is presented in Section 5.2. Simulation and measurement results are also shown and discussed. The antenna is further modified and parametric studies are done in Section 5.3. In Section 5.4, a dual-band multi-element monopole antenna is designed and its measurement results are presented and discussed.

5.2 The Miniaturized Multi-Element Monopole Antenna

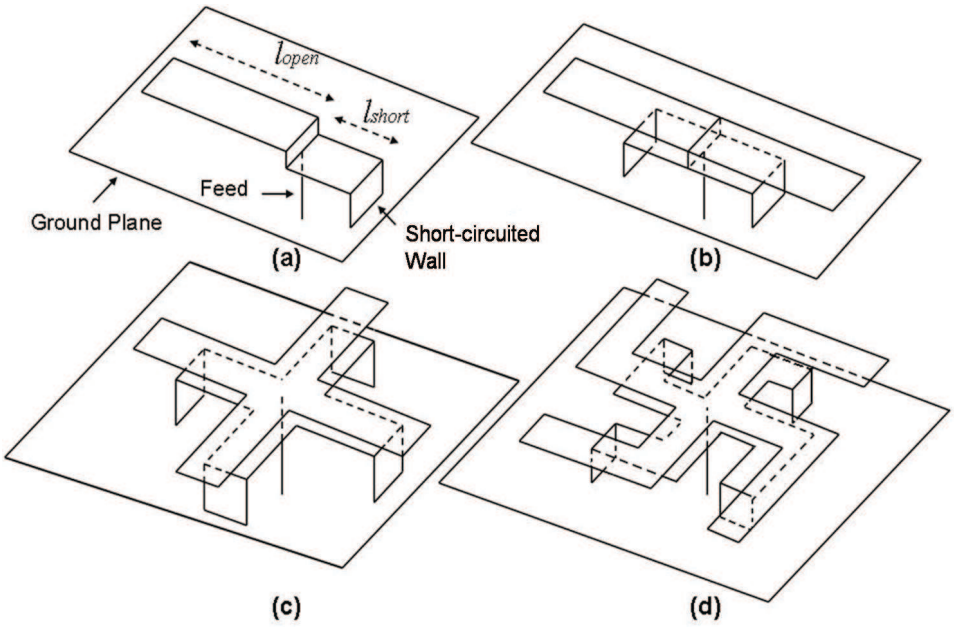

Figure 5.1: Design process of the miniaturized multi-element monopole antenna.

Radiation powers from short monopole antennas are proportional to the currents in-

duced on them. In practice the level of induced current is limited by the impedance mismatch between the transmission line and the very small radiation resistance of such radiating structures. External matching networks based on lumped elements are lossy which render a rather poor radiation efficiency. One approach to increase the induced electric current on a short segment of a vertical wire above a ground plane is to use the vertical wire as part of a resonant structure. The smallest resonant structure can be formed from a quarter-wavelength segment of a transmission line short-circuited at one end and open-circuited at the other end (i.e. monopole). Consider a microstrip line resonator formed by a strip above the ground plane and short-circuited by a small vertical wire. This resonator can be fed from the center as shown in Figure 5.1 (a). Impedance matching of this quarter-wavelength resonator (monopole) is facilitated by adjusting the feed position along the resonator and choosing parameters l_{open}, the open-circuited segment and l_{short}, the short-circuited segment. It is expected that the current flowing on the microstrip itself does not contribute to the total radiated field due to cancelation of the far-field by its image in the ground plane. The directions of the currents at the feed point and on the short-circuited vertical wire are opposite of each other; however, the magnitude of current at the short-circuited wire can be significantly higher from which the net radiation emanates. The electric current flowing on the vertical element of the antenna is responsible for the vertically polarized radiation. If the horizontal electric current can be effectively eliminated we can achieve a completely vertically polarized radiation ignoring the lateral electrical dimension for the time being. Cancellation can be done by adding another monopole element while sharing the same feed as seen in Figure 5.1 (b). The cancellation of the horizontal electric current is achieved by introducing another set of electric current that is in the opposite direction in the horizontal plane of the antenna with the original electric current at electromagnetic resonance. In contrast, the vertical electric currents flowing on the short-circuited pins of each elements is in phase and as a result, behaves as the radiating elements of the antenna. Thus, the two-element monopole antenna behaves as a small vertically polarized antenna. To achieve

omnidirectional radiation patterns in the horizontal plane of the antenna while maintaining low levels of cross-polarization levels, it is important for the antenna to be electrically small and symmetric. Additional monopole elements are added in similar ways to negate the horizontal currents. The increased number of short-circuited pins provides increased number of radiators and improves the mechanical stability of the multi-element monopole antenna. Parameters l_{open} and l_{short} must be modified to accommodate for the changes in impedance caused by the additional monopole elements. The topology of the four-element monopole antenna is presented in Figure 5.1 (c).

The proposed topology of the the multi-element monopole antenna enables the height of a traditional monopole antenna to be greatly reduced. However, as the height of the multi-element monopole antenna reduces, the lateral dimension increases. The miniaturization of the multi-element monopole antenna is achieved by folding the open-circuited segments of the antenna in a spiral-shaped geometry so the cancelation of horizontal electric currents on the elements is maintained. To achieve miniaturization, the short-circuited segments of the antenna can also be meandered and placed slightly below the spiral layer. A sketch of a miniaturized multi-element monopole antenna is visualized in Figure 5.1 (d). The overall length of each quarter-wavelength segment must be adjusted using a full-wave approach to take the effects of near field mutual couplings into account.

The miniaturized multi-element monopole antenna is designed using Ansoft's HFSS. The topology of the simulated antenna is presented in Figure 5.2. Parameters are optimized to achieve operation around 460 MHz with lateral dimensions less than $\lambda/10$ and the height to be around $\lambda/30$. The open-circuited elements and the short-circuited elements are designed on two separate vertical layers with $1mm$ spacing for enhanced space conservation and compactness. The open-circuited elements are folded in a spiral-liked fashion and minimized to $W_c \times L_c = 56mm \times 56mm$ in lateral dimension. The total length of the open-circuited element (l_{open}) is $117mm$. The miniaturized open-circuited elements are fed by a single wire feed. The meandered short-circuited elements are designed to be

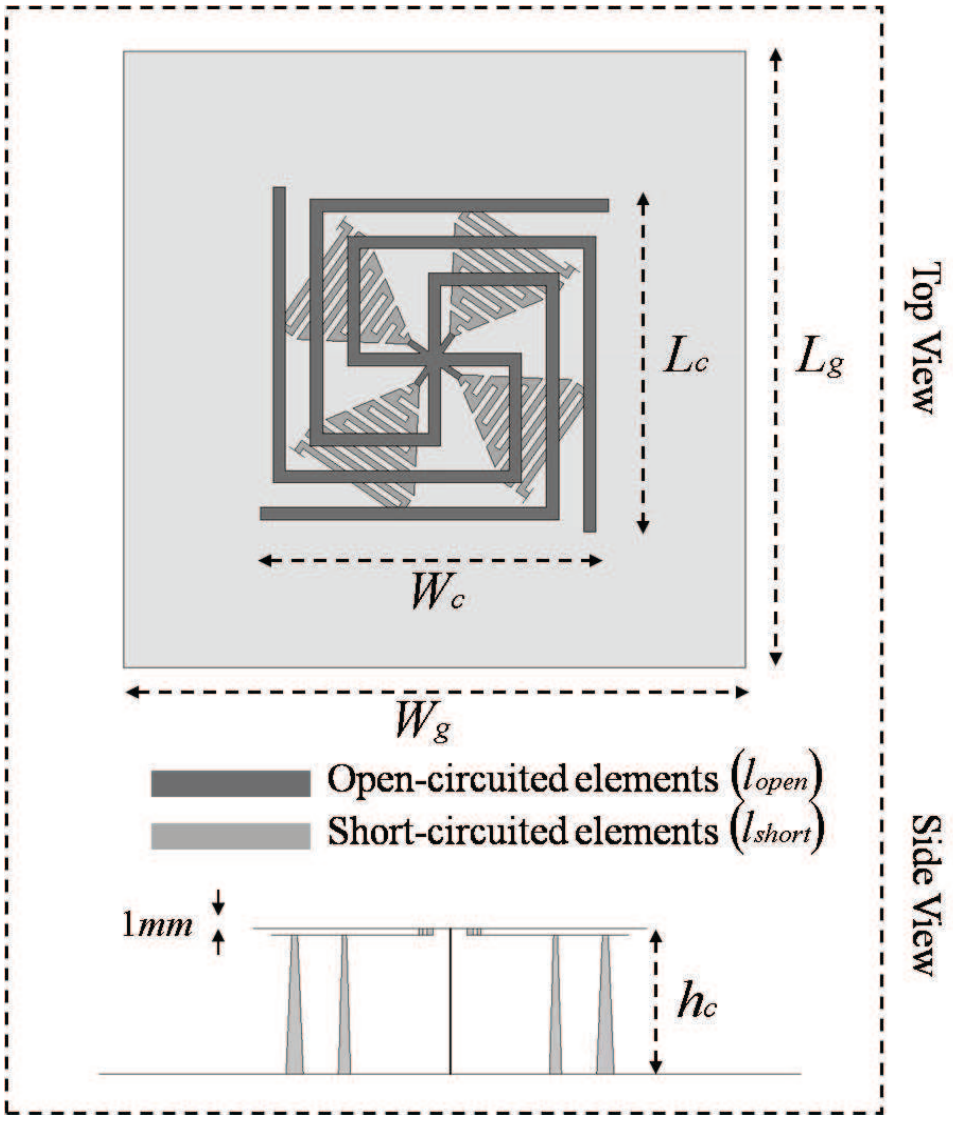

Figure 5.2: Topology of the miniaturized multi-element monopole antenna.

placed $1mm$ beneath the miniaturized open-circuited elements. The elements in both layers are electrically connected by four vertical pillars with a height of $1mm$. The short-circuited pins are connected to each end of the four short-circuited elements respectively. The total length from the vertical pillar to the short-circuited pin (l_{short}) is $94.6mm$. Impedance matching of the miniaturized multi-element monopole is achieved by adjusting the length of the meandered short-circuited elements. The antenna is then fabricated on a $0.3mm$ thick copper sheet. The open-circuited and short-circuited elements on each vertical layers are milled separately and soldered together. A $1mm$ thick dielectric spacer is placed between

the two layers to minimize fabrication and simulation discrepancies. The short-circuited pins are milled to be $20mm$ in height (h_c) and then soldered to each ends of the meandered short-circuited elements respectively. The short-circuited pins are then soldered to a $W_g \times L_g = 100mm \times 100mm$ copper ground plane. The final height of the fabricated antenna is $21.3mm$.

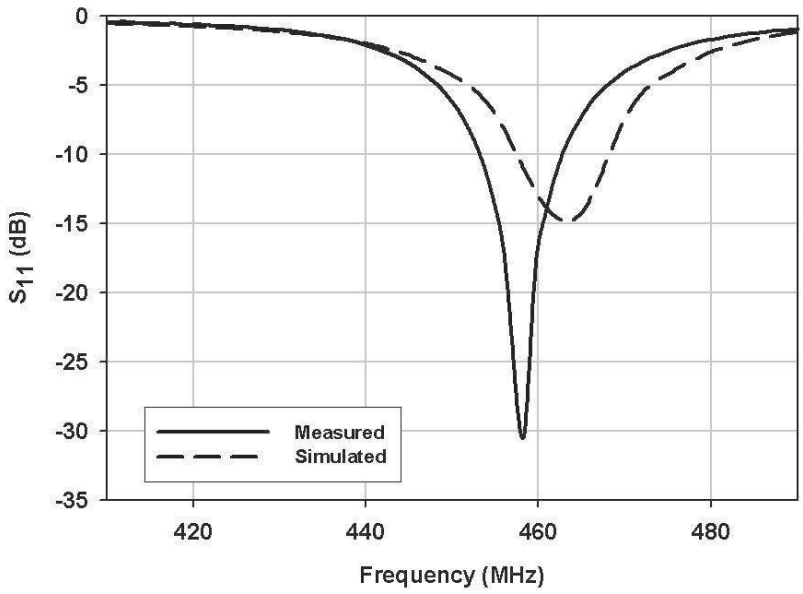

Figure 5.3: Measured and simulated S_{11} response of the miniaturized multi-element monopole antenna.

Figure 5.3 shows the simulated and measured input reflection coefficient of the proposed antenna. The fabricated antenna features 3% 2:1 VSWR bandwidth. The slight discrepancy between the simulated and measured responses can be attributed to alignment errors during the fabrication process. The radiation patterns of the miniaturized multi- element monopole antenna is measured in the anechoic chamber of the University of Michigan at the resonant frequency of 460 MHz. Figure 5.4 shows the E- and H- Plane, co- and cross-polarized patterns of the antenna. The measured antenna features omnidirectional radiation pattern in the H-Plane, similar to a monopole. In addition, a null is observed at $\Theta = 0^\circ$ in the E-Plane. Cross-polarization levels in both planes are mainly caused by the close prox-

imity of the feed network cable and the small ground plane size. This can be confirmed with simulated radiations patterns of the featured antenna on an infinite ground plane as presented in Figure 5.5. The gain of the miniaturized multi-element monopole antenna is measured in the anechoic chamber using a dipole antenna with a known gain. The gain is measured to be -4.1 dBi . The directivity is calculated to be 1.0 dBi . For such electrically small ground plane dimension ($\lambda/7 \times \lambda/7$) the effect of the edge currents on the ground plane becomes significant to the the radiation pattern, directivity, and gain of the proposed antenna. Strong levels of edge currents result in the rise of cross-polarization levels, increased ohmic loss leading to degradation of directivity and gain. In addition, the low gain suggest that relatively high levels of currents on the open-circuited and short-circuited elements may be causing ohmic loss. Therefore it is important to further investigate the topology of the antenna and the effects of the ground plane.

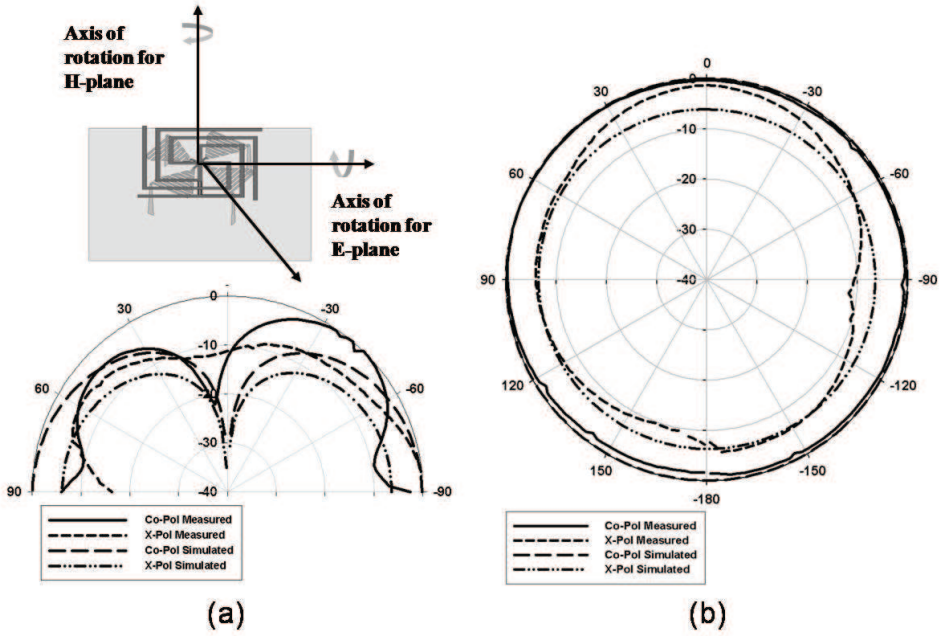

Figure 5.4: Measured and simulated radiation pattern of the miniaturized multi-element monopole antenna. (a) E-Plane. (b) H-Plane.

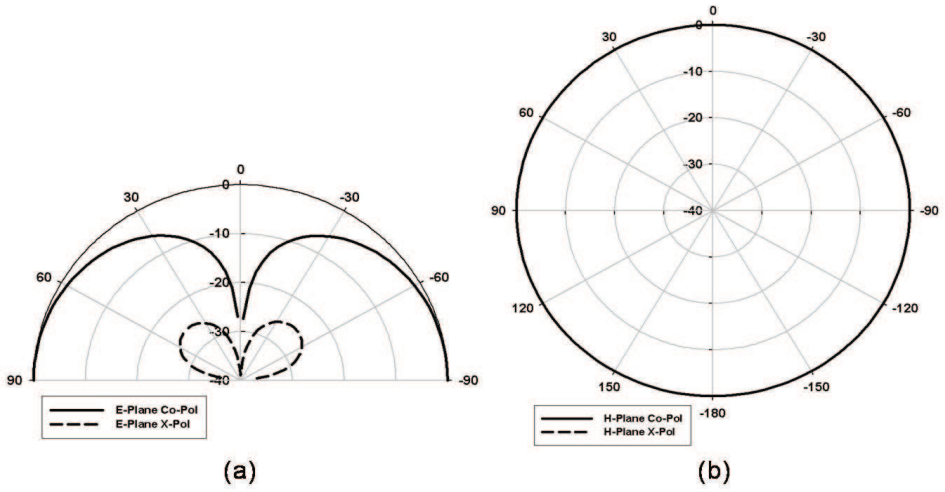

Figure 5.5: Simulated radiation pattern of the miniaturized multi-element monopole antenna on an infinite ground plane. (a) E-Plane. (b) H-Plane.

5.3 The Modified Multi-Element Monopole Antenna

5.3.1 Antenna Design

Now that the functionality of the proposed miniaturized multi-element monopole antenna has been established, additional modifications are made to the antenna design to further improve its performance. To reduce fabrication errors and improve rigidity, the antenna is newly designed on a dielectric substrate. As discussed in the previous section, the input impedance matching of the antenna is achieved by adjusting the length of the meandered element of the antenna. However, such modification is rather complex, requiring the topology of the antenna to be redesigned and fabricated. Therefore, impedance matching is difficult to achieve through simple tuning of the antenna topology. It has been shown that the length of a slot antenna can significantly be reduced by inserting short-circuited narrow slot-lines along the radiating segment of a slot antenna [79]. The short-circuited narrow slot-lines behave as series inductive elements. Due to the insertion of series inductive elements, the electric current on the ground plane then transverses a longer path. As result the resonant frequency decreases. The meandered short-circuited elements of the miniaturized multi-element monopole antenna are replaced with a similar geometry.

The meandered short-circuited elements are first straightened. Then a pair of $0.5mm$ wide open-circuited microstrip lines are inserted along the straightened elements. The insertion of narrow open-circuited microstrip lines introduces shunt capacitance stubs which have a similar size reduction effect. Thus, the physical lengths of the straightened short-circuited elements are reduced. Impedance matching is obtained by simply adjusting the location ($c_a = 3.5mm$) and lengths ($l_a = 4.2mm$) of the inserted narrow microstrip lines. The right angle edges of the spiral-shaped open-circuited elements are replaced with curved edges. The final lengths of the open-circuited elements l_{open_m} and short-circuited elements l_{short_m} are $144mm$ and $20mm$ respectively. The modified geometry is shown in Figure 5.6.

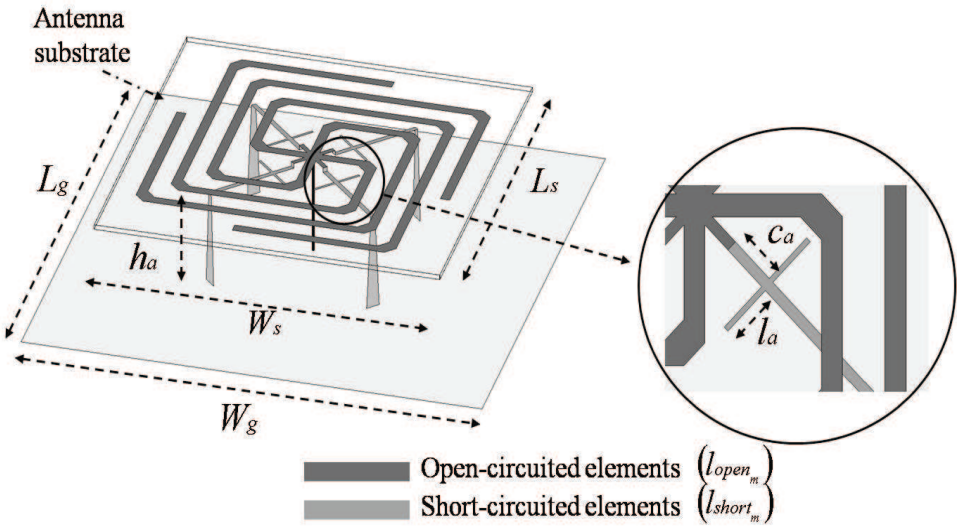

Figure 5.6: Topology of the modified multi-element monopole antenna. The inserted open-circuited microstrip is shown in the right.

5.3.2 Fabrication and Measurement

The modified antenna is simulated and then fabricated using a $W_s \times L_s = 75mm \times 75mm$ Rogers5880 with thickness of $1mm$, dielectric constant of $\varepsilon_a = 2.2$, and loss tangent of $\tan\delta_a = 0.0009$. The two layers of the antenna geometry are etched on the top and bottom side of the dielectric substrate. The two layers are then connected through Via holes.

The short-circuited pins are connected to each end of the four short-circuited elements. The integrated antenna structure is then soldered on to a $W_g \times L_g = 50mm \times 50mm$ ground plane. The antenna is fed from the center using a coaxial feed. The antenna height (h_a) is set to $20mm$. The return loss of the fabricated modified multi-element monopole antenna is presented in Figure 5.7. The antenna displays good impedance matching and 3.5% 2:1 VSWR bandwidth. The far-field co-polarized and cross-polarized radiation patterns of the antennas are presented in Figure 5.8 (a) and Figure 5.9 (a) respectively. The measured pattern indicates the radiation pattern of the antenna remains similar to that of the original miniaturized multi-element monopole antenna after the modification. As expected due to the small ground plane dimension, the modified antenna features relatively high levels of cross-polarization levels. The gain of the modified multi-element monopole antenna is measured to be -3.3 dBi , indicating the new geometry enhances the radiation efficiency of the antenna compared to the original miniaturized multi-element monopole antenna.

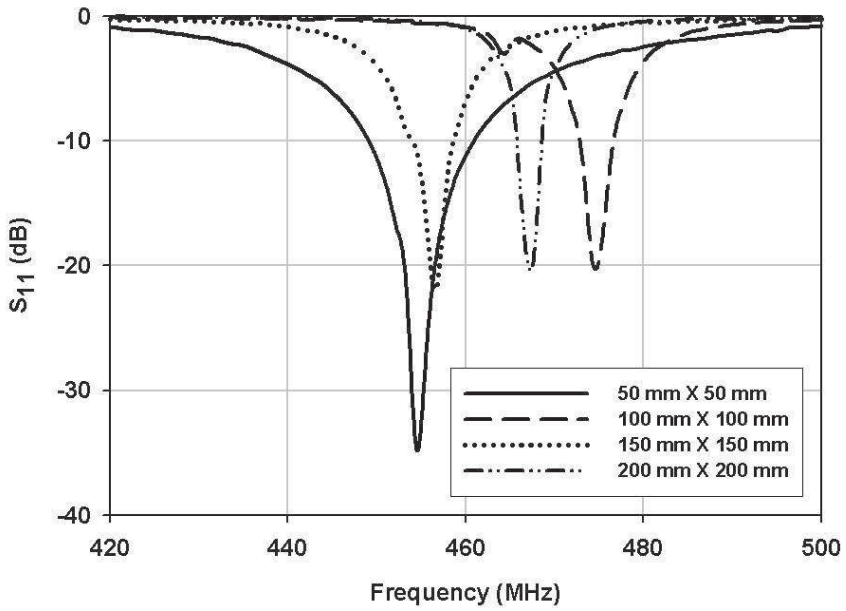

Figure 5.7: Measured S_{11} response of the modified multi-element monopole antenna as a function of ground plane dimension.

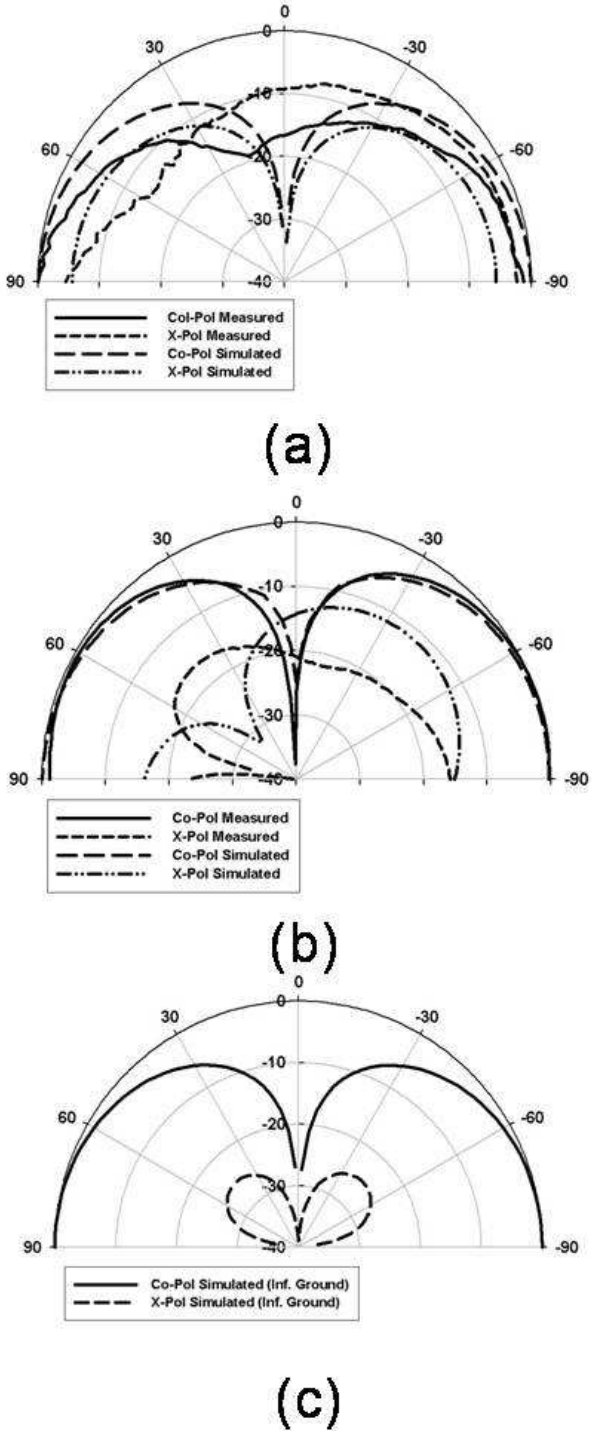

Figure 5.8: Measured and simulated E-Plane radiation pattern of the modified multi-element monopole antenna as a function of ground plane dimension. (a) $W_g \times L_g = 50mm \times 50mm$. (b) $W_g \times L_g = 200mm \times 200mm$. (c) Infinite ground plane

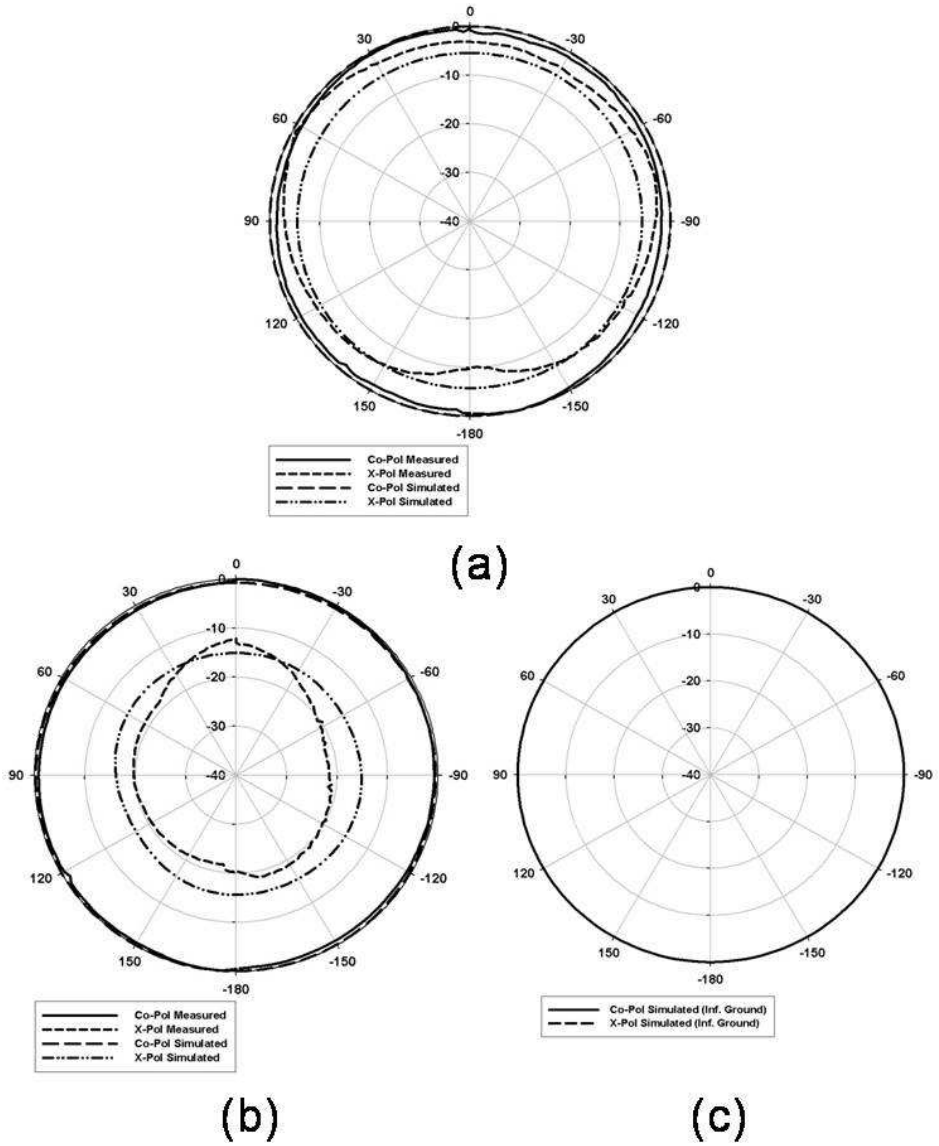

Figure 5.9: Measured and simulated H-Plane radiation pattern of the modified multi-element monopole antenna as a function of ground plane dimension. (a) $W_g \times L_g = 50mm \times 50mm$. (b) $W_g \times L_g = 200mm \times 200mm$. (c) Infinite ground plane.

5.3.3 Parametric Studies

The dimension of the ground plane is increased to examine how the the parameter affects the performance of the modified multi-element monopole antenna. The antenna is subsequently fabricated and measured on four different ground planes with increasing dimension. No additional modifications to the topology of the antenna is performed as the dimension of the ground plane changes. The measured input reflection responses of the antennas are presented in Figure 5.7. It is observed that the antenna remains to be well matched as the size of the ground plane varies. The shift in resonant frequency can mostly be attributed to the radiating ground plane currents which slightly modify the radiation of the antenna. The measured 2:1 VSWR bandwidths, gain, and the calculated directivity of the antennas associated with different ground plane sizes are listed in Table 5.1. The measured and simulated radiation patterns in Figure 5.8 and Figure 5.9 show as the ground plane dimension increases, cross-polarization levels decrease accordingly. As expected the gain increases as a result. It can be seen from Table 5.1 that the gain of the modified multi-element monopole antenna is enhanced by more than 5 dB as the dimension of the ground plane increases to $200mm \times 200mm$.

2:1 VSWR (%)	Measured Gain (dBi)	Directivity (dBi)	$W_g \times L_g$ (mm)
3.5	-3.3	1.0	50×50
1.6	-1.1	1.1	100×100
1.8	0.4	2.0	150×150
0.6	1.6	2.8	200×200

Table 5.1: Measured bandwidth and gain and computed directivity as a function of ground plane dimension. The antenna height (h_a) is $20mm$.

It is important to study the effect of the height of the modified multi-element monopole antenna on its gain and bandwidth. The height of the antenna from the metal ground plane is incremented from $h_a = 10mm$ to $h_a = 30mm$ by adjusting the height of the short-circuited pins. The modified antennas are then fabricated on a $W_g \times L_G = 200mm \times 200mm$ ground plane. Figure 5.10 shows the measured input reflection response of the antennas

with different heights. The measured 2:1 VSWR bandwidth and gain are listed in Table 5.2. The measured results indicates that the height of the antenna can be further reduced to less than $\lambda/25$ without suffering severe gain degradation which is important for low-profile, vertically-polarized antennas.

2:1 VSWR (%)	Measured Gain (dBi)	Antenna height h_a (mm)
0.4	-3.1	10 ($\lambda/40$)
0.5	1.0	15 ($\lambda/27$)
0.6	1.6	20 ($\lambda/20$)
0.5	1.9	30 ($\lambda/13$)

Table 5.2: Measured bandwidth and gain as a function of antenna height. The ground plane dimension is $W_g \times L_g = 200mm \times 200mm$.

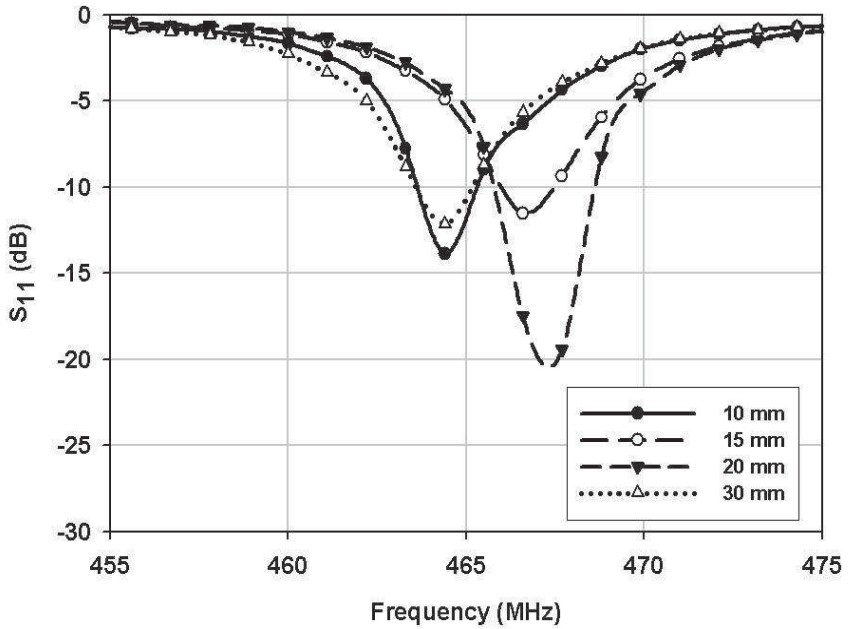

Figure 5.10: Measured S_{11} response of the modified multi-element monopole antenna as a function of antenna height h_a.

5.4 The Dual-Band Multi-Element Monopole Antenna

5.4.1 Antenna Design

It has been shown in the previous section that the gain of the modified multi-element monopole antenna can greatly be enhanced by increasing the size of the ground plane. For small antennas, due to ohmic losses the bandwidth is found to be inversely proportional to the gain. Therefore in this section, additional methods are investigated and discussed to further increase the bandwidth while maintaining the gain of the proposed antenna.

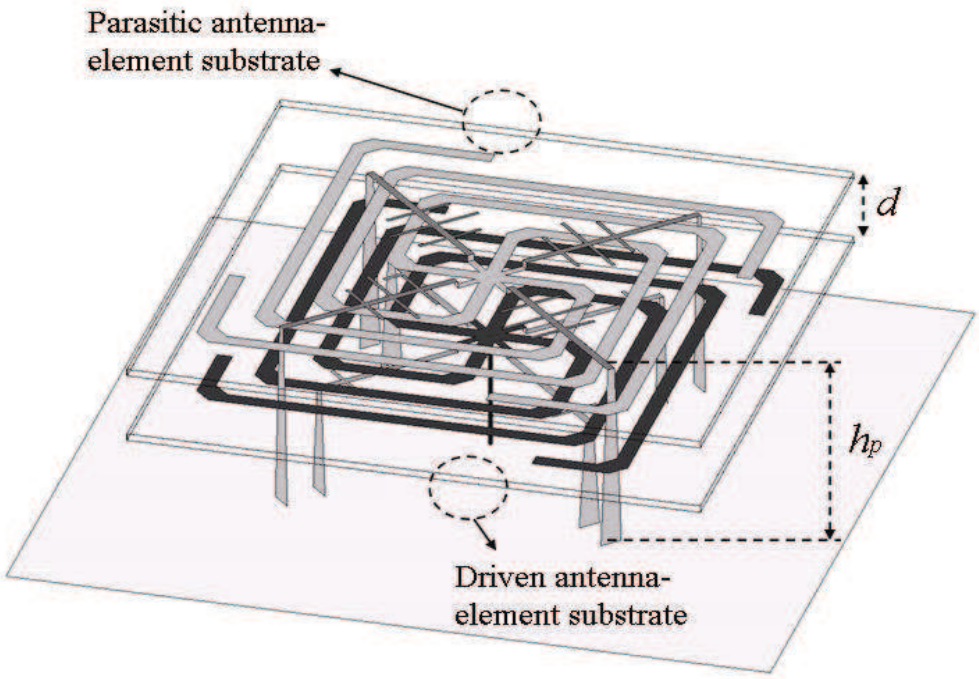

Figure 5.11: Topology of the dual-band multi-element monopole antenna.

The fundamental resonance of the miniaturized multi-element monopole antenna is determined by the overall length of the antenna arms. As mentioned earlier, the length of the each arm of the antenna is designed to be of identical length to ensure an electrical symmetry of the antenna structure. Therefore each arm of the antenna features an identical electromagnetic resonance. Adjusting the length of each arm to be of different lengths is found to be ineffective in achieving multi-resonance behavior. Instead, a single resonance which is

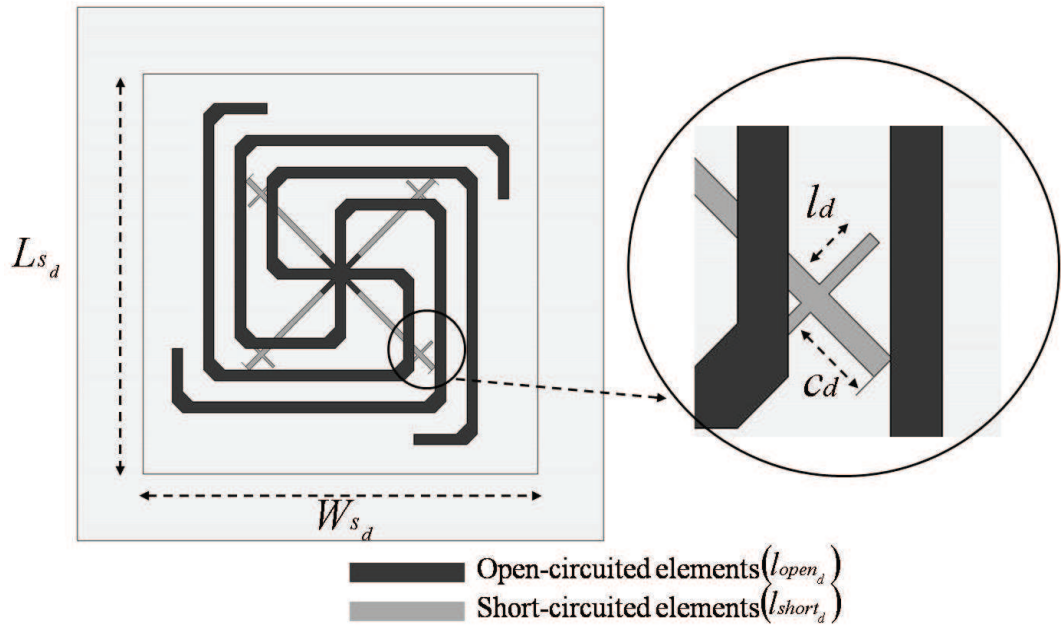

Figure 5.12: Topology of the driven antenna-element of the dual-band multi-element monopole antenna. The inserted open-circuited microstrip is shown in the right.

approximately the average of the combined resonances of each different arms is observed. In addition, transmission zeros limits the multiple resonances from being effectively combined for bandwidth enhancement. Thus, a parasitic coupling approach is used to further improve the bandwidth of the proposed antenna. The dual-band miniaturized multi-element monopole antenna is designed by adding an additional parasitic antenna topology on top of the original modified multi-element monopole antenna structure. Figure 5.11 shows the geometry of the proposed dual-band antenna. The driven and parasitic antenna-elements of the proposed antenna are separated by spacing d, which is adjusted by modifying the vertical heights (h_p) of the short-circuited pins of the parasitic antenna-element. The coaxial feed is connected to the driven antenna-element. The driven and parasitic antenna-elements are presented in Figure 5.12 and Figure 5.13 respectively. For the driven antenna element, the open-circuited element and the short-circuited element is designed to be on the top and bottom side of the driven antenna-element substrate respectively, similar to the original single resonance miniaturized multi-element monopole antenna. However, it should be

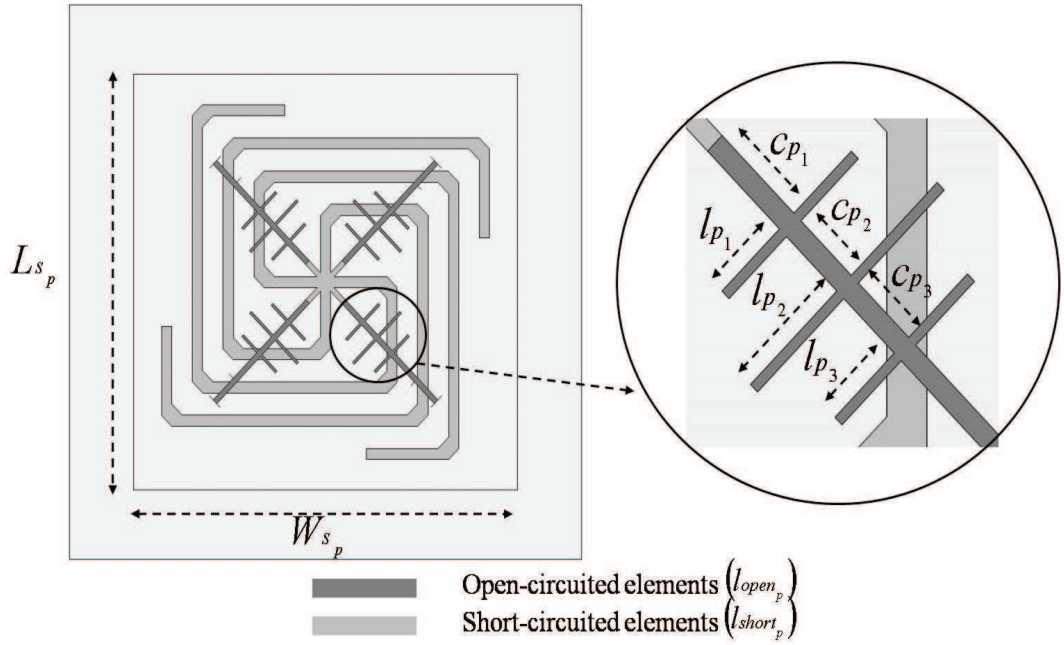

Figure 5.13: Topology of the parasitic antenna-element of the dual-band multi-element monopole antenna. The inserted open-circuited microstrip is shown in the right.

noted that for the parasitic antenna-element, the configuration of the open-circuited element and the short-circuited element is reversed. The open-circuited element for the parasitic antenna-element is placed on the bottom side of the parasitic antenna-element substrate. Such modification is made to ensure the two antenna-elements are electrically coupled at similar locations. By doing so, the electric fields in both antenna-elements will be in phase and therefore the far field radiation is enhanced. Impedance matching is achieved by adjusting the lengths and locations of the inserted $0.5mm$ wide open-circuited microstrip-lines for each respective antenna-elements. The final design parameters of the dual-band multi-element monopole antenna are provided in Table 5.3.

5.4.2 Fabrication and Measurement

The dual-band multi-element monopole antenna follows similar fabrication procedure as its single-resonance predecessor. The antenna is simulated using HFSS. Then, both

l_{open_d}	l_{short_d}	l_d	c_d	W_{s_d}	L_{s_d}	l_{open_p}	l_{short_p}
118	20	2.8	2.5	75	75	126	25.5
l_{p_1}	l_{p_2}	l_{p_3}	c_{p_1}	c_{p_2}	c_{p_3}	W_{s_p}	L_{s_p}
4	6	4.1	3.5	2.5	2.5	75	75

Table 5.3: Design parameters of the dual-band multi-element monopole antenna (*mm*). The ground plane dimension is $W_g \times L_g = 200mm \times 200mm$.

driven and parasitic antenna-elements are etched using identical substrates. The short-circuited pins are then connected to their respective locations. Small holes are drilled through both of the antenna-element substrates for the short-circuited pins of the parasitic antenna-element. A dielectric spacer is placed between the two antenna-element substrates while the short-circuited pins are connected to the substrates. The assembled antenna topology is then connected to a $W_g \times L_g = 200mm \times 200mm$ ground plane. Finally, a coaxial cable is connected to the driven antenna-element. The measured and simulated return losses of the dual-band antenna is presented in Figure 5.14. As can be observed from the the figure, by adjusting d, the two resonances of the antenna can be controlled to split or merge with one another. The far-field co-polarized and cross-polarized radiation patterns of the antenna are presented in Figure 5.15. It can be observed that the radiation pattern remains similar to a traditional monopole antenna throughout the operating frequency band. In addition, the added parasitic antenna-element does not appear to cause increased levels of cross-polarized radiations. The measured 2:1 VSWR bandwidth and gain of the dual-band multi-element antenna with different spacing d are presented in Table 5.4.

	Resonant Frequency (MHz)	2:1 VSWR (%)	Measured Gain (dBi)	Antenna height h_p (*mm*)	d (*mm*)
$Dual-$	453	0.6	2.0	28	7
band	465	0.7	2.2	28	7
$Wide-band$	460	2.2	2.0	31	10

Table 5.4: Measured bandwidth and gain as a function of spacing d.

Compared to the original multi-element monopole antenna with identical ground plane

dimension, the dual-band multi-element monopole antenna features enhanced bandwidth without gain degradation. By controlling the spacing d, the wide-band response is measured to have more than twice the 2:1 VSWR bandwidth of the individual bands of the dual-band response. The addition of a parasitic antenna-elements results in increasing the overall height of the antenna by 50%. However, it has been shown that the height can be further reduced without significant performance trade-off.

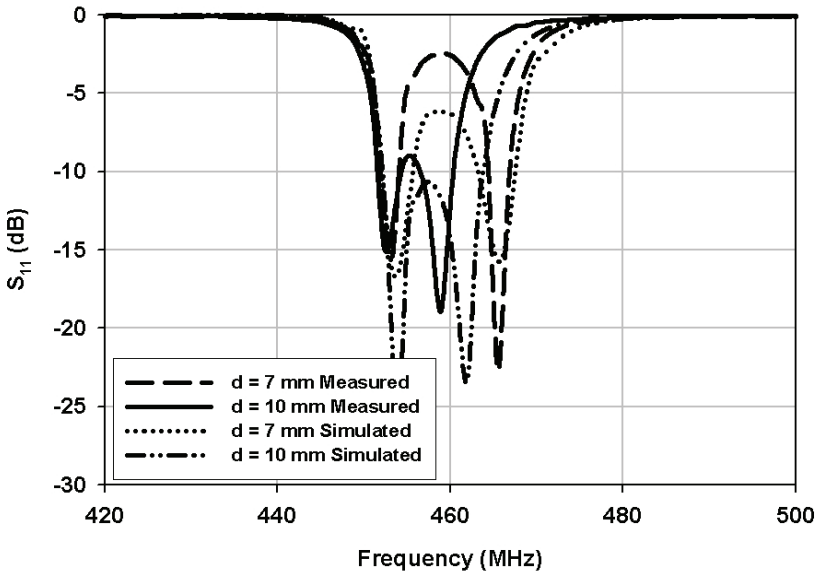

Figure 5.14: Measured and simulated S_{11} response of the dual-band multi-element monopole antenna as a function of spacing d.

5.5 Summary

An antenna miniaturization method for wire type antenna is proposed and discussed. Using this method, an electrically small antenna is designed, emulated, and measured. The featured multi-element monopole antenna displays similar radiation behavior as that of a traditional vertical monopole antenna while having a vertical profile as low as $\lambda/40$. The lateral dimension of the multi-element monopole antenna is significantly reduced by

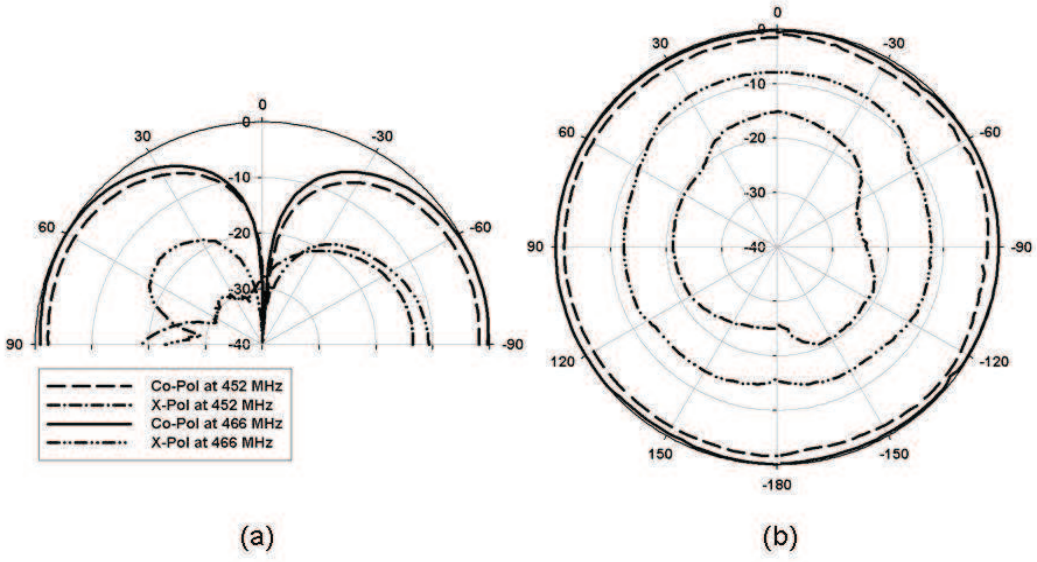

Figure 5.15: Measured radiation pattern of the dual-band multi-element monopole antenna. (a) E-Plane. (b) H-Plane. (d = 10mm)

folding the open-circuited elements in a spiral-shaped geometry. Parametric studies are performed to investigate further antenna miniaturization and performance improvements. The measured multi-element monopole antenna displays omnidirectional pattern in the horizontal plane of the antenna and low levels of cross-polarized radiations. In addition, the proposed antenna is modified to feature enhanced bandwidth and excellent gain.

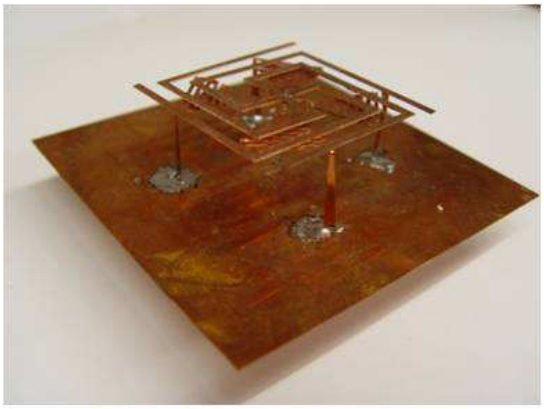

(a)

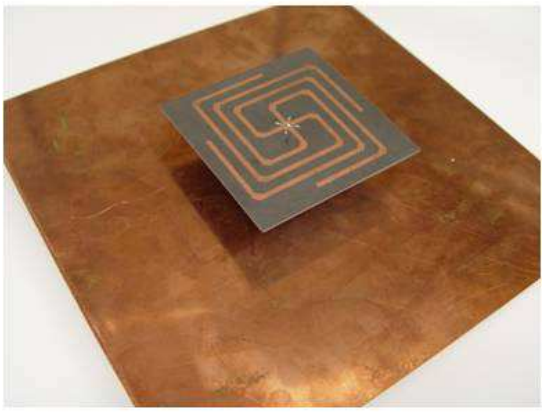

(b)

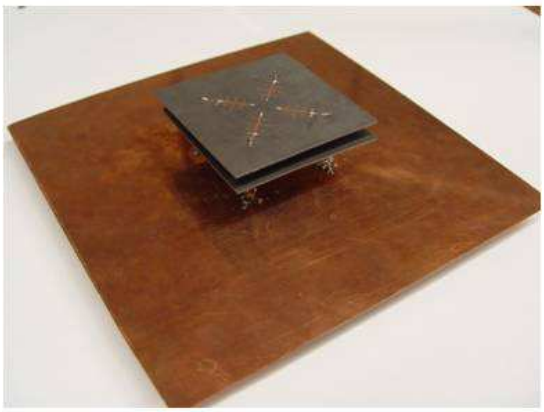

(c)

Figure 5.16: Photograph of the fabricated antennas. (a) Miniaturized multi-element monopole antenna. (b) Modified multi-element monopole antenna. (c) Dual-band/Wide-band multi-element monopole antenna.

CHAPTER 6

Applications of the Multi-element Monopole Antenna

6.1 Introduction

The concept, functionality and analysis of the Multi-element Monopole Antenna (MMA) have been introduced and discussed in the previous chapter. In this chapter, the performance of the MMA is demonstrated in two separate application scenarios.

6.1.1 Design Guidelines for the MMA at 2.45 GHz

In platform-level integration scenarios, the Multi-element Monopole Antenna (MMA) is adapted to function at 2.45 GHz. The MMA is redesigned to be monolithic - the entire structure is contained in a RO5880 dielectric substrate. The overall topology of the antenna is further simplified. These modifications of the original design greatly enhance the rigidity and compactness and reduce the number of fabrication procedures and time. The redesigned topology of the MMA is shown in Figure 6.1. It can be observed that the antenna height (h) is now equivalent to the substrate thickness. Likewise, the square ground plane dimension (L) is equivalent to the substrate dimension. The details of the redesigned monolithic MMA are addressed in Section 6.2 and Section 6.3.

Since the behavior of the MMA is equivalent to that of a conventional monopole, the

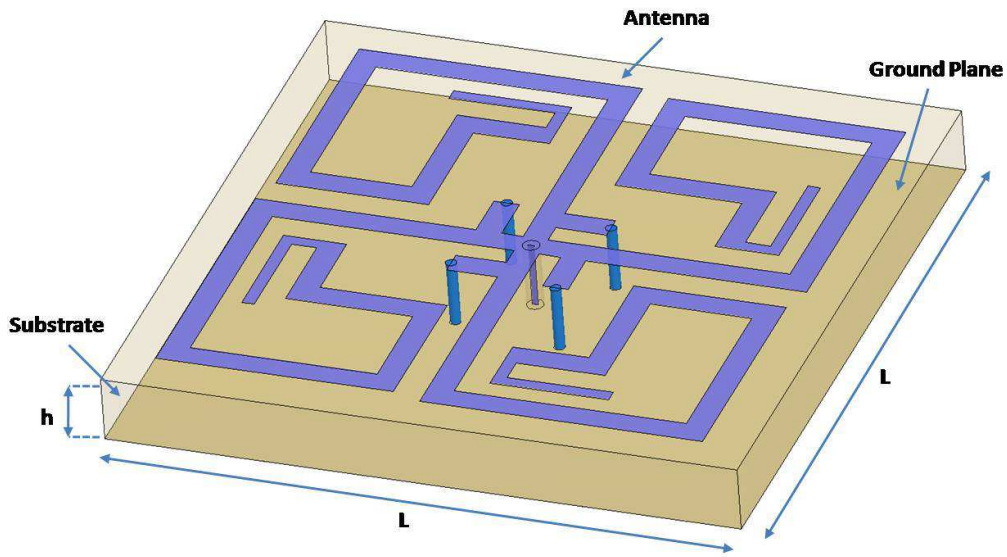

Figure 6.1: The monolithic MMA using dielectric substrate.

performance of the antenna is dictated by its volumetric dimension. Parametric studies presented in Chapter 5 reinforce and quantify this relation. Therefore it is important to investigate and characterize the performance versus physical dimension for the monolithic MMA. Parametric studies can be utilized as design guidelines when incorporating the monolithic MMA for specific wireless link budgets at 2.45 GHz.

Gain and cross polarization levels of an antenna are key parameters for efficient signal transmission and reception. The effect of the antenna height (h) and ground plane dimension (L) on the gain and cross polarization levels are studied using full-wave simulations. Figure 6.2 depicts the effect of the antenna height on gain for varying ground plane dimensions. Similar to the measured results in Chapter 5, it can be observed that as the antenna height further increases, gain begins to converge to saturation. Here, the Figure of Merit (FoM) is defined as maximal gain improvement for minimal increased antenna height. FoM indicates it is recommended to first use slightly greater than minimum antenna height and make incremental increase to suffice for the wireless link budget. It is interesting to note that as the ground plane dimension increases by a factor of 3, the overall computed gain actually decreases by a small margin. This is clearly different from the measured relation

in Chapter 5. To further investigate this trend, the effect of the ground plane dimension on gain for varying antenna heights is studied and presented in Figuure 6.3. The computed gain as a function of ground plane dimension support the observation in Figure 6.2 - when the ground plane is electrically small in dimension, incremental increase of the ground plane is ineffective to gain improvement. The discrepancy between the studies in Figure 6.3 and the measured ground plane dimension versus gain relation in Chapter 5 is attributed to the presence of the feed network cable. For electrically small ground planes, the effect of the feed network cable on the antenna performance is significant. High levels of currents are induced on the feed network cable which reradiate into the far field adversely affecting gain, cross polarization and co-polarization. As the ground plane dimension increases, the contributions of the feed network cable in the far field radiation region decrease. However, this is oftentimes extremely difficult to quantify using full-wave simulations. In addition, for platform-integrated application scenarios, the monolithic MMA does not require feed network cables that are used during measurements in the anechoic chamber (open-space). Therefore, the feed network cable is omitted for full-wave simulations and a localized excitation port within the monolithic MMA is modeled instead.

The average cross polarization difference with respect to co-polarization as a function of ground plane dimension and antenna height is computed in Figure 6.4 and Figure 6.5 respectively. Figure 6.4 indicates cross polarization levels decreases considerably when the electrical small ground plane dimension increases. However, as shown in Figure 6.3, this does not translate to improved gain. Similarly, although gain is found to be proportional to antenna height in Figure 6.2, there is no distinct change in cross polarization levels as the antenna height increases in Figure 6.5. These parametric studies indicate that the electrically small ground plane significantly contributes to the far field radiation in conjunction with edge diffration and its contribution levels decline when the ground plane dimension increase as currents become increasingly localized in the antenna. However, the contribution of the ground plane in the far field radiation region has minimum effect on the gain

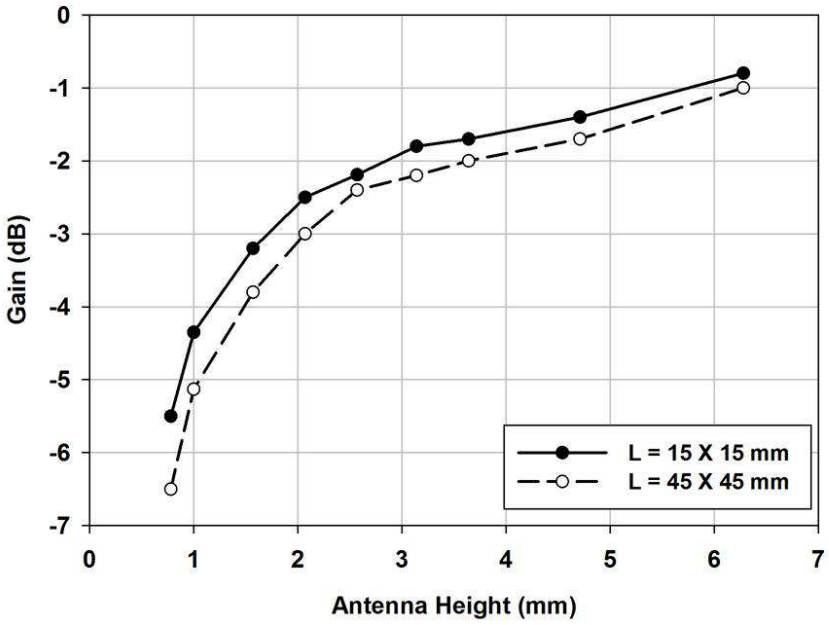

Figure 6.2: The computed gain as a function of antenna height for varying ground plane dimensions.

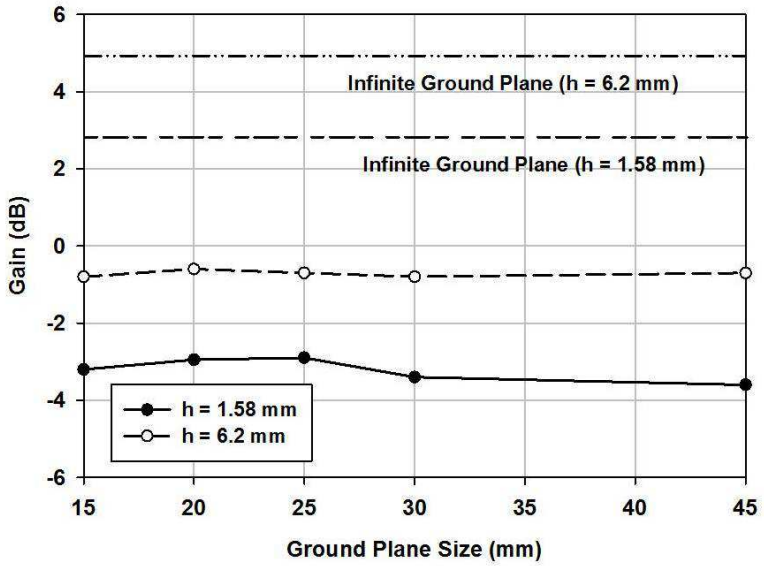

Figure 6.3: The computed gain as a function of square ground plane dimension for varying antenna heights.

of the antenna since the ground plane radiates in a different polarization. Nevertheless, for situations where the monolithic MMA is integrated into an electrically large conductive platform, significant performance enhancement can be expected. For non-conductive, lossy platforms such as FR4 or ceramic, full-wave simulations predict very little effect on the overall performance of the monolithic MMA.

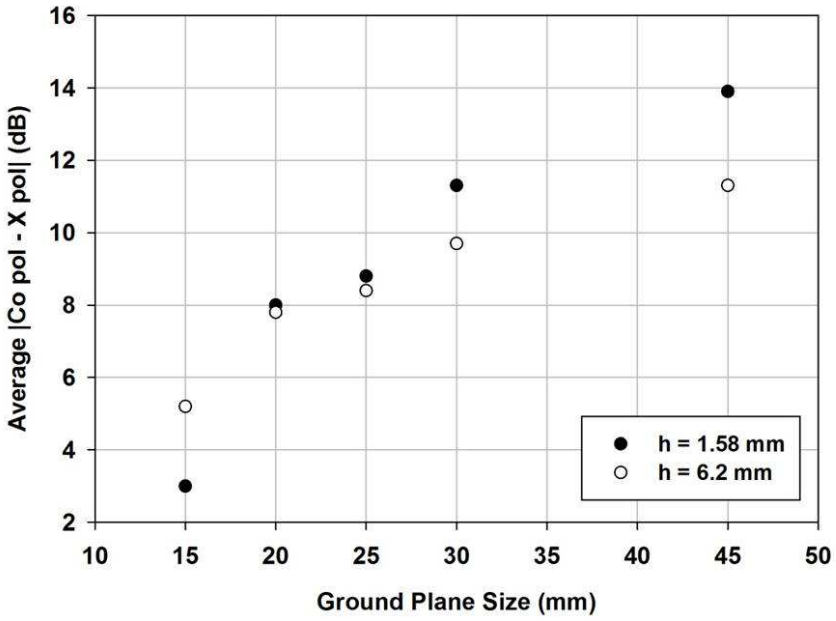

Figure 6.4: The computed average | Co-pol - Cross-pol | as a function of square ground plane dimension for varying antenna heights.

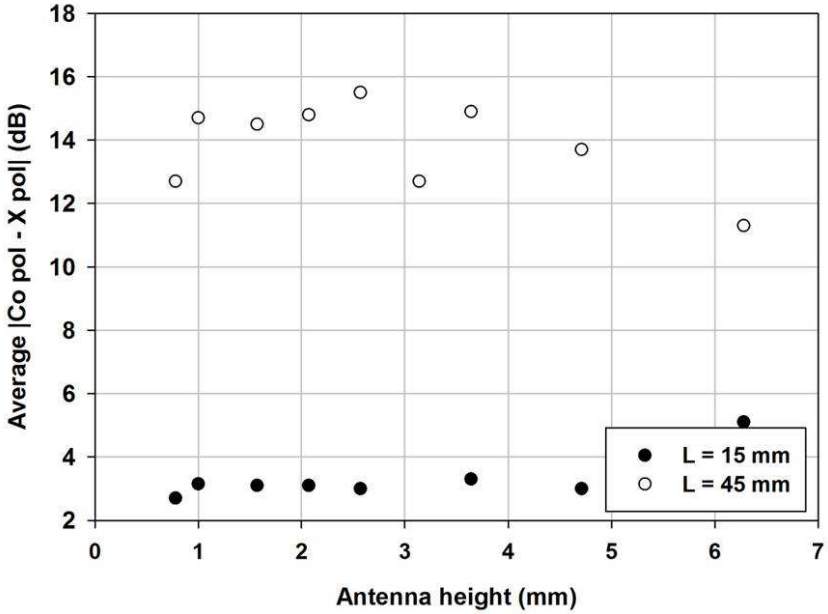

Figure 6.5: The computed average | Co-pol - Cross-pol | as a function of antenna height for varying ground plane dimensions.

6.2 The Small Radio Repeater

6.2.1 Overview of the Small Radio Repeater

Radio repeaters are advantageous for capacity and coverage improvements in situations such as blind spots, obstructive scenarios (i.e. indoor, underground, cell edges etc). Compared to conventional base stations, radio repeaters are generally composed of simpler architecture, and require lower cost and power consumption. Radio repeaters are extensively used in a variety of application scenarios. Numerous studies regarding usage of radio repeaters for cellular applications have been presented [80, 81, 82, 83, 84, 85]. In [81], the performance of an RF radio repeater for Wideband-CDMA (WCDMA) High Speed Downlink Packet Access (HSDPA) is evaluated for in-door communication scenarios. In [84] the antenna isolation requirements are studies for radio repeaters for 3G cellular service. In addition, radio repeaters have been actively employed in non-cellular mobile phone services. In [86], a radio repeater devised using amplifiers and leaky transmission lines for subways

and mines is discussed. An Ultra-wideband (UWB) radio repeater is developed to increase the coverage area in [87]. Pulse-position-modulation (PPM) is used to avoid coupling interface between the received and retransmitted signal. Diversity gain is improved using radio repeaters for Wireless Personal Area Network (WPAN) and presented in [88]. In [89] the design and performance requirements of a radio repeater for satellite digital broadcast systems is discussed. The aforementioned repeaters are designed using conventional $\lambda/4$ antennas as the donor and server antenna. While the exact circuitry is intrinsically linked to the system requirement for each specific application scenario, it should be noted that the dimension of the antennas for these repeaters are relatively large, which may potentially become a critical matter in certain situations. Therefore it would be interesting to incorporate an electrically small antenna into a radio repeater to attain a more compact and integrated topology.

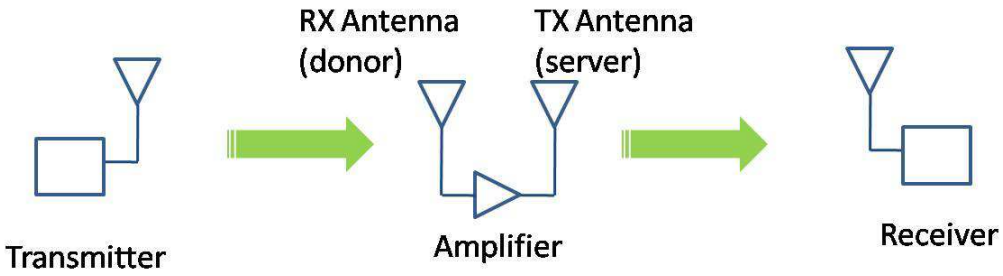

Figure 6.6: The concept of the Small radio repeater.

In this section, the Multi-element Monopole Antenna (MMA) is redesigned to be incorporated into a Small radio repeater. A rudimentary configuration of the Small radio repeater is presented in Figure 6.6. The idea of the Small radio repeater is to achieve enhanced connectivity without the need for increasing the transmit power. The Small radio repeater is envisioned to be placed near shadow boundaries (building corner, entrance to caves or basements, etc.) to receive the line-of-sight signal from the transmitter, amplify and re-transmit and establish a secondary line-of-sight to the receiver. A series of Small radio repeaters are capable of relaying information in stringent wireless propagation en-

vironments by forming a connected a link of line-of-sight nodes. The first version of the repeater is designed to be rigid, small (2 $cm \times 4\ cm$) in physical dimension and capable of being powered by a conventional lithium watch battery for up to 24 hours of continuous operation time. The circuit is composed of low-cost Printed-circuit board (PCB) and mass produced commercial components. The design guidelines based on the performance requirements of the Small radio repeater is summarized in Table 6.1.

Performance Requirements	Design Guidelines
Dimension: 20 $mm \times 40\ mm$	Electrically small planar antenna
Robust packaging	Monolithic repeater circuitry
Minimum power consumption	Homodyne radio architecture
Required communication range (R) R $\geq$ 20 m	Sufficient antenna efficiency Vertical polarization

Table 6.1: Design guidelines of the Small radio repeater.

6.2.2 The Small Radio Repeater Antenna

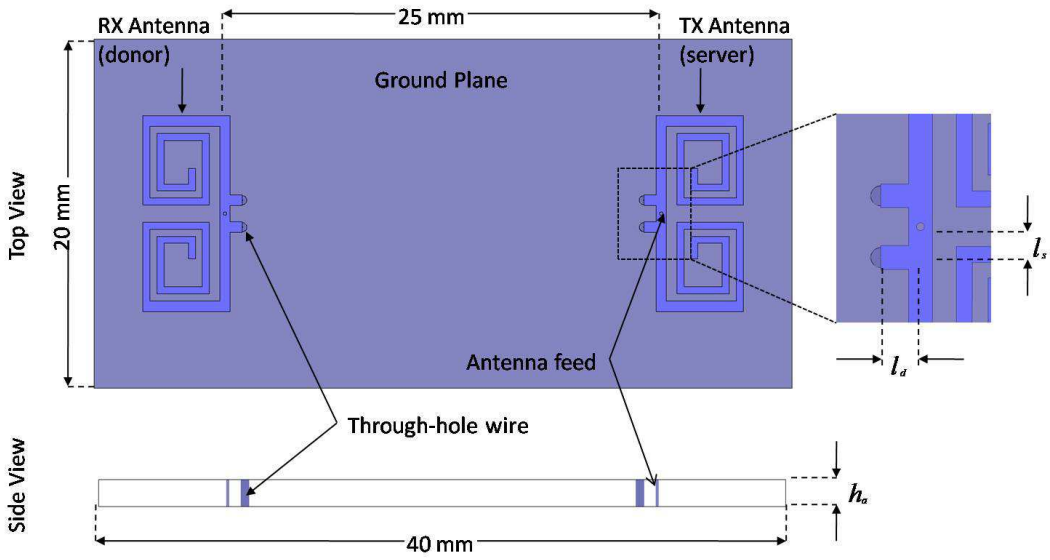

Figure 6.7: The topology of the Small radio repeater antenna.

The Small radio repeater has the simplest active radio architecture and thus can be made very small with minimal power requirement. The most significant challenge for the

proposed small repeater from the antenna prospect is the design of a highly miniaturized planar antenna that can radiate vertical polarization. The topology of the Multi-element Monopole Antenna (MMA) is redesigned for the Small radio repeater to function near 2.45 GHz. Two identical antennas are designed to function as the donor (TX antenna) and server (RX antenna) respectively. First, the original MMA presented and discussed in Chapter 5 is simplified into a two-layer topology. Similar to the original MMA design, a small resonant structure is formed by a quarter-wavelength transmission line short-circuited at one end using through-hole wires and open-circuited at the other end. Space compression of the Small radio repeater antenna is accomplished by folding the quarter-wavelength segment in a spiral-shaped geometry. It has been noted in Chapter 5 that in order for a quarter-wavelength planar antenna to radiate vertical polarization, the antenna topology must be symmetric in the horizontal plane. The addition of quarter-wavelength segments introduces cancelation of horizontal electric currents flowing on the horizontal plane of the antenna. Series of parametric studies regarding the effects of physical parameters of the four-segment-MMA on the antenna gain and bandwidth have been reported in the previous chapter. The design parameters of the newly designed antenna for the Small radio repeater are determined based the parametric studies along with the overall link budget of the system. It is concluded that the lateral dimension of the each antenna must be greater than $15\ mm \times 15\ mm$ to meet the performance requirements. However, this becomes problematic given the overall lateral dimension of the Small radio repeater. Therefore the Small radio repeater antenna is designed into a two-segment-MMA to minimize antenna dimension with minimal antenna gain degradation. As a consequence of the modified antenna topology, the horizontal radiation pattern of each antenna is expected to be affected. However by placing the each antenna symmetrically on the horizontal plane, cancellation of the horizontal electric current is achieved. Impedance matching of the antenna is facilitated by adjusting the locations (l_s, l_d) of the short-circuited through-hole wires. The physical parameters of the antenna is optimized using Ansoft HFSS and l_s and l_d are chosen to be

0.78 *mm* and 1.0 *mm* respectively. The finalized design of the Small radio repeater antenna is shown in Figure 6.7.

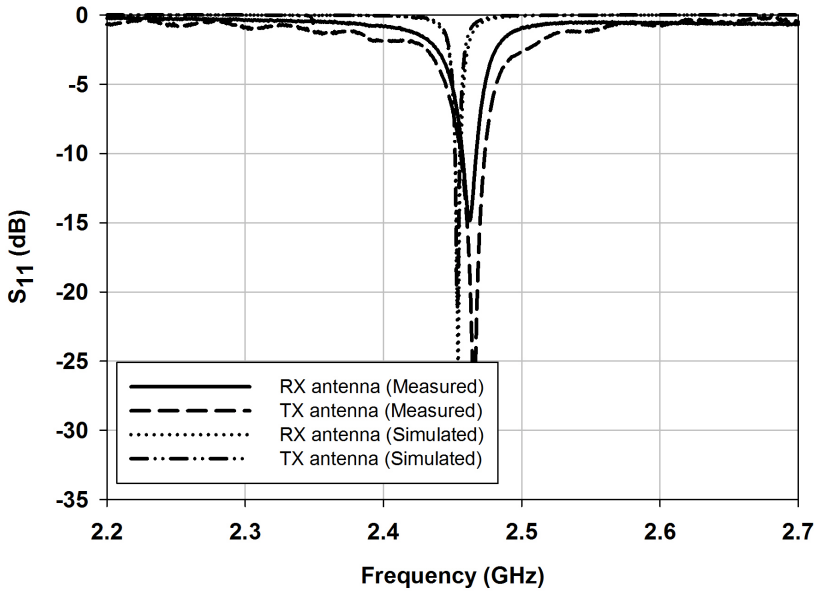

Figure 6.8: The measured and simulated input reflection coefficients of the Small radio repeater antenna.

The antenna design and ground plane are printed on the top and bottom layer of a 1.58 *mm* thick (h_a) Rogers5880 with dielectric constant of $\varepsilon_a = 2.2$, and loss tangent of $\tan\delta_a = 0.0009$ respectively. Through-holes are drilled to construct the antenna feeds and the short-circuited wires. The input measured and simulated input reflection coefficients of the antenna are presented in Figure 6.8. It is observed that the simulation and measurement results agree with less than 0.8% discrepancy. The far-field radiation patterns are measured in the anechoic chamber of the University of Michigan using a one-port signal generator. The orientation of the measured antenna is shown in Figure 6.9. Co- and cross-polarized patterns of the antenna are presented in Figure 6.10. Distortion of the radiation patterns can be observed in the x-y and z-x plane due to the asymmetry of the antenna topology in the respective planes. It should be noted that the measured patterns in Figure 6.10 depict the patterns when only antenna element (TX antenna or RX antenna) is excited. Therefore the

pattern distortion will be significantly alleviated during the actual operation of the Small radio repeater antenna when both of the antennas are simultaneously excited and the horizontal currents are effectively canceled. The relatively high levels of cross polarization is expected as the ground plane of the antenna is less than $\lambda/3 \times \lambda/6$ in electrical dimension, which causes significant reradiation of the feed network cable connected to the antenna for measurement purposes. The actual cross polarization levels of the Small radio repeater are expected to be much lower during field operation as studied in Section 6.1. The maximum gain in the x-y plane is measured to be -3.7 dBi, similar to the requirement based on the link budget.

6.2.3 Integration and Measurement of the Small Radio Repeater

The channel isolator circuit is an array of a single pole parallel LC unit cell. The LC unit cell consists of a square inductance and interdigital capacitance that is optimized using full wave simulations to resonant at the operating frequency of the antennas. The resonant single pole LC network suppresses the wave propagation from one antenna to the other, thus behaving as an effective channel isolator. The designed Small radio repeater antenna is integrated with the TX/RX channel isolator circuit. Minimum levels of changes of the resonance of the Small radio repeater antenna combined with the channel isolator are measured. The far-field radiation patterns of the Small radio repeater system is measured in an identical procedure as described in Subsection 6.2.2 and the results are shown in Figure 6.11. Due to the effect of the channel isolator, a front-to-back ratio (FTBR), in respect the the +x ($\phi = 0^\circ$) and -x direction ($\phi = -180^\circ$) of more than 8 dB is observed in the measured x-y plane. Overall, directivity increases in the x-y plane, which can potentially be advantageous for electrically small antennas of this nature. Reduced levels of pattern distortion is measured both y-z and z-x planes. The maximum gain in the x-y plane is measured to be -3.5 dBi, similar to the measured gain of the circuit without the channel isolator. The fabricated Small radio repeater is shown in Figure 6.12.

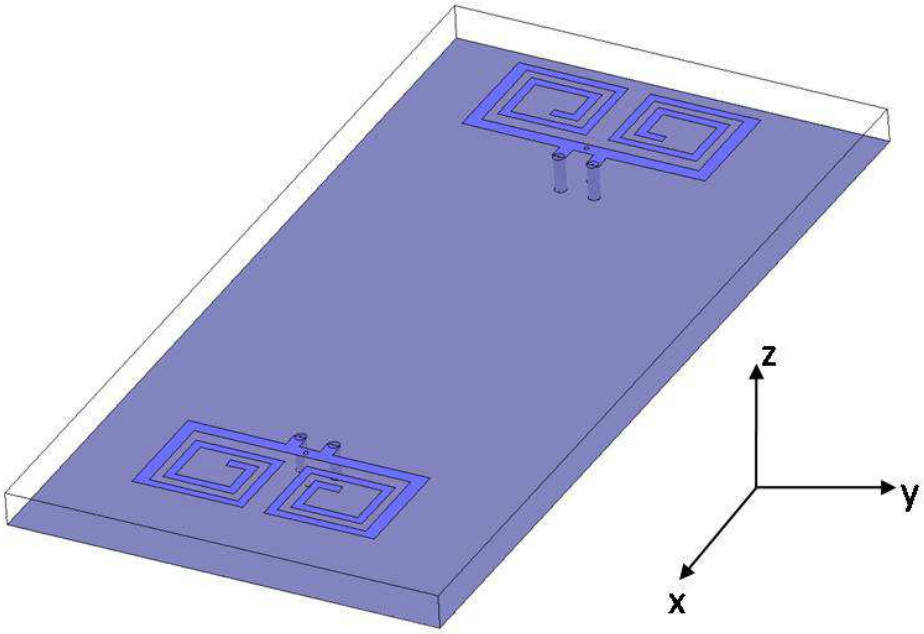

Figure 6.9: The far-field measurement setup of the Small radio repeater antenna.

6.3 A Fully Integrated Transmitter Module

6.3.1 Integrated Transmitter Antenna

Extensive research and development regarding integrated radio transceivers circuities [90, 91, 92, 93, 94, 95, 96, 97] have been conducted up to present. A consensus suggesting the integration of an electrically small antenna being the next milestone has been starting to form. Astonishing amount of effort has been made in recent years to integrate a compact antenna with the RF transceiver circuitry [98, 99, 100, 101, 102, 103, 104, 105, 106, 45, 107, 108]. Thus, antenna miniaturization becomes of even greater importance.

In this section, the Multi-element Monopole Antenna (MMA) is fully integrated into an RF front-end transmitter module for in-door image transmission. The RF front-end transmitter module is to be combined with a commercially-built component consisting of a CMOS image processor (camera) and microprocessor unit. The purpose of the RF front-end transmitter module is to effectively transmit the image signal with 2 MHz bandwidth to a commercially-built base station unit connected to a personal computer. The advantages

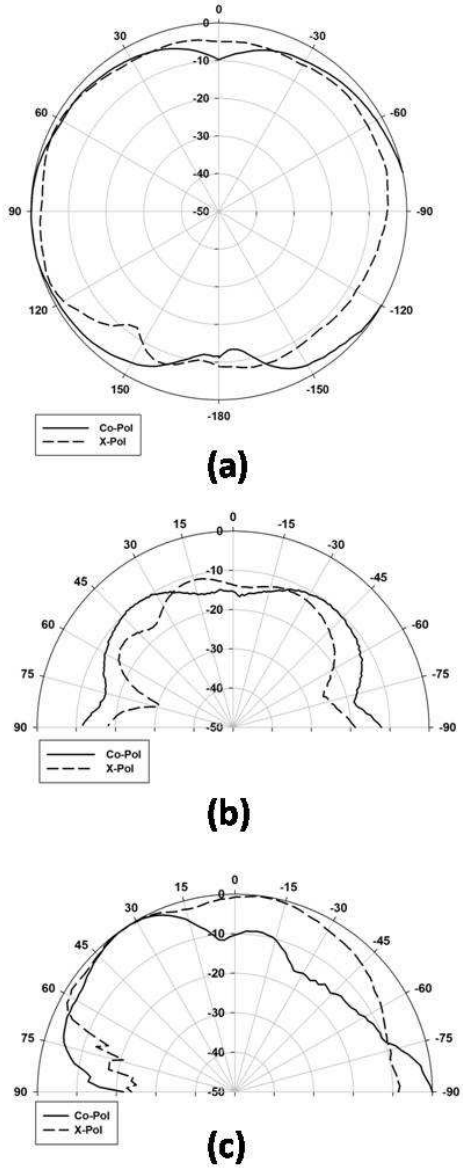

Figure 6.10: The measured far-field radiation patterns of the Small radio repeater antenna. (a) x-y plane. (b) y-z plane. (c) z-x plane.

of vertical polarization for near-ground communication has been discussed in Chapter 4. Consequently for optimum performance, on-board conventional antennas shown in Figure 6.13 are typically oriented vertically on the wireless platform. The low-profile MMA is advantageous in designing an integrated, planar-type RF front-end transmitter as depicted in Figure 6.14.

The four-arm MMA topology introduced in Chapter 5 is redesigned into a two-layer

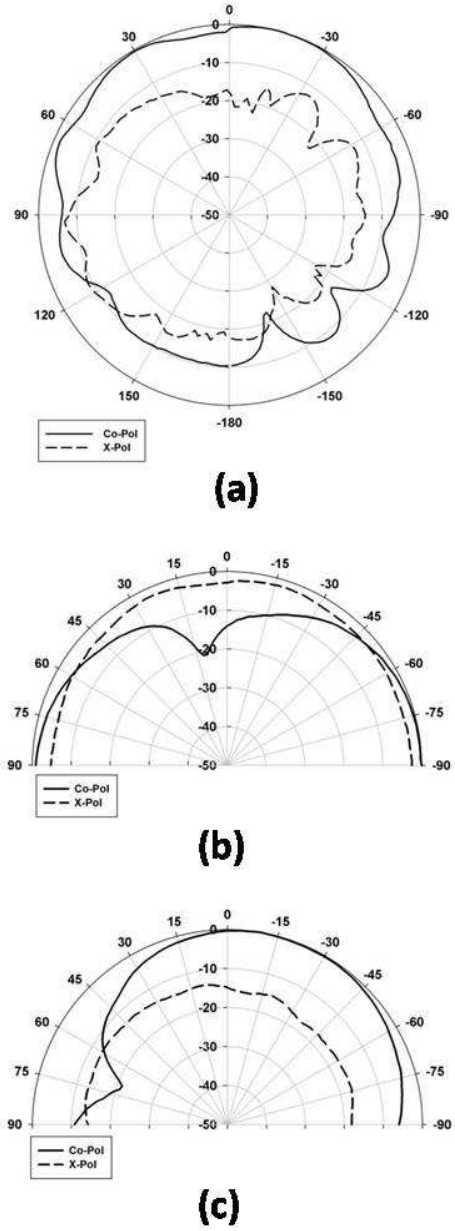

Figure 6.11: The measured far-field radiation patterns of the Small radio repeater antenna integrated with the channel isolator. (a) x-y plane. (b) y-z plane. (c) z-x plane.

topology operating at 2.45 GHz. The two layer antenna topology is then vertically stacked on a two-layer RF front-end transmitter circuitry, forming a four-layer Integrated transmitter module as shown in Figure 6.15. The electrical connection between the antenna and the RF front-end transmitter circuitry is established using Plated Vias. Clearances are created around the RF and DC ground plane to prevent short-circuiting the antenna feed connected

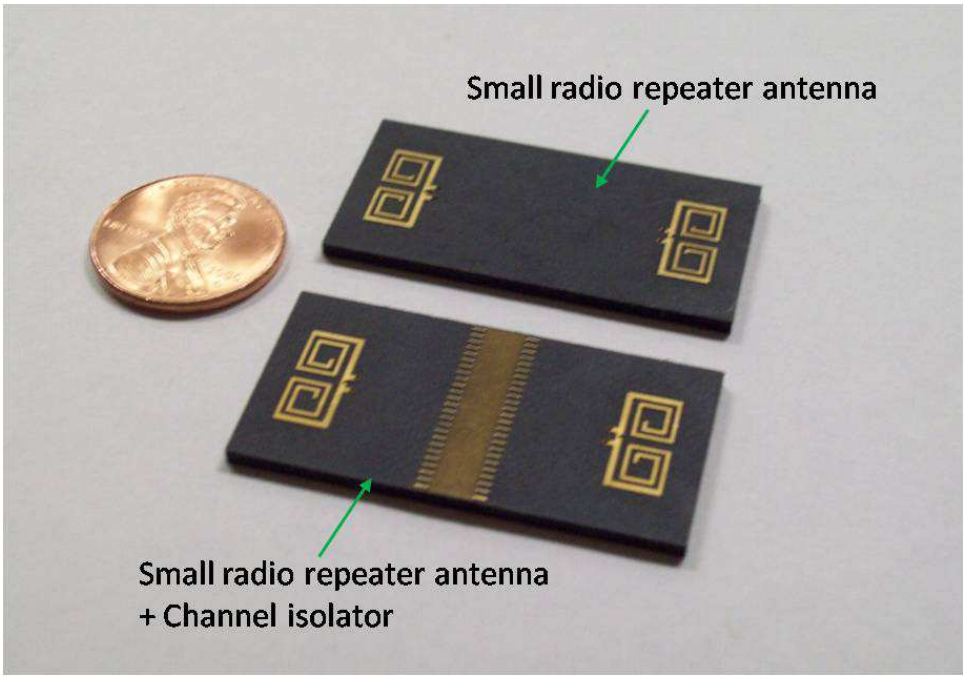

Figure 6.12: The fabricated Small radio repeater antenna.

to the nRF2401A Transceiver chip by Nordic Semiconductor. Installation of Blind Vias are difficult and costly for conventional Printed circuited board (PCB) fabrication technology. Consequently, the antenna design in Layer 1 is shifted to avoid direct contact with the Plated Vias that connects the RF and DC ground plane as shown in Figure 6.16. This results in an increased lateral dimension of the Integrated transmitter module. However, the fabrication procedure is kept simple and low-cost. The physical parameters of the antenna is optimized through full wave simulations of the Integrated transmitter module. The finalized antenna design is shown in Figure 6.17. The input impedance matching is achieved when l_p and l_q are 1.6 *mm* and 1.1 *mm* respectively.

6.3.2 Fabrication and Measurement of the Integrated Transmitter Antenna

The Integrated transmitter module antenna topology and the RF ground plane are printed on the top and bottom layer of a 1.58 *mm* thick (h_b) Rogers5880 with dielectric constant

of $\varepsilon_b = 2.2$, and loss tangent of $\tan\delta_b = 0.0009$ respectively. The RF-front end circuitry and the DC ground plane are printed on two sides of a 0.5 *mm* thick FR4 substrate with dielectric constant of $\varepsilon_c = 4.4$, and loss tangent of $\tan\delta_c = 0.02$ respectively. The fabricated Integrated transmitter module can be seen in Figure 6.18. To verify the performance of the designed antenna, the antenna is fabricated on a Rogers5880 substrate with identical properties and the input reflection coefficient and far-field radiation patterns are measured. The measured input reflection coefficient in Figure 6.19 indicates good agreement with the simulation result. Therefore, comparable levels of accuracy can be expected for the Integrated transmitter module. The measured radiation patterns of the antenna are presented in Figure 6.20. The antenna is observed to feature an omnidirectional pattern in the H-Plane. The relatively high levels cross polarizations can be attributed to the small lateral antenna dimension of less than $\lambda/8 \times \lambda/8$. The cross polarization levels is expected to decrease for the Integrated transmitter module once the feed network cable is removed as discussed in Section 6.1. The gain is measured using a standard double-ridged horn antenna. The maximum gain in the H-plane is measured to be -3.4 dBi. Photograph of the Integrated transmitter module combined with commercially-built CMOS image sensor and microprocessor units is presented in Figure 6.21. The image transmitted from the Integrated transmitter module is shown in Figure 6.22.

6.4 Summary

In this chapter, the performance and advantages of the Multi-element Monopole Antenna (MMA) is demonstrated in two separate application scenarios. The MMA is redesigned to be monolithic and to scaled to operate at 2.45GHz. Parametric studies are performed to establish design guidelines for maximum performance with minimum antenna dimension. The redesigned MMA for both applications are a fraction of wavelength in physical dimension and exhibits sufficient performances for the predetermined wireless

link budgets. It should be noted that the technical benefits of using the MMA is maximized as the frequency of operation decreases beyond the vicinity of UH, VH frequency bands. This is due to that fact that the advantages of vertical polarization generally tends be more definitive as the operating frequency decreases.

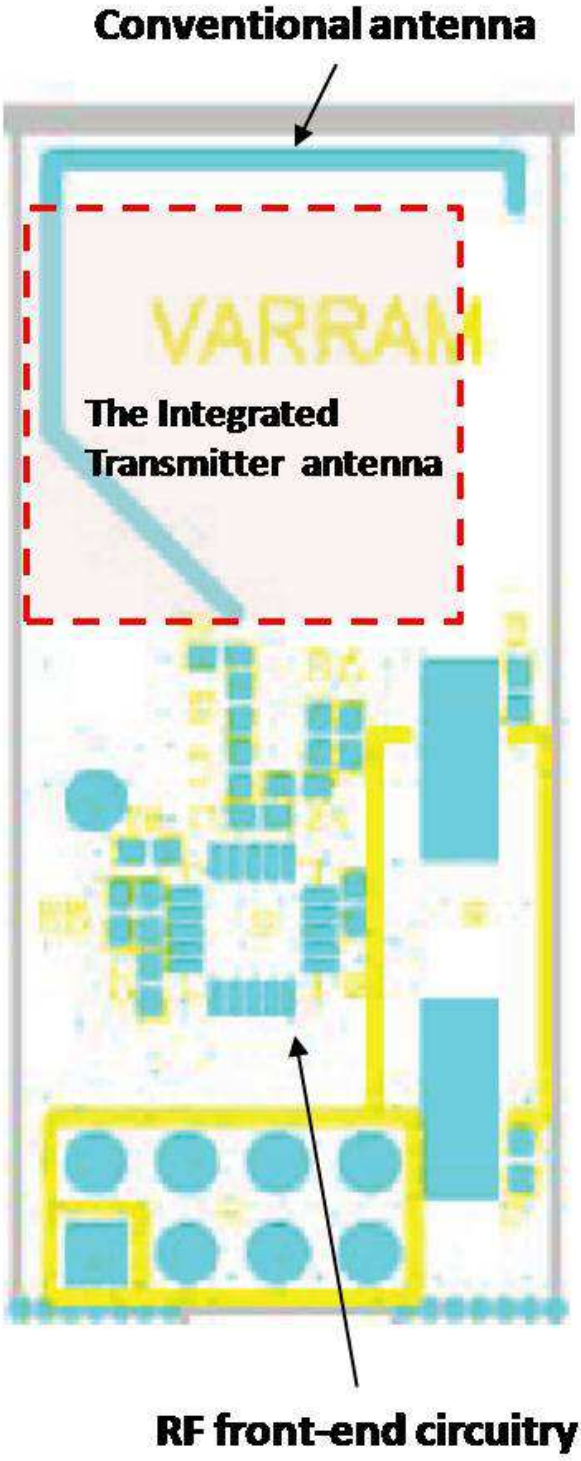

Figure 6.13: Conventional RF-front end transmitter with on-board antenna.

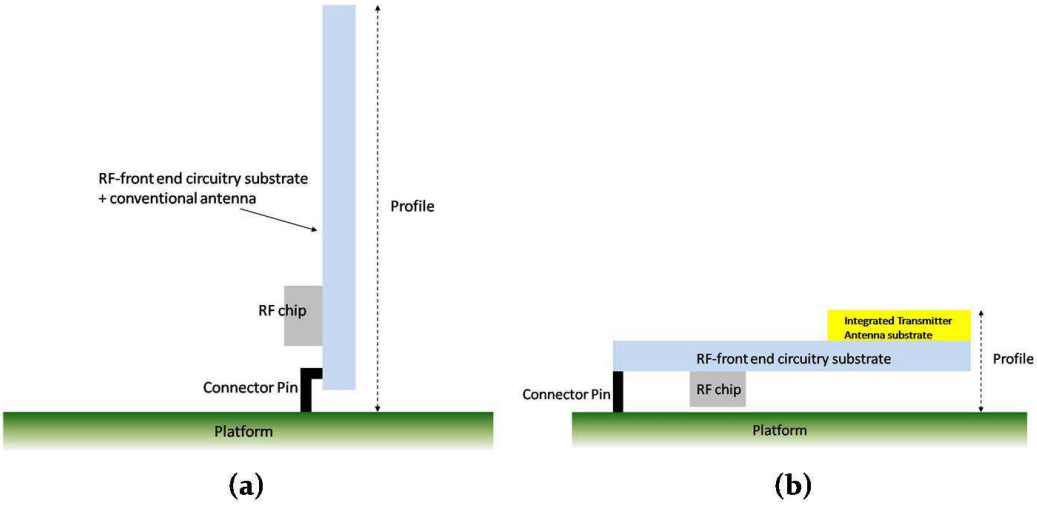

Figure 6.14: Comparison of (a) conventional RF front-end transmitter with on-board antenna and the proposed (b) Integrated transmitter module.

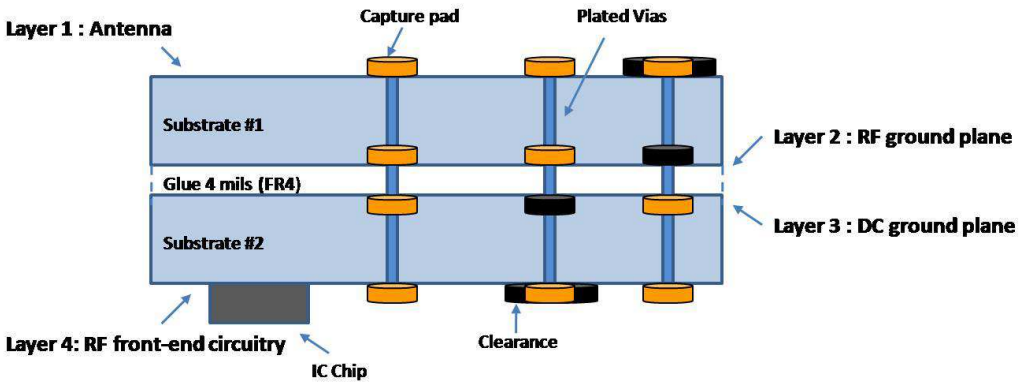

Figure 6.15: The four-layer topology (side view) of the Integrated transmitter module.

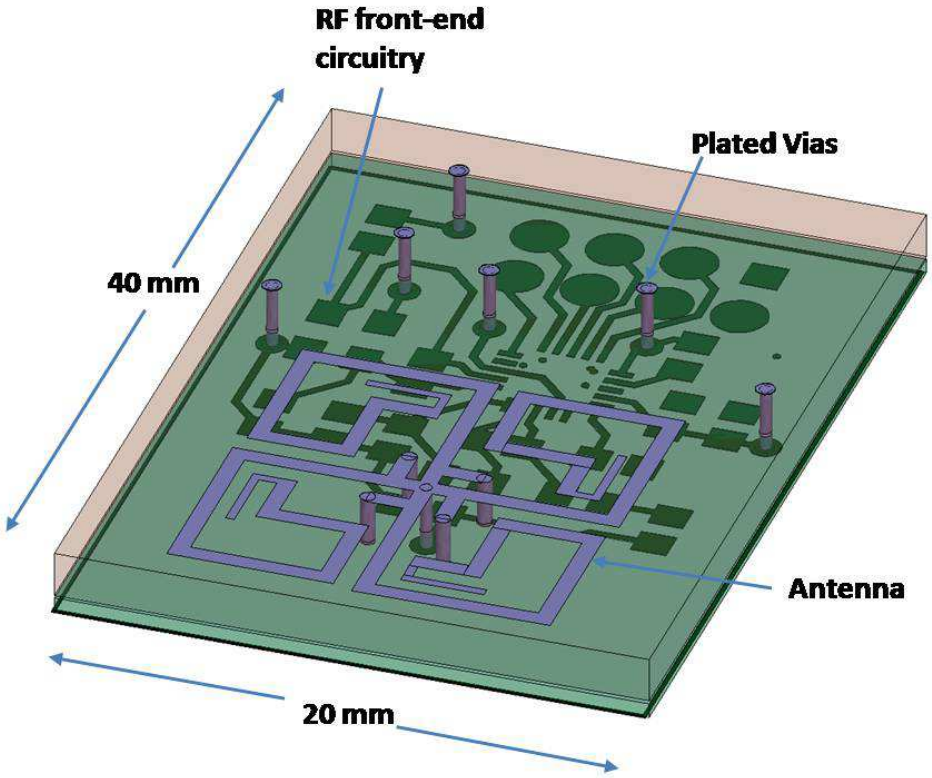

Figure 6.16: 3D view of the four-layer topology of the Integrated transmitter module.

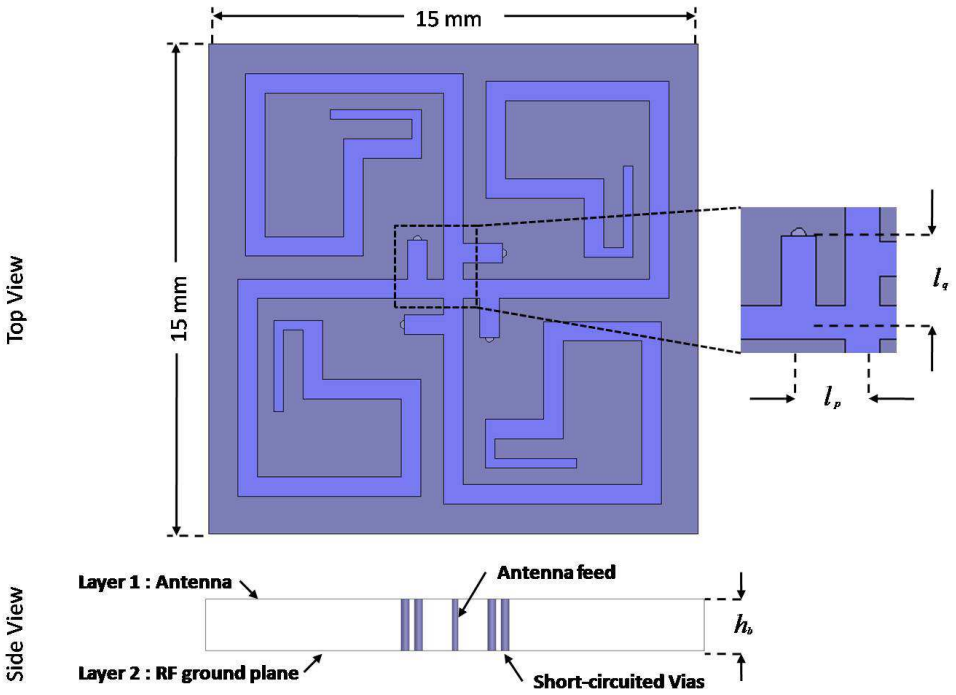

Figure 6.17: Topology of the Integrated transmitter antenna.

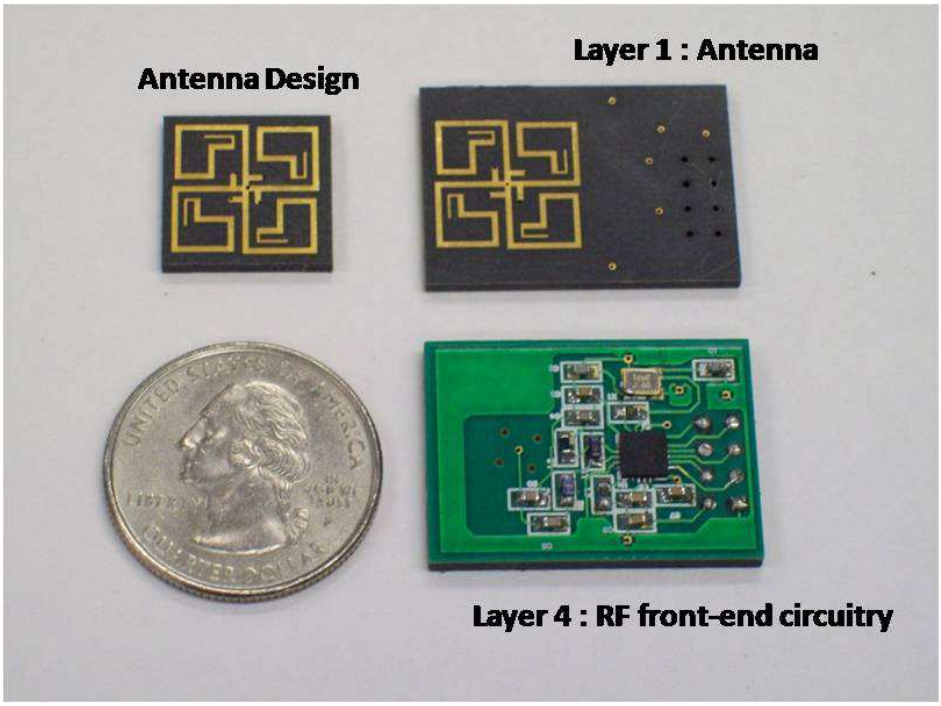

Figure 6.18: The fabricated Integrated transmitter antenna.

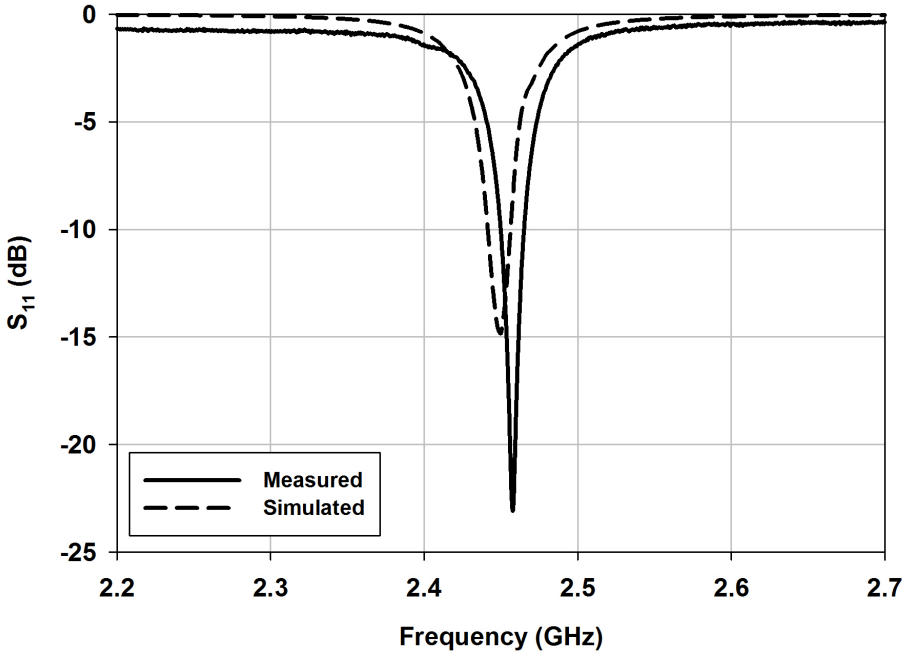

Figure 6.19: The measured and simulated input reflection coefficients of the Integrated transmitter antenna.

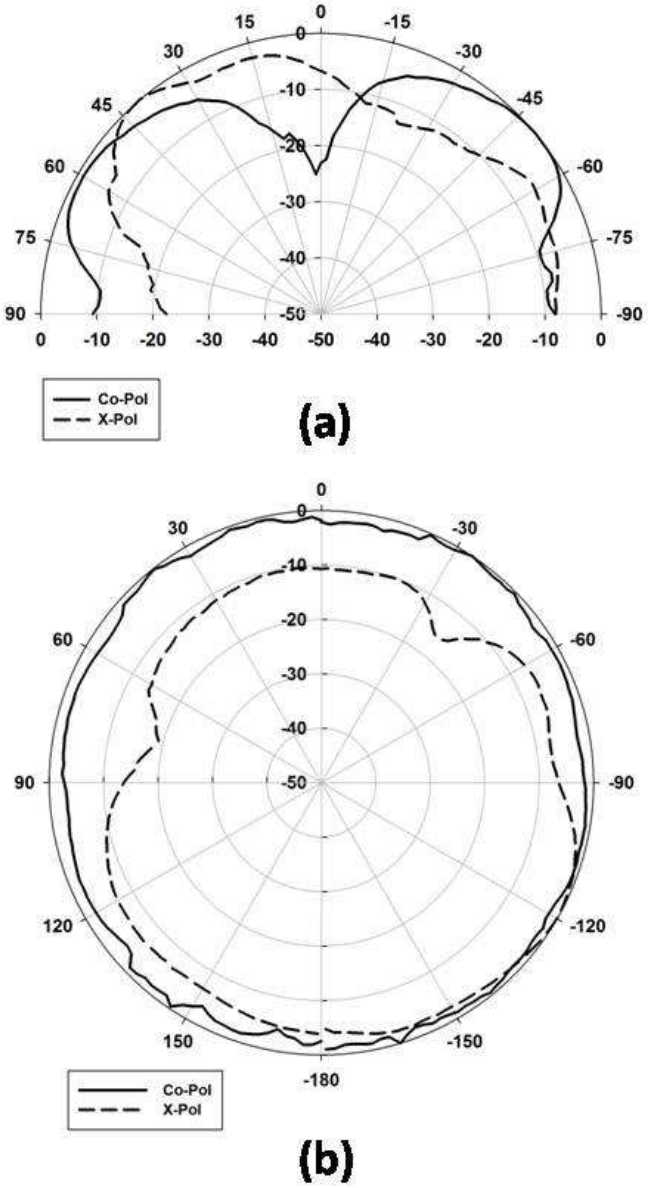

Figure 6.20: The measured far-field radiation patterns of the Integrated transmitter antenna. (a) E-Plane. (b) H-Plane.

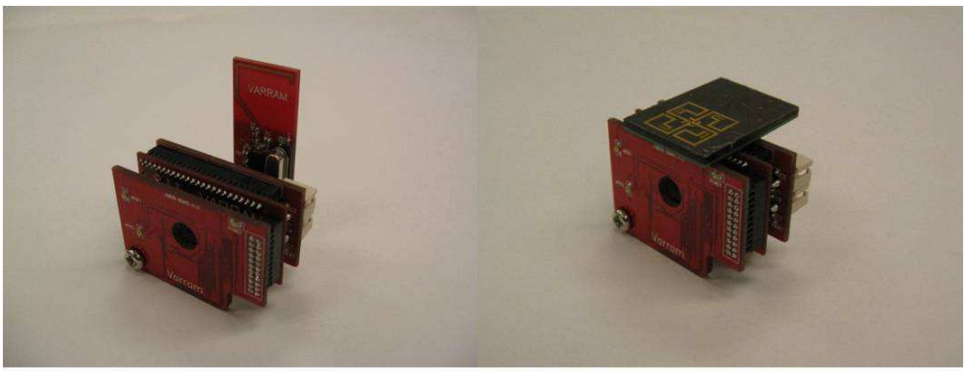

Figure 6.21: RF front-end transmitters combined with commercially-built (CMOS image sensor, microprocessor) units. (a) Commercial RF front-end transmitter with on-board antenna. (b) Fabricated Integrated transmitted module.

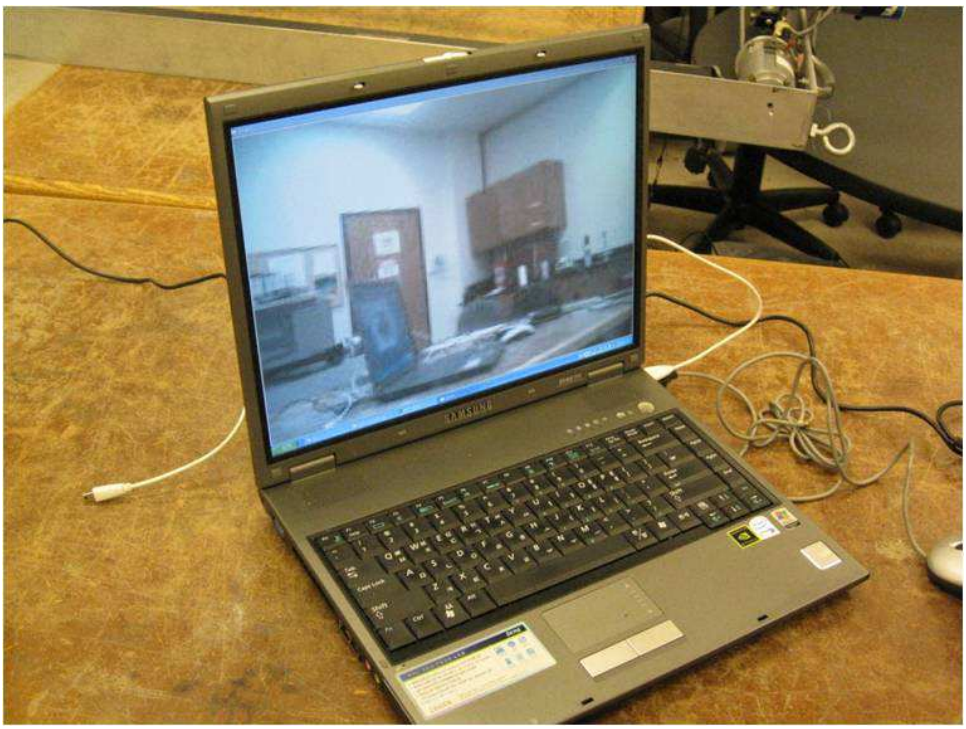

Figure 6.22: The image transmitted from the Integrated transmitter module can be observed from the screen of the computer.

CHAPTER 7

Frequency Reconfigurable Miniaturized Antenna

7.1 Introduction

A series of bandwidth enhancement techniques for electrically small resonant type antenna have been discussed in previous chapters of this dissertation. The aforementioned approaches have been based on additional modification of the impedance matching network or antenna topology. Bandwidths of each antennas have been intrinsically linked to the antenna topologies. In this chapter, a frequency reconfigurable antenna using active diodes is introduced.

At present, spectrum allocations vary based on the geographical region. For instance, a regular single-band cellular mobile phone used in Asia will most likely fail to perform adequately without additional expense in North America due to different frequency band allocations for cellular service by the local government. To mitigate this limitation, antenna engineers have commonly been designing tri-band, quad-band antennas to cover majority of the cellular mobile spectrum around the globe. While this approach has been largely effective particulary in the cellular service market, for many other application scenarios such as RFID, the antennas potentially carry the risk of cross-talk and signal interference with other wireless communication devices that operate in the adjacent frequency band. The current U.S. radio spectrum allocation chart is shown in Figure 7.1.

Figure 7.1: The US radio spectrum allocation chart.

RFID systems fall into two categories, passive and active, depending on their source of electrical power. Passive RFID tags receive power from the signal of a RFID reader through inductive coupling and therefore are limited to short ranges comparable to the size of the antenna. Active RFID tags contain both the radio transceiver and source of power. These systems use radiative coupling and therefore have higher read range and do not require line-of-sight access. Due to their on-board power source, active RFID tags operate at microwave frequencies - commonly near 430 MHz, 900 MHz, and 2.45 GHz worldwide. Research and development of antennas for RFID application has been extensively studied by various authors [109, 13, 110]. Since RFID technologies are widely used in the ISM (Industrial, Scientific, Medical) band, frequency allocation and interference with other signals become an important issue. In addition, spectral allocation by governments varies from one country to another. This can result in the RFID device being limited to operate within a certain region. In addition, operating frequencies affect the radiation characteristics of resulting radiated fields. For locating large objects, low frequencies such as 433 MHz are more applicable to avoid obstacle blockage, whereas higher frequencies can be used when a

clear line-of-sight is assured. Therefore, a multifunctional antenna capable of operating at all major frequencies used for RFID technology can alleviate and compensate the short comings that a single band antenna will experience. Recently, reconfigurable antennas with various electronic tuning capabilities have been extensively studied [111, 112, 113]. Since typical dimensions of antennas for RFID devices operating at 900 MHz range from 10 *cm* to 30 *cm*, size reduction of the antenna can enable the RFID system to be more mobile and versatile. A number of studies has shown the dimension of the antenna can be reduced through capacitive loading using PIN diodes or varactors [114, 115].

This chapter presents a compact multifunctional antenna operating at three separate frequency bands capable for worldwide active RFID usage. Frequency reconfigurability is achieved without any additional modification to the antenna topology. In what follows, the antenna design process is first described and the measurement results are later presented and discussed.

7.2 Design of the Tri-band Reconfigurable Antenna

The key function requirements are first established for active RFID application scenario. First, the antenna must be capable of operating at designated active RFID frequency bands worldwide. The frequency tuning range of the antenna is determined for each three frequency bands (430 MHz to 460 MHz, 800 MHz to 840 MHz and 2.4 GHz to 2.6 GHz). Selection of the frequency band is made utilizing a multi-switch diplexer which will ultimately be controlled via digital interface. Second, the total real estate of the antenna must be minimum for effective integration to the system platform. The system topology of the active RFID is presented in Figure 7.2.

Three sub-level antennas are designed on a 50 *mm* $\times$ 50 *mm* ground plane. $\lambda/4$ slot antenna topology is used for all sub-level antennas due to its omni-directional behavior, ease of miniaturization, and planar geometry. A $\lambda/4$ slot antenna at first resonance can

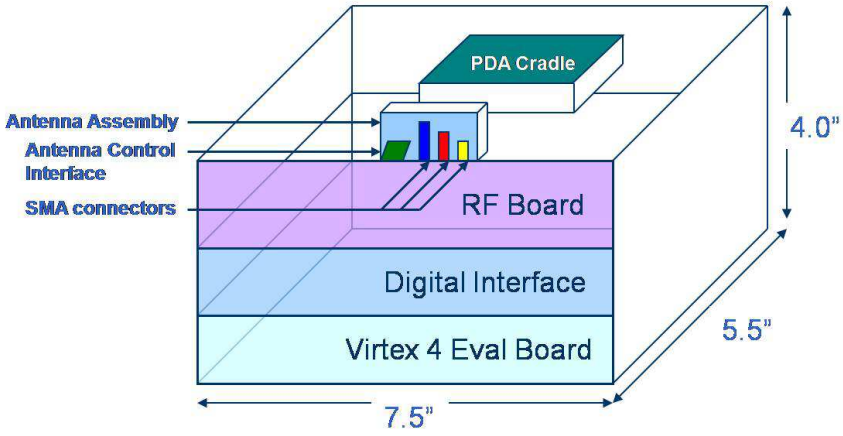

Figure 7.2: System configuration of the active RFID system

be considered a transmission line of equivalent length. Loading the structure with shunt capacitor increases the line capacitance and results in decrease of resonant frequency of the transmission line. The line capacitance can be tuned electronically using a varactor diode to achieve reconfigurability through modulation of the DC bias voltage. For the sub-antenna design for the 430 MHz and 800 MHz band, the lumped capacitor is replaced with a SMT MTV4030 varactor diode from MicroMetrics. The capacitance of the varactor ranges from 1.36 pF to 0.32 pF as the bias voltage increases from 0 V to 30 V. The performance graph of the varactor is presented in Figure 7.3. The placement of the varactor is determined by a series of full wave simulation based on method of moments [34] to achieve accurate tuning ability throughout the frequency bands. The final location of the varactors are optimized so that maximum frequency tuning ranges can be achieved with relatively low voltage levels at both frequency bands. This enables the antenna to be ultimately powered by small, light-weighted batteries, increasing its portability and mobility. The schematic of the proposed Tri-band antenna is shown in Figure 7.4. The 400 MHz and the 860 MHz sub-level antennas are located in the lower and mid portion of Figure 7.4 (a) respectively. The antennas are fed with open-stub microstrip lines with an impedance of 50Ω. Impedance matching is achieved by adjusting the location (l_{p1}, l_{p2}, l_{p3}) of the microstrip feed and the length of the open-circuit stub (l_{m1}, l_{m2}, l_{m3}) to compensate the reactance of the feed. Biasing networks

for both sub-level antennas consist of DC feed lines for RF-DC isolation. The biasing network is shown in Figure 7.4 (c). The physical design parameters of the antenna is presented in Table 7.1.

l_{s1}	l_{s2}	w_1	l_{s3}	w_2
42.6	27	2	28	2
l_{s4}	w_3	l_{p1}	l_{m1}	l_{p2}
33	2	14.8	22	30
l_{m2}	l_{p3}	l_{m3}	l_{v1}	l_{v2}
10.2	5.6	1.9	9.8	10.0

Table 7.1: Design parameters of the Tri-band reconfigurable antenna (*mm*).

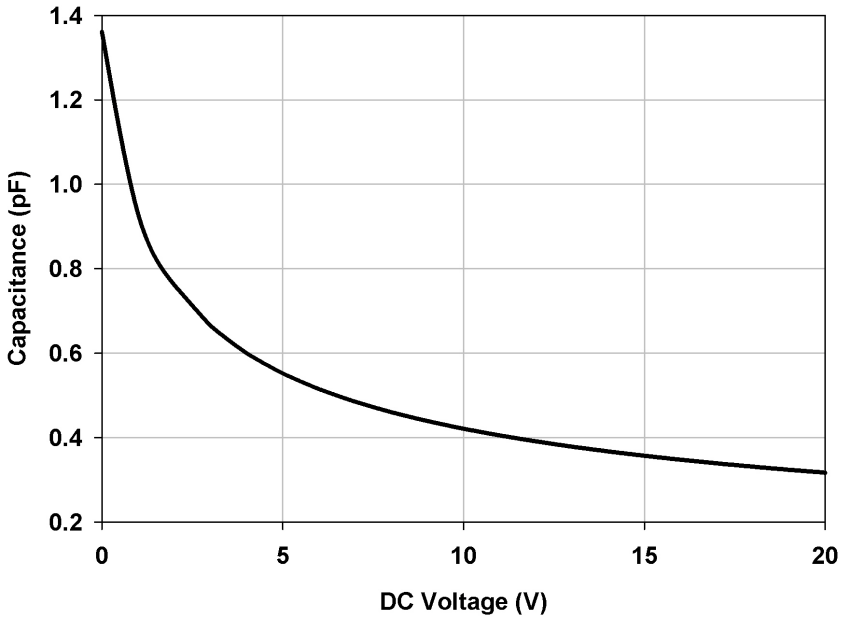

Figure 7.3: Capacitance vs. DC bias voltage of the MTV4030 varactor

Due to its relatively high operating frequency and therefore, less need for miniaturization, the 2.4 GHz sub-level antenna is designed without additional capacitive loading technique. A $\lambda/4$ notch antenna topology is adopted for the 2.4 GHz sub-level antenna, as shown in the upper portion of Figure 7.4 (a). The antenna is matched to a line impedance of 50Ω by choosing the appropriate location (L_{p1}, L_{p2}, L_{p3}) and length of the stub (L_{m1},

L_{m2}, L_{m3}). As discussed in previous chapters of this dissertation, two separate resonance behaviors can be achieved through optimizing the microstrip feed. The first resonance is the principle resonance which is inversely proportional to the length of the antenna. The second resonance occurs when the electric field along the slot is manipulated by the microstrip feed from the edge of the slot antenna. The electric field of the slot excited by the return current on the ground plane of the microstrip line is canceled out by the tangential component of the electric field created by the microstrip line, introducing a fictitious short circuit with a resonant frequency slight higher than the first resonance. By adjusting the location of the microstrip feed, a dual-band or wideband behavior is achieved.

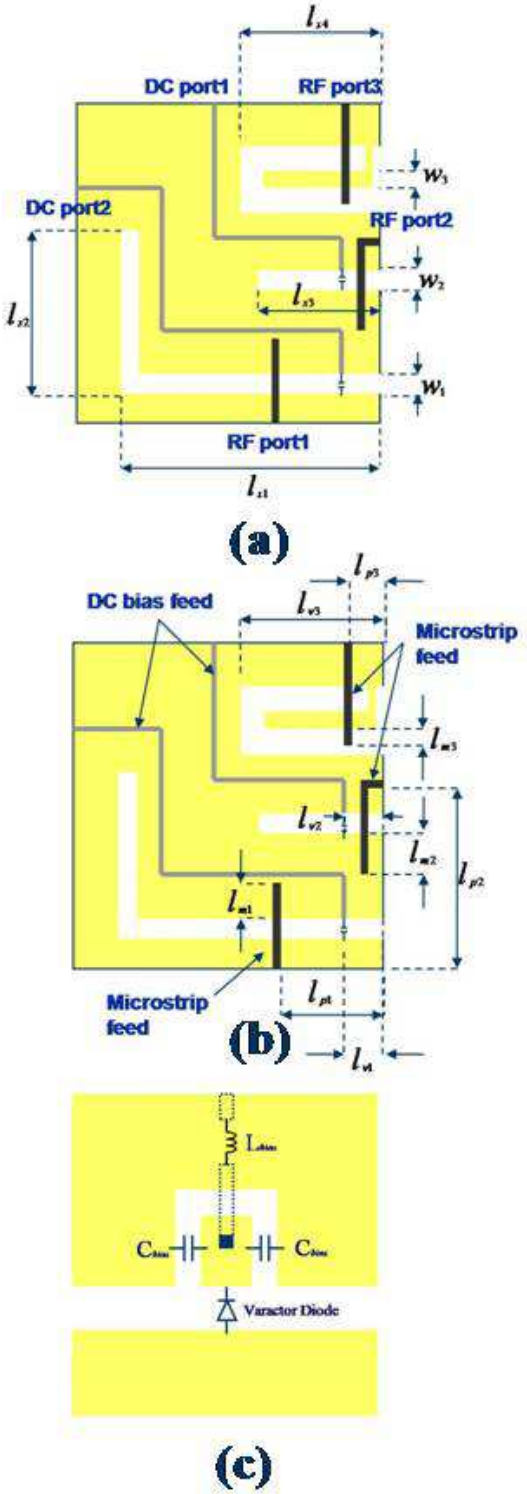

Figure 7.4: Topology of the Tri-band reconfigurable antenna. (a) Topology of the sub-level antennas. (b) Topology of the microstrip and DC bias feed lines. (c) The biasing network.

7.3 Measurement and Discussion of the Tri-band Reconfigurable Antenna

The Tri-band reconfigurable antenna is simulated using IE3D and fabricated on a 0.5 *mm* thick RO4003 substrate from Rogers Corp with a dielectric constant of $\varepsilon_{ra} = 3.4$, loss tangent of $\tan\delta_a = 0.0027$. The input reflection coefficients S11 are measured across all frequency bands and the results are shown in Figure 7.5, Figure 7.6, Figure 7.7 respectively. it can be seen from their respective figures that the 400 MHz and 860 MHZ sub-level antennas are well matched throughout the frequency tuning range of more than 40 MHz and 140 MHz, respectively. The DC voltage ranges remain relatively small with the maximum range being less then 4 V. However it should be noted that when the DC bias voltage exceeds 4 V, the resonant frequency begins to saturate and ultimately features very limited frequency tuning capabilities. The 2.4 GHz sub-level antenna is also well matched, displaying more than 8% 2:1 VSWR bandwidth from 2.4 GHz to 2.6 GHz

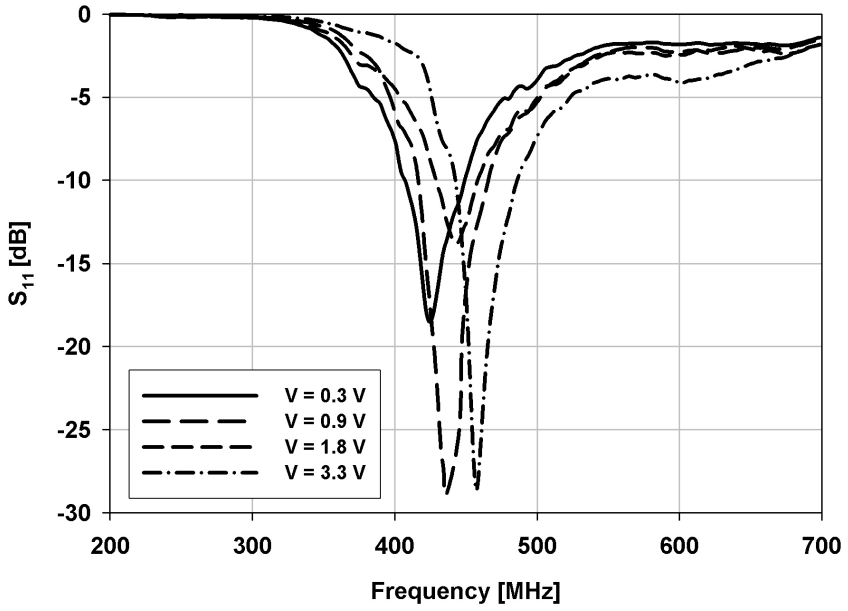

Figure 7.5: Measured input reflection coefficient of the Tri-band reconfigurable antenna at 400 MHz band.

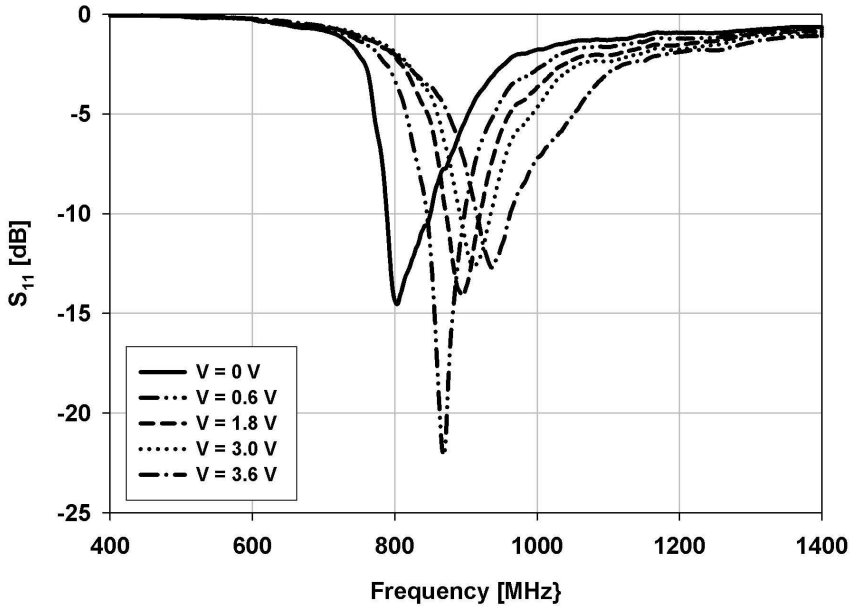

Figure 7.6: Measured input reflection coefficient of the Tri-band reconfigurable antenna at 860 MHz band.

The DC-RF isolations are measured to be less than 20 dB as shown in Figure 7.8. The electric current distributions of the simulated antenna during excitation (radiation) of each sub-level antennas can be seen in Figure 7.9. The simulations indicate the undesired electromagnetic couplings of adjacent sub-level antennas are limited. The RF isolation levels are shown in Figure 7.10.

The far field co-polarized and cross-polarized radiation patterns of these antennas are measured in the E- and H-planes inside the anechoic chamber of the University of Michigan. A log-periodic antenna was used as the reference antenna for the Tri-band sub-level antennas at 400 MHz and 860 MHz band whereas a double ridged horn antenna was used as the reference antenna for the 2.4 GHz band. The measured radiation patterns at each frequency band are presented in Figure 7.11, Figure 7.12 and Figure 7.13. The radiation pattern is observed to remain consistent as the bias DC voltage changes for both 400 MHz and 860 MHz band. The cross polarization levels are relatively small throughout the frequency bands. Cross polarizations are mostly attributed to the close proximity of SMA

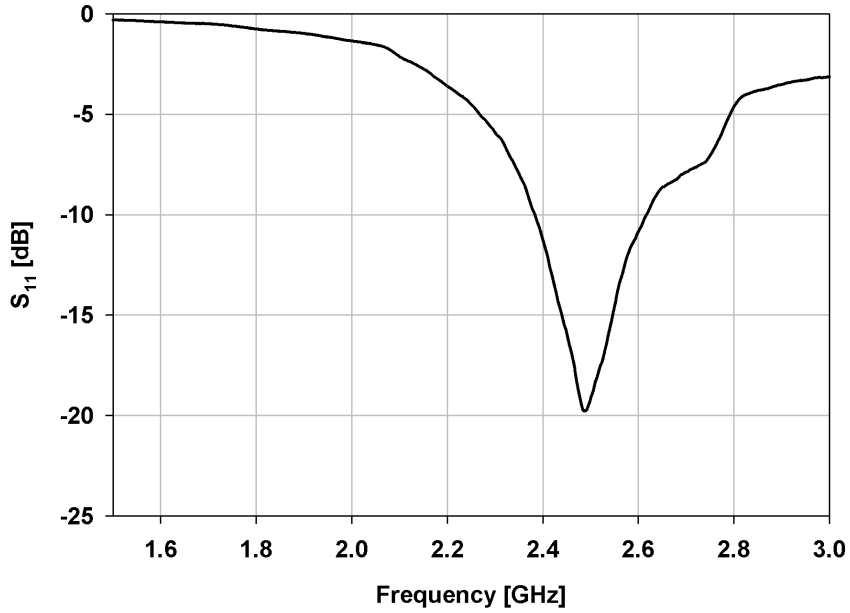

Figure 7.7: Measured input reflection coefficient of the Tri-band reconfigurable antenna at 2.4 GHz band.

connectors and cables to the antenna. When the ground plane is small compared to the wavelength, the radiated fields are capable of inducing significant currents on the feeding cables which re-radiates. In addition, the contribution of the anechoic chamber gives rise to cross polarizations at the low 400 MHz band. It can be noted that ripples are observed in the E-plane radiation pattern in Figure 7.12, which is unusual for electrically small antennas. Finite ground plane size contributes to increased levels of edge diffraction introducing ripples in the measured pattern as a result of diffracted energy. In addition, it is discovered that close proximity of the connectors to the open-circuit edge of the $\lambda/4$ slot antenna attributes to increased pattern distortion. Basically, the open-circuit boundary at the edge of the slot antenna results in maximum voltage, inducing the currents on the connectors and cable and ultimately distorting the far field radiation pattern. Rearranging the antennas and the connector feeds can significantly reduce the induction and improve the radiation pattern results for future designs. The fabricated Tri-band reconfigurable antenna can be seen in Figure 7.14.

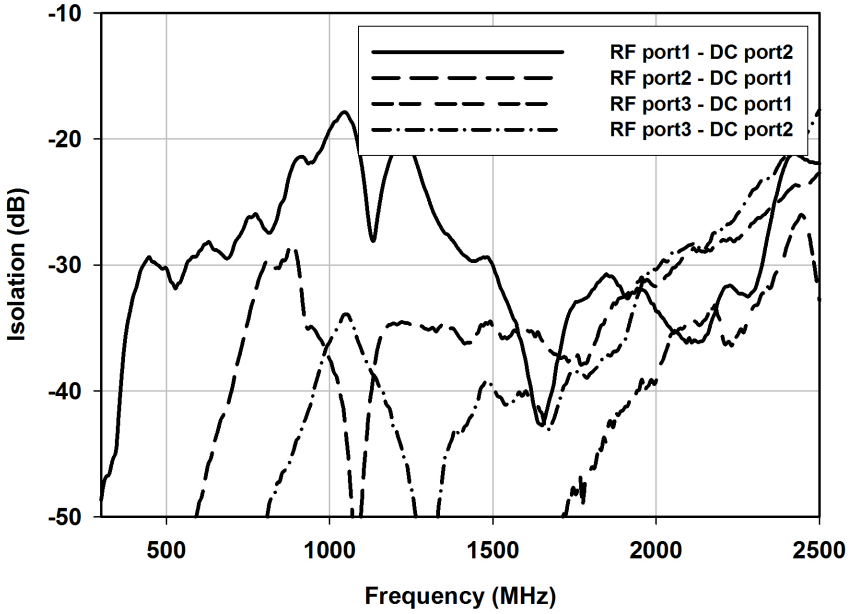

Figure 7.8: Measured RF-DC port isolations of the Tri-band reconfigurable antenna.

The gain of the antennas are also measured and presented in Table 7.2 and Table 7.3. The relatively lower gain at 400 MHz and 860 MHz bands are results of a number of factors. The relatively small electrical dimensions of each sub-level antennas are further reduced as a result of capacitive loadings. Naturally, gain is further reduced. In addition, the finite ground plane size compared to the wavelength results in significant back radiation. Finally, strong edge currents on the boundary of small ground planes cause increased ohmic losses. However when the designed antenna is implemented on the active RFID system platform, degradations of radiation patterns and gain are expected to be reduced since the platform can be regarded as an electrically large ground plane.

Frequency	DC Voltage	Gain	Frequency	DC Voltage	Gain
415 MHz	0 V	-1.7 dBi	800.5 MHz	0 V	0.6 dBi
425 MHz	0.6 V	-1.7 dBi	865 MHz	0.6 V	0.43 dBi
445 MHz	1.8 V	-1.4 dBi	895 MHz	1.8 V	0.75 dBi
460 MHz	3.3 V	-1.5 dBi	930 MHz	3.0 V	0.33 dBi

Table 7.2: Measured gain of the Tri-band reconfigurable antenna.

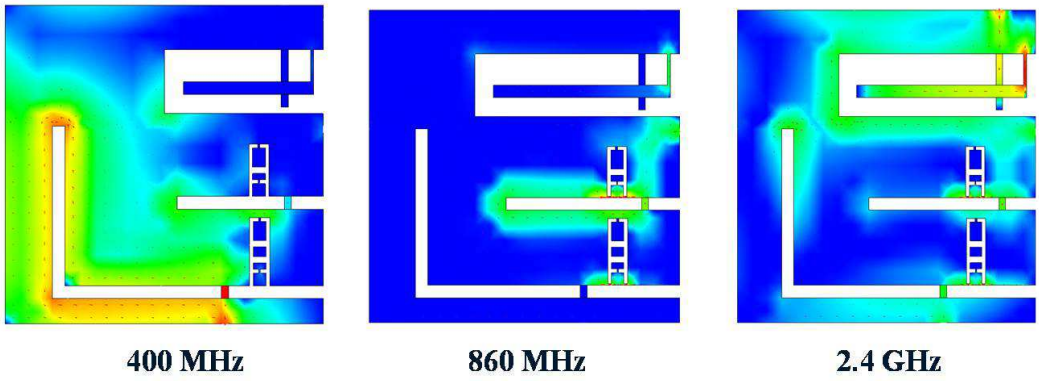

Figure 7.9: Electric current distribution of the antenna at each frequency band.

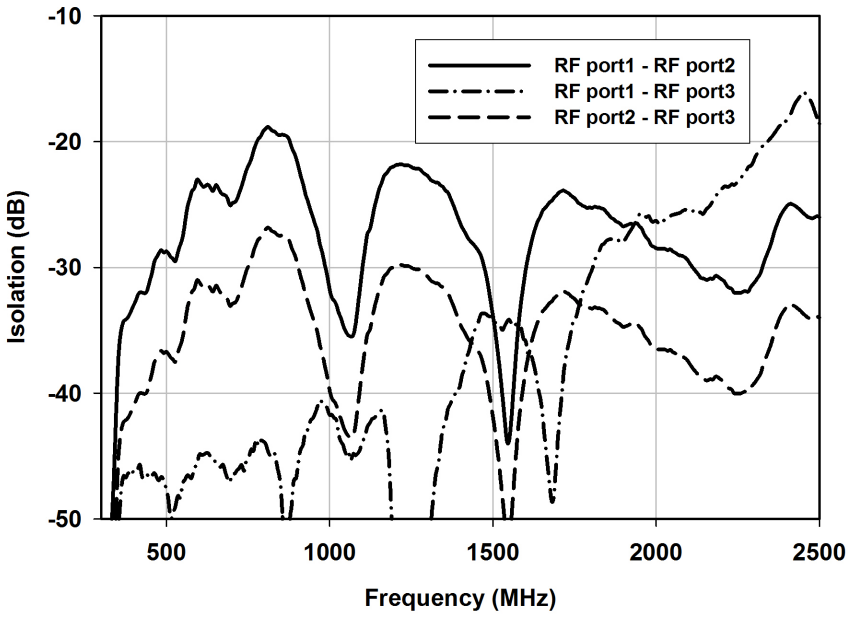

Figure 7.10: Measured RF-RF port isolations of the Tri-band reconfigurable antenna.

7.4 Summary

This chapter describes an electrically small Tri-band reconfigurable antenna. The antenna employs two different approaches for bandwidth enhancement and frequency tuning capabilities. Given the frequencies of operation of the proposed antenna, the antenna is capable of being used as worldwide active RFID application scenarios. The proposed antenna features simple frequency tuning interface, high port-to-port isolations and sufficient gain.

Frequency (GHz)	2.45	2.51	2.58
Gain (dBi)	1.1	1.2	1.5

Table 7.3: Measured gain of the Tri-band reconfigurable antenna.

The radiation performance of the antenna is dependent on the ground plane dimension. Therefore performance improvements can be expected after final paste-on type integration with the active RFID system.

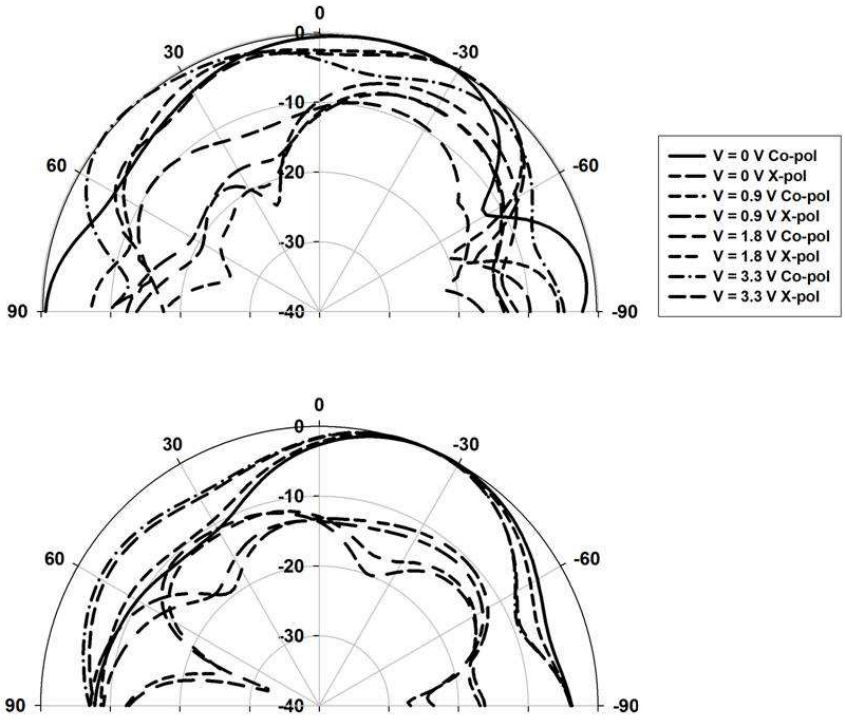

Figure 7.11: Measured E- (top) and H- (bottom) Planes of the Tri-band reconfigurable antenna at 400 MHz band.

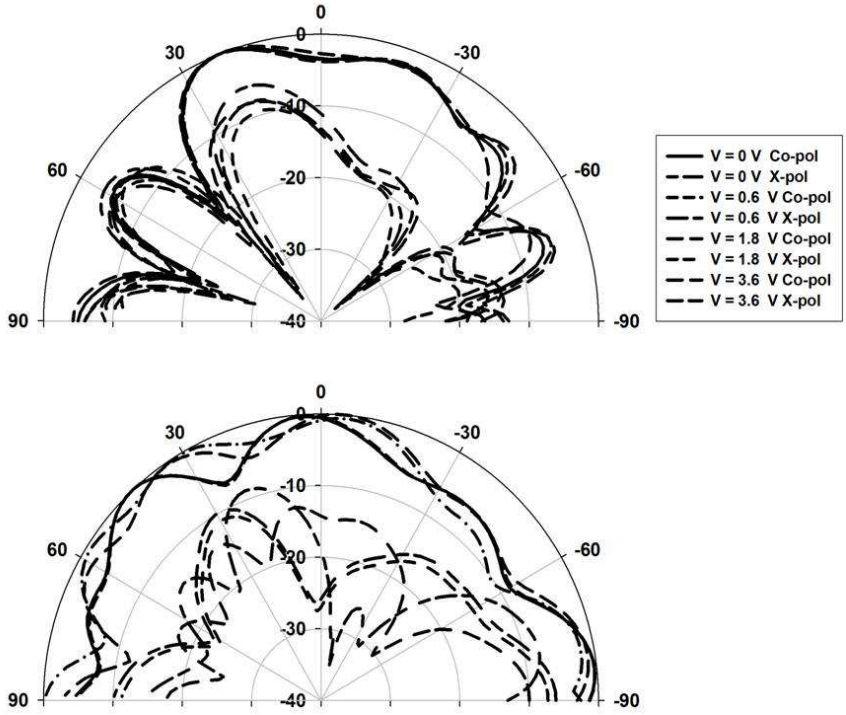

Figure 7.12: Measured E- (top) and H- (bottom) Planes of the Tri-band reconfigurable antenna at 860 MHz band.

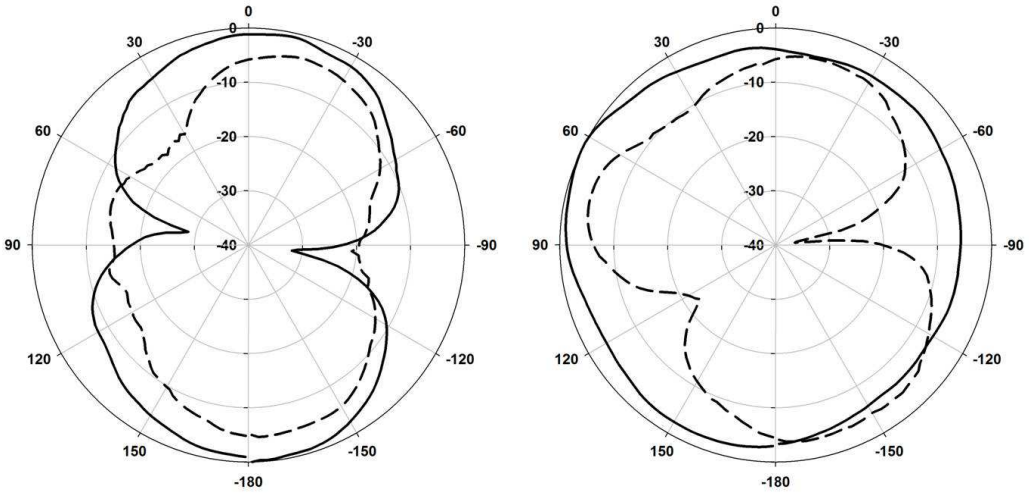

Figure 7.13: Measured E- (left) and H- (right) Planes of the Tri-band reconfigurable antenna at 2.4 GHz band. Solid line: Co-pol. Dotted line: Cross-pol.

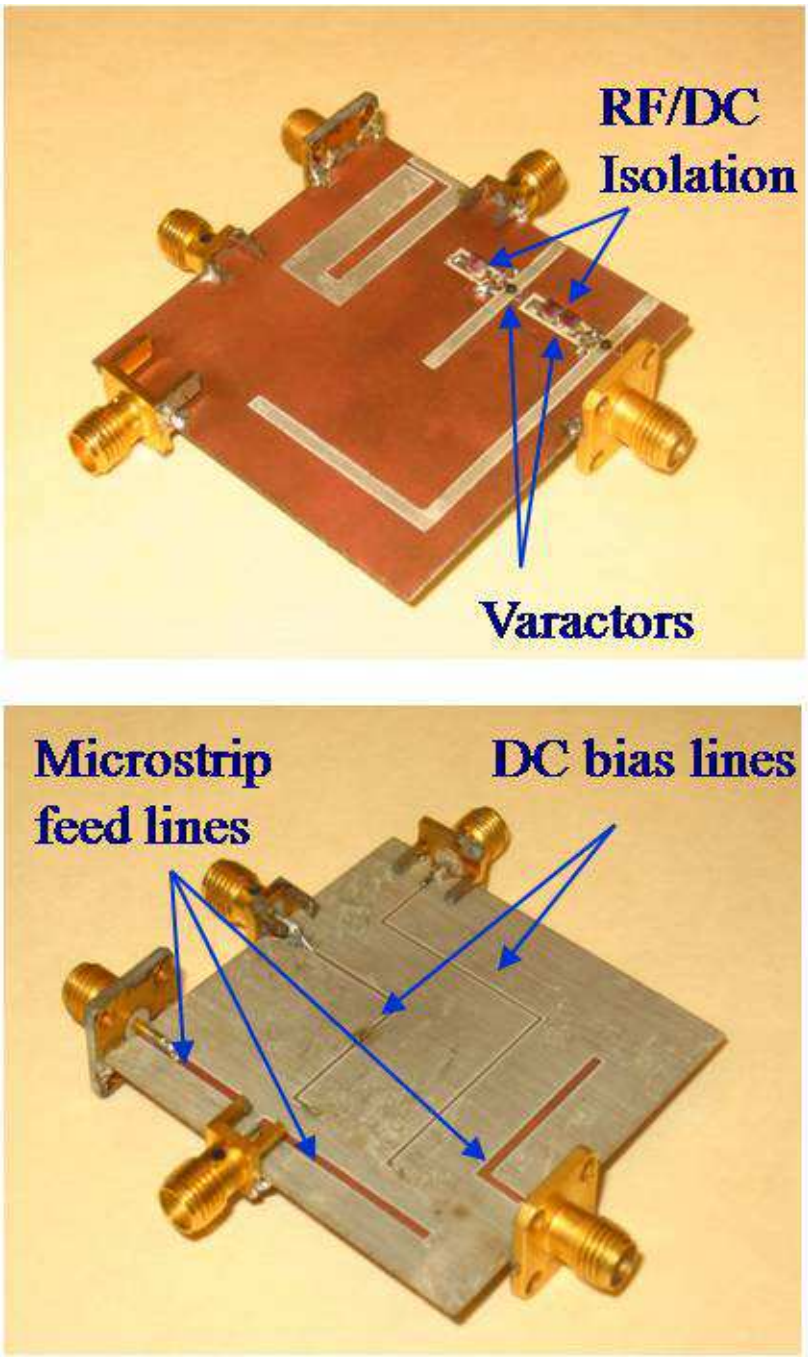

Figure 7.14: The fabricated Tri-band reconfigurable antenna. Top view (top). Bottom View (bottom).

CHAPTER 8

Conclusion and Future Work

8.1 Conclusion

Efforts to reduce the physical dimension of an antenna has been vigorously studied for many decades. Through the collection of such efforts, the effects of size reduction on the performance of an antenna are fairly well understood matters in present day. The fundamental limitations established by Wheeler and Chu have been referenced as theoretical guidelines in acquiring smaller antenna size at the expense of radiation resistance, antenna Q (bandwidth) and polarization [116, 17]. However, it should be noted that the fundamental limitation applies only to fundamental antennas - a resonant antenna that has been discussed in Chapter 1. Therefore while performance degradation is inevitable using contemporary materials as the resonant antenna volume becomes smaller, it is still possible to overcome this restriction by taking a different route. Various techniques including the utilization of mutual coupling effects of parasitic elements, integration of transistors and capacitive and inductive loading methods are now employed to mitigate and curb the inverse relationship between antenna volume and performance. Using these techniques, an electrically small resonant antenna is modified to exhibit multiple resonances and enhanced bandwidths. Artificial materials are developed to reduce material loss as antenna dimensions become smaller. Surface mount components such as diodes and transistors are also

used to control polarizations.

This dissertation continues the path of designing fully integrated, electrically small antennas in a controlled manner. Antenna miniaturization techniques and topologies are applied in such a manner to preserve the behavior and radiation characteristics of the originally-sized antenna. The contributions of this dissertation includes:

- A method to reduce the dimension of a cavity-backed slot antenna is synthesized. For a simple straight slot antenna, this technique can reduce the overall occupied volume of the modified cavity backing the slot antenna by more than 65% without effecting the high radiation efficiency of the antenna. This facilitates proper fabrication and integration of miniaturized slot antennas on multi-layer substrates.

- A platform-integrated low-profile antenna with high isolation levels to its environment is reported. Through this approach, complex package-level designs and simulations can be greatly simplified as the antenna exhibits similar behavior when integrated as it does in open-space. The method enables the realization of unidirectional cavity-backed slot antennas with heights less than $\lambda/100$, minimizing surface intrusion or protrusion for platform antenna implementations.

- An infinitesimal electric dipole radiating vertical polarization with less than $\lambda/100$ height is realized. The theoretical equivalence relation between a short electric dipole and a magnetic loop at resonance is valid under the following preconditions: 1) The existence of uniform in-phase magnetic current, 2) Impedance matching to the low radiation resistance of the magnetic loop. This dissertation is the first to satisfy both requirements to the best of my knowledge.

- An omnidirectional antenna with height less than $\lambda/80$ featuring vertical polarization perpendicular to the horizontal plane is fully integrated with the wireless communication platform in a number of scenarios. Performance and measurements of the

wireless communication devices verifies the advantages of the discussed techniques and topologies.

The introduced techniques and approaches can be applied separately or in conjunction with other techniques to design small, integrated antenna for wireless communication systems. Theses methods may be more advantageous especially at lower frequencies for applications such as near-ground terrestrial communication, polarimetric synthetic aperture radar, and radio frequency identification.

8.2 Future Work

8.2.1 Platform-embedded Slot Array

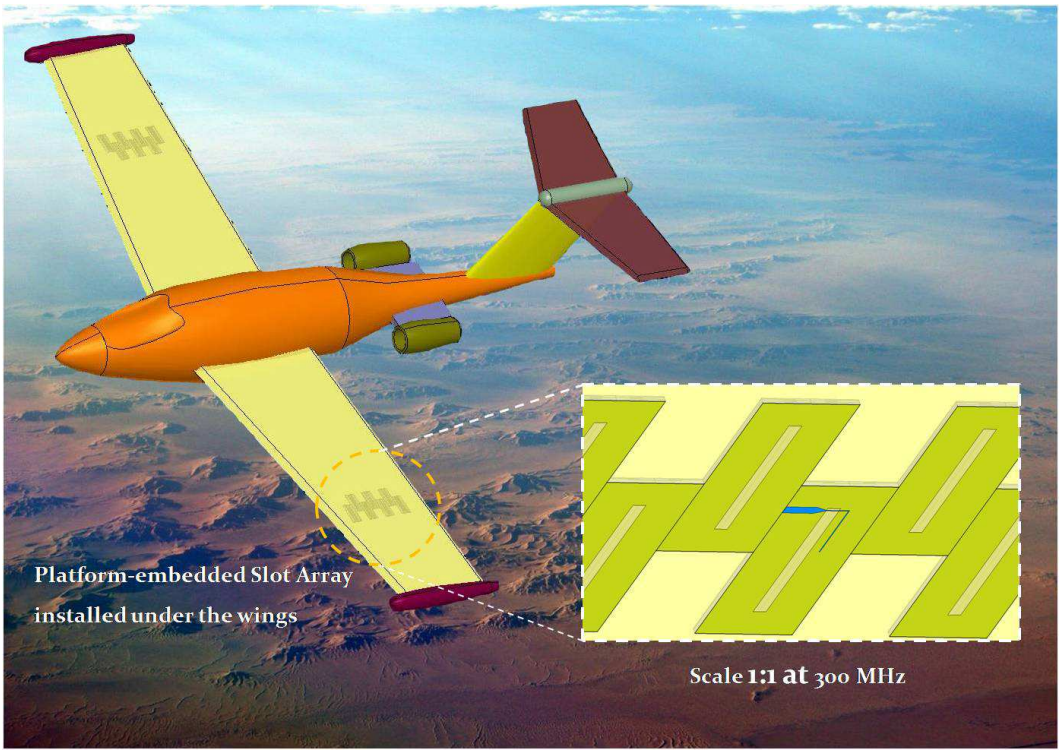

Figure 8.1: Possible application for the platform-embedded slot array as polarimetric synthetic aperture radar antenna.

Further investigation regarding transformation of single element platform-embedded slot antenna topologies discussed in Chapter 2-3 into multi-element platform-embedded slot array is a promising task. The advantages of the proposed platform-embedded slot array would be twofold: 1) The near-flat profile of the array can be flush-mounted or surface-mounted with minimum modification of the platform, 2) The small physical dimensions of the platform-embedded slot antenna topologies can be implemented with very close inter-element spacings and limited mutual coupling effects. Thus, undesired grating lobes can be avoided while featuring very small array dimension. A potential application for the proposed array is visualized in Figure 8.1. By employing Ultrasonic consolidation process, it will be interesting to study conformal topologies that can be integrated with curved platforms.

8.2.2 Integrated Antenna using Multi-layer Packaging Technology

The miniaturized antennas radiating vertical polarized waves with respect to the horizontal plane can be adapted in conjunction with multi-layer packaging technology for system-in-package (SiP) solutions. Traditional microelectronic packaging technology involves numerous components connected via interconnected boards, often resulting in increased volume, weight and complexity. In addition, the interconnects can potentially introduce stray capacitance and stray inductance, which can severely effect the performance of an antenna. Comparatively, organic-based SiP solutions such as liquid crystal polymer (LCP) or low-temperature co-fired ceramics (LTCC) have attractive electrical characteristics, reduced number of interconnects and increased density, making compact vertical integration feasible. However, the relatively high dielectric constant of ceramic introduces unwanted surface waves and substrate modes within the ceramic package. Such adverse effects can degrade the behavior of the integrated antenna. Therefore, it will be useful to further investigate methods of integrating the miniaturized antennas topologies with 3D embedded wireless communication modules as depicted in Figure 8.2.

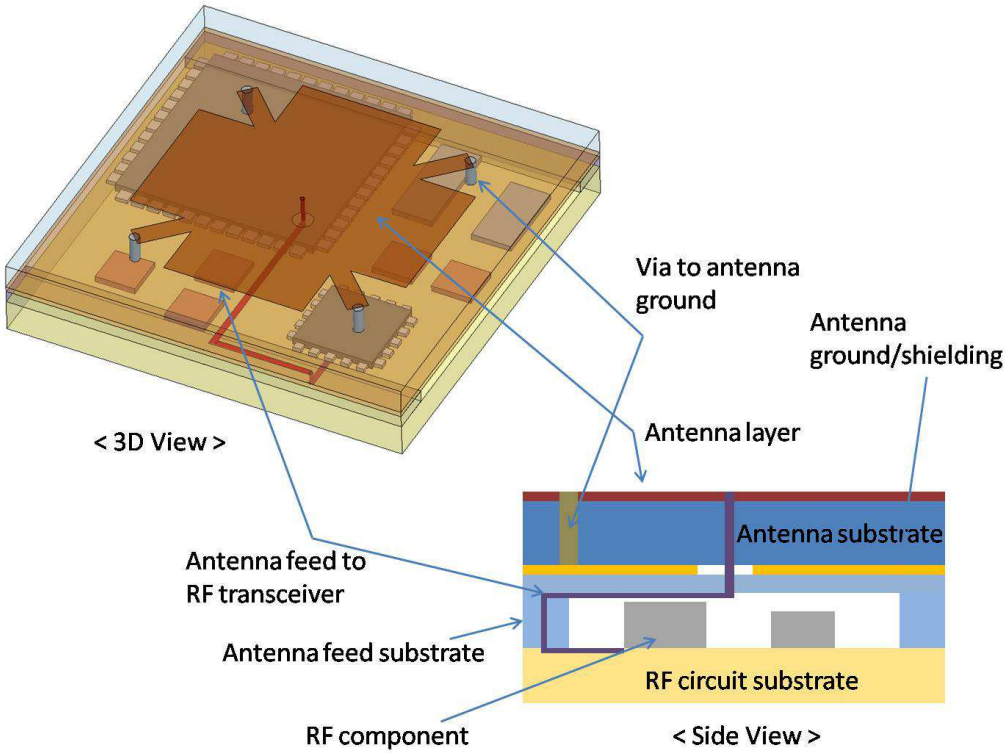

Figure 8.2: Topology of the Integrated transceiver module.

8.2.3 Parasitic Platform Antenna

Electromagnetic resonance is induced through the creation of standing waves over an aperture. It is well known for small antennas implemented on electrically small platforms, that the platform significantly contributes to the far-field radiation. The benefits of designing a small antenna element that parasitically couples energy into the platform in a controlled manner would be aplenty. First, high levels of displacement current will be excited on the platform, creating various standing waves. Hence, numerous electromagnetic resonances are induced and radiation resistance and bandwidth are increased. Second, by creating an array of these elements, the entire platform can be utilized as an efficient radiating element at the frequency of choice. If successful, such approach will have a profound effect on contemporary antenna theory.

APPENDICES

Appendix A

Layouts of the Integrated Transmitter Module

The designed layouts of the RF front-end Integrated transmitter module discussed in Chapter 6 are provided as follows.

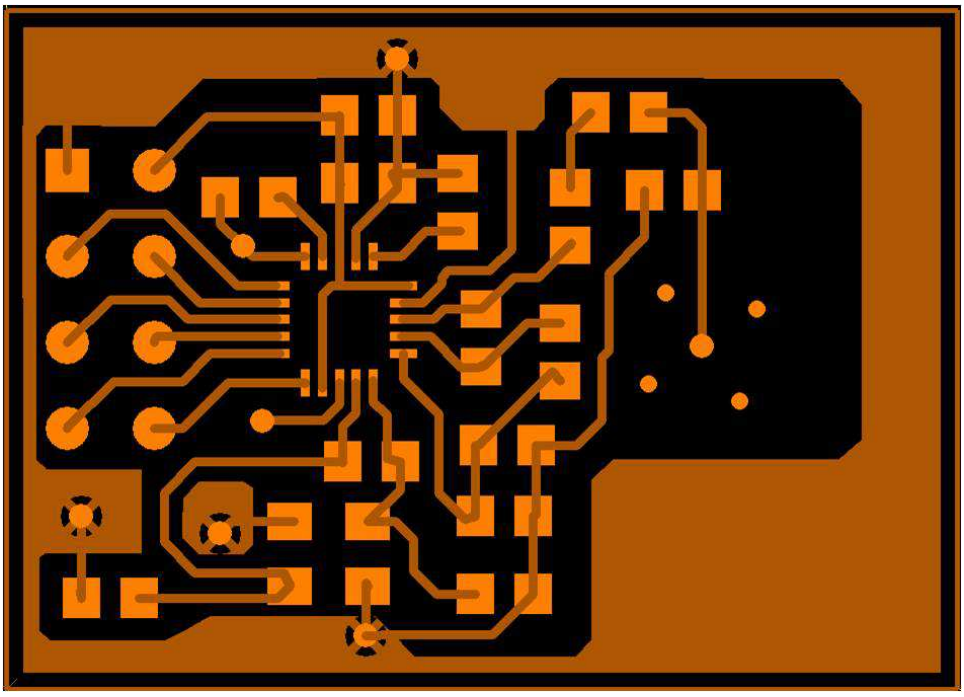

Figure A.1: The redesigned RF front-end transmitter circuitry (Layer 4).

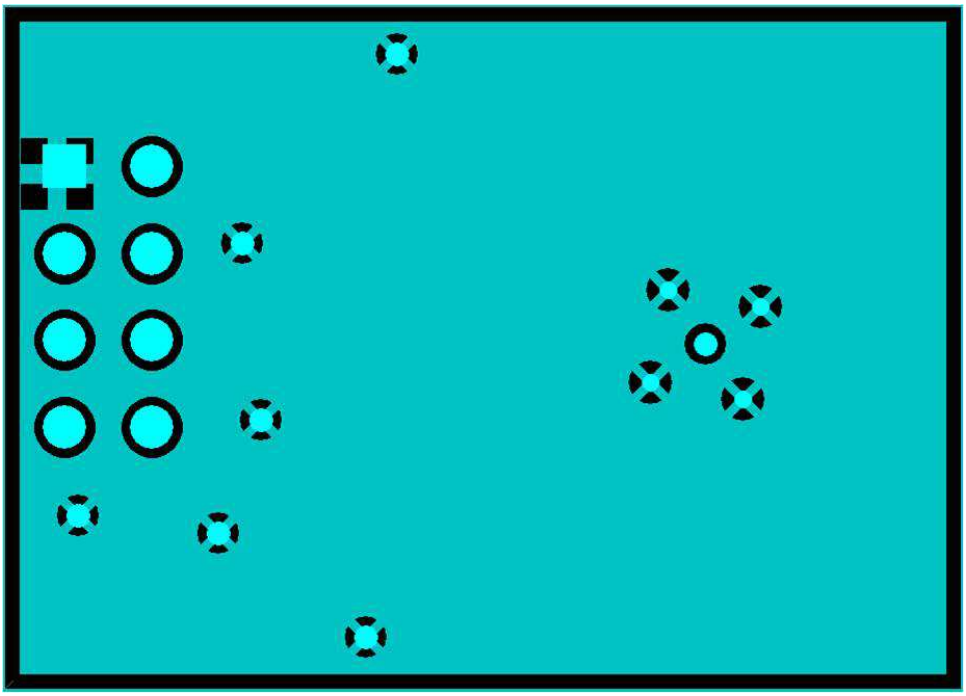

Figure A.2: The redesigned DC ground plane (Layer 3).

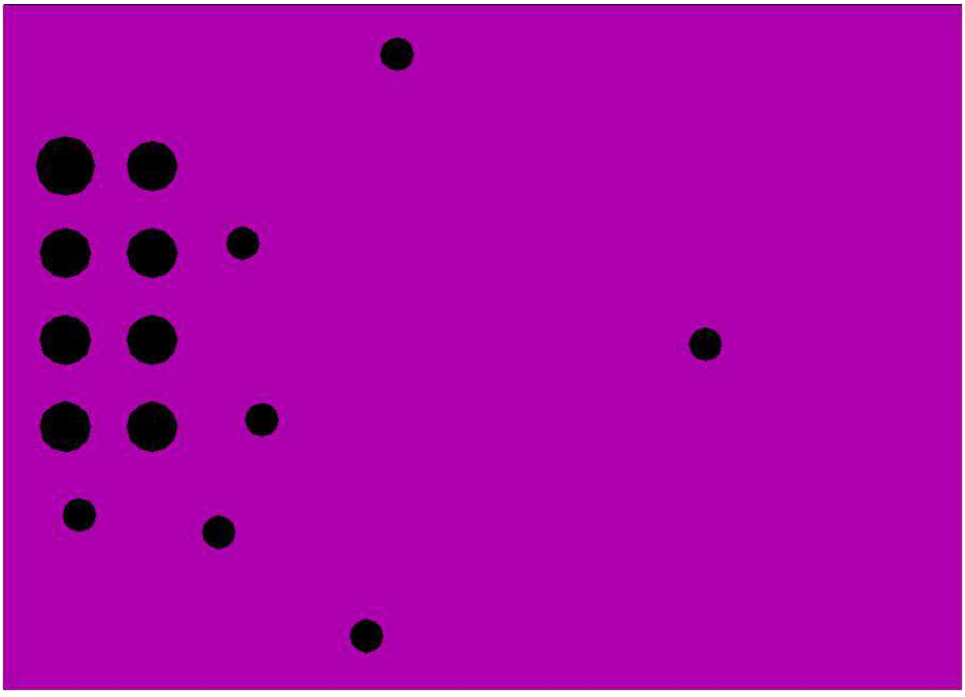

Figure A.3: The RF ground plane (Layer 2).

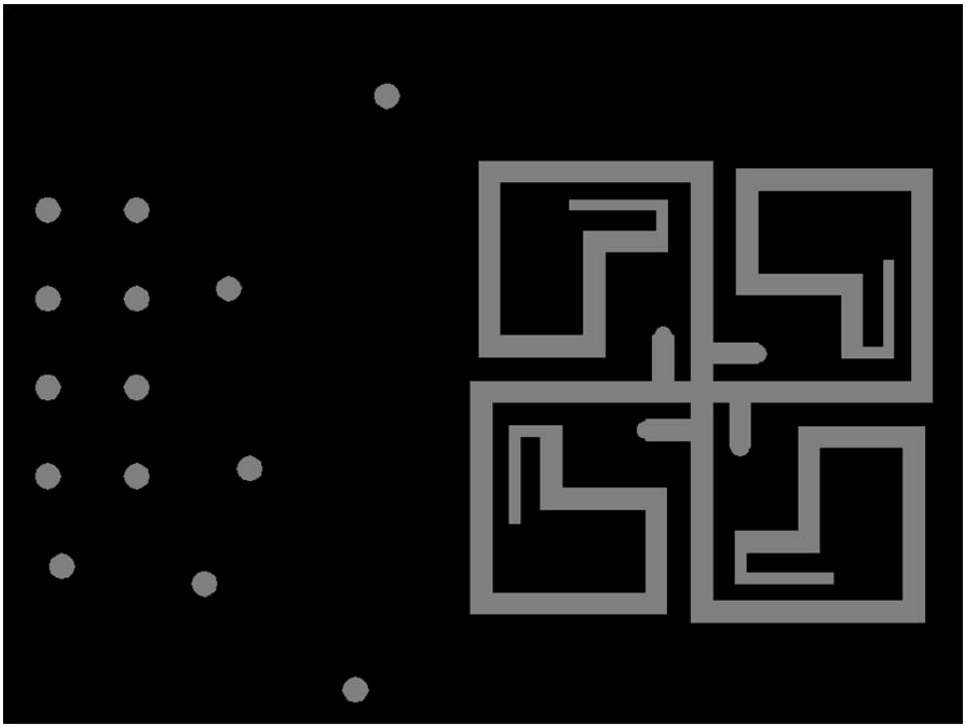

Figure A.4: The Integrated transmitter antenna layer (Layer 1).

BIBLIOGRAPHY

BIBLIOGRAPHY

[1] J. D. Kraus, Ed., *Antennas*. McGraw-Hill, 1988.

[2] J. Rashed and C. Tai, "A new class of resonant antennas," *IEEE Transactions on Antennas and Propagation*, vol. 39, no. 9, pp. 1428–1430, Sept. 1991.

[3] C. Puente-Baliarda, J. Romeu, and A. Cardama, "The Koch monopole: A small fractal antenna," *IEEE Transactions on Antennas and Propagation*, vol. 48, no. 11, pp. 1773–1781, Nov. 2000.

[4] C. Puente-Baliarda, J. Romeu, R. Pous, and A. Cardama, "On the behavior of the Sierpinski multiband fractal antenna," *IEEE Transactions on Antennas and Propagation*, vol. 46, no. 4, pp. 517–528, Apr. 1998.

[5] S. Best, "On the behavior of the Sierpinski multiband fractal antenna," *IEEE Antennas and Wireless Propagation Letters*, vol. 2, pp. 197–199, 2003.

[6] J. Zhu, A. Hoorfar, and N. Engehta, "Bandwidth, cross-polarization, and feed-pont characteristics of matched Hilbert antennas," *IEEE Antennas and Wireless Propagation Letters*, vol. 2, pp. 2–5, 2003.

[7] K. Carver and J. Mink, "Microstrip antenna technology," *IEEE Transactions on Antennas and Propagation*, vol. AP-29, no. 1, pp. 2–24, Jan. 1981.

[8] W. Stutzman and G. Thiele, Eds., *Antenna Theory and Design, 2nd ed.* New York: Wiley, 1998.

[9] Y. Hwang, Y. Zhang, G. Zheng, and T. Lo, "Planar inverted F antenna loaded with high permittivity material," *Electronics Lett.*, vol. 31, no. 20, pp. 1710–1712, Sept. 1995.

[10] J. Colburn and Y. Rahmat-Sami, "Patch antennas on externally perforated high dielectric constant substrates," *IEEE Transactions on Antennas and Propagation*, vol. 47, no. 12, pp. 1785–1794, Dec. 1999.

[11] H. Mosallaei and K. Sarabandi, "Magneto-dielectrics in electromagnetics: concept and applications," *IEEE Transactions on Antennas and Propagation*, vol. 52, no. 6, pp. 1558–1567, June 2004.

[12] M. Rad and L. Shafai, "Embedded microstrip patch antenna for structural health monitoring applications," in *Antennas and Propagation Society International Symposium, 2008. AP-S 2008. IEEE*, 5-11 July 2008, pp. 1–4.

[13] S. Basat, K. Lim, J. Laskar, and M. Tentzeris, "Design and modeling of embedded 13.56 MHz RFID antennas," in *Antennas and Propagation Society International Symposium, 2005 IEEE*, vol. 4B, 3-8 July 2005, pp. 64–67.

[14] M. Polivka, M. Svanda, and P. Cerny, "Multiple-arm folded monopole antenna operating extremely close to a conductive plane," in *Microwave Techniques, 2008. COMITE 2008. 14th Conference on*, 23-24 April 2008, pp. 1–5.

[15] J. Wang and J. Winters, "An embedded antenna for mobile DBS," in *Vehicular Technology Conference, 2004. VTC2004-Fall. 2004 IEEE 60th*, vol. 6, 26-29 Sept. 2004, pp. 4092–4095.

[16] S. Rogers, J. Scott, J. Marsh, and D. Lin, "An embedded quad-band WLAN antenna for laptop computers and equivalent circuit model," in *Antennas and Propagation Society International Symposium, 2004. IEEE*, vol. 3, 20-25 June 2004, pp. 2588–2591.

[17] L. J. Chu, "Physical limitations of omni-directional antennas," *J. Appl. Phys.*, vol. 19, no. 64, pp. 1163–1175, Dec. 1948.

[18] R. Azadegan and K. Sarabandi, "A compact planar folded-dipole antenna for wireless applications," in *IEEE Antennas and Propagation Society International Symposium 2003*, June 2003, pp. 439–442.

[19] N. Behdad and K. Sarabandi, "Bandwidth enhancement and further size reduction of a class of miniaturized slot antennas," *IEEE Transactions on Antennas and Propagation*, vol. 52, no. 8, pp. 1928–1935, Aug. 2004.

[20] K. Sarabandi and R. Azadegan, "Design of an efficient miniaturized UHF planar antenna," *IEEE Transactions on Antennas and Propagation*, vol. 51, no. 6, pp. 1270–1276, June 2003.

[21] R. Azadegan and K. Sarabandi, "A novel approach for miniaturization of slot antennas," *IEEE Transactions on Antennas and Propagation*, vol. 51, no. 3, pp. 421–429, Mar. 2003.

[22] J. Galejs, Ed., *Antennas in Inhomogeneous Media*. Pergamon Press, 1969.

[23] J. Galejs, "Admittance of a rectangular slot which is backed by a rectangular cavity," *IEEE Transactions on Antennas and Propagation*, vol. 21, no. 2, pp. 119–126, Mar. 1963.

[24] C. Cockrell, "The input admittance of the rectangular cavity-backed slot antenna," *IEEE Transactions on Antennas and Propagation*, vol. 24, no. 3, pp. 288–294, May 1976.

[25] S. Long, "A mathematical model for the impedance of the cavity-backed slot antenna," *IEEE Transactions on Antennas and Propagation*, vol. 25, no. 6, pp. 829–833, Nov. 1977.

[26] ——, "Experimental study of the impedance of cavity-backed slot antennas," *IEEE Transactions on Antennas and Propagation*, vol. 23, no. 1, pp. 1–7, Jan. 1975.

[27] A. Hadidi and M. Hamid, "Aperture field and circuit parameters of cavity-backed slot radiator," *IEE Proceedings on Antennas, Microwaves, and Propagation*, 1989.

[28] A. T. Adams, "Flush mounted retangular cavity slot antennas - theory and design," *IEEE Transactions on Antennas and Propagation*, vol. 15, no. 3, pp. 342–351, May 1967.

[29] H. P. Moyer and R. A. York, "Active cavity-backed slot antenna using MESFETs," *IEEE Microwave and Guided Wave Letters*, vol. 3, no. 4, pp. 95–97, Apr. 1989.

[30] L. Quan and S. Zhongxiang, "An inverted microstrip-fed cavity-backed slot antenna for circular polarization," *IEEE Antennas and Wireless Propagation Letters*, vol. 1, no. 11, pp. 190–192, 2002.

[31] J. Hirokawa, H. Arai, and N. Goto, "Cavity-backed wide slot antenna," *IEE Proceedings on Antennas, Microwaves, and Propagation*, vol. 136, no. 1, pp. 29–33, Feb. 1989.

[32] A. Roederer, "A log-periodic cavity-backed slot array," *IEEE Transactions on Antennas and Propagation*, vol. 16, no. 6, pp. 756–758, Nov. 1968.

[33] M. R. Crews and S. G. A. Thiele, "On the design of shallow depth T-bar fed slot antennas," *IEEE Transactions on Antennas and Propagation*, vol. 25, no. 6, pp. 833–836, Nov. 1977.

[34] *IE3D Electromagnetic Simulation and Optimization Software*. Zeland Software, Inc.

[35] J. McVay and A. Hoorfar, "Miniaturization of top-loaded monopole antennas using Peano-curves," in *IEEE Radio and Wireless Symposium*, Jan. 2007, pp. 253–256.

[36] A. Buerkle, K. Sarabandi, and H. Mosallaei, "Compact slot and dielectric resonator antenna with dual-resonance, broadband characteristics," in *IEEE Transactions on Antennas and Propagation*, vol. 53, no. 3, Mar. 2005, pp. 1020–1027.

[37] H. Mosallaei and K. Sarabandi, "Antenna miniaturization and bandwidth enhancement using a reactive impedance substrate," *IEEE Transactions on Antennas and Propagation*, vol. 52, no. 9, pp. 2403–2414, Sept. 2004.

[38] K. Buell, H. Mosallaei, and K. Sarabadi, "A substrate for small patch antennas providing tunable miniaturization factors," in *IEEE Transactions on Antennas and Propagation*, vol. 54, no. 1, 2006, pp. 135–146.

[39] D. Horn, "Selection of vehicular antenna configuration and location through use of radiation pattern," in *Vehicular Technology Conference, 1973. 24th IEEE*, vol. 24, Dec. 1973, pp. 45–51.

[40] Z. Novacek, "Radiation of a whip antenna on the car body," in *Radioelektronika, 2007. 17th International Conference*, 24-25 April 2007, pp. 1–4.

[41] S. R. Best, "On the use of scale brass models in HF shipboard communication antenna design," *Antennas and Propagation Magazine, IEEE*, vol. 44, no. 2, pp. 12–23, Apr. 2002.

[42] B. Collins, "Embedding antennas in user equipments," in *Wireless Communications and Networking Conference, 2007.WCNC 2007. IEEE*, 11-15 March 2007, pp. 2334–2337.

[43] S. Ponnapalli, "Design and packaging of antennas for wireless systems," in *Electrical Performance of Electronic Packaging, 1995*, 2-4 Oct. 1995, pp. 157–159.

[44] B. Collins, "Improving the RF performance of clamshell handsets," in *Antenna Technology Small Antennas and Novel Metamaterials, 2006 IEEE International Workshop on*, March 6-8, 2006, pp. 265–268.

[45] C.-M. Su, L.-C. Chou, C.-I. Lin, and K.-L. Wong, "Embedded DTV antenna for laptop application," in *Antennas and Propagation Society International Symposium, 2005 IEEE*, vol. 4B, 3-8 July 2005, pp. 68–7.

[46] J. Wang and J. Winters, "An embedded antenna for mobile DBS," in *Vehicular Technology Conference, 2004. VTC2004-Fall. 2004 IEEE 60th*, vol. 6, 26-29 Sept. 2004, pp. 4092–4095.

[47] J. Karanik, "Embedded antennas," in *Long Island Systems, Applications and Technology, 2005. IEEE Conference*, 6 May, 2005, pp. 26–31.

[48] A. Vallecchi and G. Gentili, "Investigation of microstrip-fed slot antennas backed by shallow cavities," in *Antennas and Propagation Society International Symposium, 2005 IEEE*, vol. 3B, 3-8 July 2005, pp. 373–376.

[49] C. X. Lindberg, "A shallow-cavity UHF crossed-slot antenna," *IEEE Transactions on Antennas and Propagation*, vol. 17, no. 5, pp. 558–563, Sept. 1969.

[50] Solidica, http://www.solidica.com.

[51] N. Behdad and K. Sarabandi, "A wide-band slot antenna design employing a fictitious short circuit concept," *IEEE Transactions on Antennas and Propagation*, vol. 52, no. 1, pp. 475–482, Jan. 2005.

[52] K. Bobier, J. Wells, and M. Dapper, "Enhanced unattended ground sensor system communications," in *MILCOM Proceedings*, vol. 1, Oct. 2002, pp. 282–289.

[53] K. Elgort, S. Komaromy, J.Madden, and A. Taylor, "US army employment of unattended ground sensors," in *IEEE Symposium on Systems and Information Engineering Design*, Apr. 2005, pp. 263–269.

[54] E. Soliman, M. Ibrahim, and A. Abdelmageed, "Dual-polarized omnidirectional planar slot antenna for WLAN applications," *IEEE Transactions on Antennas and Propagation*, vol. 53, no. 9, pp. 3093–3097, Sept. 2005.

[55] R. Li, B. Pan, J. Laskar, and M. M. Tentzeris, "A compact broadband planar antenna for GPS, DCS-1800, IMT-2000, and WLAN applications," *IEEE Antennas Propag. Lett.*, vol. 53, pp. 25–27, 2007.

[56] F. Hsiao and K. Wong, "Omnidirectional planar folded dipole antenna," *IEEE Transactions on Antennas and Propagation*, vol. 52, no. 7, pp. 1898–1902, July 2004.

[57] C. Lin, L. Kuo, and H. Chuang, "A horizontally polarized omnidirectional printed antenna for WLAN applications," in *IEEE Antennas and Propagation Society International Symposium 2005*, vol. 54, no. 11, July 2005, pp. 491–494.

[58] N. Herscovici, Z. Sipus, and P. Kildal, "The cylindrical omnidirectional patch antenna," *IEEE Transactions on Antennas and Propagation*, vol. 49, no. 12, pp. 1746–1753, Dec. 2001.

[59] S. Xu and X. Wu, "A millimeter-wave omnidirectional dielectric rod metallic grating antenna," *IEEE Transactions on Antennas and Propagation*, vol. 44, no. 1, pp. 74–79, Jan. 1996.

[60] R. Zentner, Z. Sipus, N. Herscovici, and J. Bartolic, "Omnidirectional stacked patch antenna printed on circular cylindrical structure," in *IEEE Antennas and Propagation Society International Symposium 2002*, vol. 12, June 2002, pp. 272–275.

[61] L. Freytag, E. Pointereau, and B. Jecko, "Omnidirectional dielectric electromagnetic band gap antenna for base station of wireless network," in *IEEE Antennas and Propagation Society International Symposium 2004*, vol. 1, June 2004, pp. 815–818.

[62] B. Guo, J. Fang, and W. Wang, "The study of the radiation characteristic for cavity backed antennas," *Electronics Lett.*, pp. 236–237, 1999.

[63] S. Dey, C. Aanandan, P. Mohanan, and K. Nair, "Analysis of cavity backed printed dipoles," in *IEEE Antennas and Propagation Society International Symposium 1994*, vol. 30, no. 3, Feb. 1994, pp. 173–174.

[64] M. Li, M. K. Hummer, and K. Chang, "Theoretical and experimental study of the input impedance of the cylindrical cavity-backed rectangular slot antennas," *IEEE Transactions on Antennas and Propagation*, vol. 39, no. 8, pp. 1158–1166, Aug. 1991.

[65] M. Zheng, P. Hall, Q. Chen, and V. Fusco, "Cavity-backed active slot loop antenna," in *IEEE Antennas and Propagation Society International Symposium 1998*, vol. 3, June 1998, pp. 1620–1623.

[66] D. Liao and K. Sarabandi, "Optimization of low-profile antennas for applications in unattended ground sensor networks," in *IEEE Antennas and Propagation Society International Symposium 2006*, July 2006, pp. 783–786.

[67] H. Chen, W. Chen, Y. Cheng, and Y. Lin, "Dualband monopole antenna," in *IEEE Antennas and Propagation Society International Symposium 2003*, June 2003, pp. 48–51.

[68] Y. Lin, C. Lin, and P. Hall, "A miniature dielectric loaded monopole antenna for 2.4/5 ghz wlan applications," *IEEE Microwave and Wireless Components Lett.*, vol. 16, no. 11, pp. 591–593, Nov. 2006.

[69] A. Pomerleau and M. Fournier, "Inductively loaded monopole antenna," in *IEEE Antennas and Propagation Society International Symposium 1972*, Dec. 1972, pp. 81–84.

[70] J. C. Harrison., "Monopole with inductive loading," *IEEE Transactions on Antennas and Propagation*, vol. 11, no. 4, pp. 394–400, July 1963.

[71] J. McLean, H. Foltz, and G. Crook, "Broadband, robust, low profile monopole incorporating top loading, dielectric loading, and a distributed capacitive feed mechanism," in *IEEE Antennas and Propagation Society International Symposium 1999*, July 1999, pp. 1562–1565.

[72] S. Tokumaru, "Multiplates: Low profile antennas," in *IEEE Antennas and Propagation Society International Symposium 1976*, vol. 14, Oct. 1976, pp. 379–382.

[73] N. Herscovivi and E. Dziadek, "Omnidirectional antennas for wireless communication," in *IEEE Antennas and Propagation Society International Symposium 1999*, vol. 1, July 1999, pp. 556–559.

[74] T. Noro and Y. Kazama, "Low profile and wide bandwidth characteristics of top loaded monopole antenna with shorting post," in *IEEE International Workshop on Antenna Technology Small Antennas and Novel Metamaterials*, Mar. 2006, pp. 108–111.

[75] C. Delaveaud, P. Levegue, and B. Jecko, "Small-sized low-profile antenna to replace monopole antennas," *Electron. Lett.*, vol. 34, no. 8, pp. 716–717, Apr. 1998.

[76] G. Goubau, "Multielement monopole antennas," in *Proc. Workshop on Electrically Small Antennas ECOM, Ft. Monmouth, NJ*, May 1976, pp. 63–67.

[77] C. Ravipati and S. Best, "The Goubau multi element monopole antenna - revisited," in *IEEE Antennas and Propagation Society International Symposium 2007*, June 2007, pp. 233–236.

[78] F. Yang and Y. Rahmat-Samii, "Reflection phase characterizations of the EBG ground plane for low profile wire antenna applications," *IEEE Transactions on Antennas and Propagation*, vol. 51, no. 10, pp. 2691–2703, Oct. 2003.

[79] N. Behdad and K. Sarabandi, "Bandwidth enhancement and further size reduction of a class of miniaturized slot antennas," *IEEE Transactions on Antennas and Propagation*, vol. 52, no. 8, pp. 1928–1935, Aug. 2004.

[80] T. W. Ban, B. Y. Cho, W. Choi, and H.-S. Cho, "On the capacity of a DS/CDMA system with automatic on-off switching repeaters," in *Communications, 2001. ICC 2001. IEEE International Conference on*, vol. 3, 11-14 June 2001, pp. 780–784.

[81] K. Hiltunen, "Using RF repeaters to improve WCDMA HSDPA coverage and capacity inside buildings," in *Personal, Indoor and Mobile Radio Communications, 2006 IEEE 17th International Symposium on*, 11-14 Sept. 2006, pp. 1–5.

[82] R. Jakubowski, "A new generation of high-power cellular repeaters," in *Vehicular Technology Conference, 1990 IEEE 40th*, 6-9 May 1990, pp. 24–28.

[83] M. Lee, B. Keum, Y. Son, J.-W. Kim, and H. S. Lee, "A new low-complex interference cancellation scheme for WCDMA indoor repeaters," in *Computational Technologies in Electrical and Electronics Engineering, 2008. SIBIRCON 2008. IEEE Region 8 International Conference on*, 21-25 July 2008, pp. 457–462.

[84] A. S. M. Marzuki, A. R. Rahim, B. Mohmd, K. Khalil, A. Naemat, and A. Tee, "Antenna isolation considerations in WCDMA repeater deployment," in *RF and Microwave Conference, 2006. RFM 2006. International*, 12-14 Sept. 2006, pp. 347–350.

[85] A. H. Naemat, A. Tee, A. S. M. Marzuki, B. Mohmd, K. Khalil, and A. R. A. Rahim, "Achieving optimum in-building coverage of 3G network in malaysia," in *RF and Microwave Conference, 2006. RFM 2006. International*, 12-14 Sept. 2006, pp. 343–346.

[86] R. Isberg, "Radio communication in subways and mines through repeater amplifiers and leaky transmission lines," in *Vehicular Technology Conference, 1978. 28th IEEE*, vol. 28, 22-24 March 1978, pp. 248–254.

[87] C. Cho, H. Zhang, and M. Nakagawa, "A UWB repeater with a short relaying-delay for range extension," in *Wireless Communications and Networking Conference, 2004. WCNC. 2004 IEEE*, vol. 2, 21-25 March 2004, pp. 1154–1158.

[88] G. Sharma and S. Srinivasan, "Diversity gain using a repeater in a wireless personal area network," in *Vehicular Technology Conference, 2005. VTC 2005-Spring. 2005 IEEE 61st*, vol. 3, 30 May-1 June 2005, pp. 1519–1522.

[89] S. Saunders, M. Kennett, E. Montiel, and B. Evans, "Repeater requirements for Pan-European satellite digital broadcast services," in *Antennas and Propagation, 2003.*

(ICAP 2003). Twelfth International Conference on (Conf. Publ. No. 491), vol. 1, 31 March-3 April 2003, pp. 123–127.

[90] S. Heinen, "Integrated transceivers for digital cordless applications," in *Bipolar/BiCMOS Circuits and Technology Meeting, 2000. Proceedings of the 2000*, 24-26 Sept. 2000, pp. 44–51.

[91] L. Khuon, E. Huang, C. Sodini, and G. Wornell, "Integrated transceiver arrays for multiple antenna systems," in *Vehicular Technology Conference, 2005. VTC 2005-Spring. 2005 IEEE 61st*, vol. 2, 30 May-1 June 2005, pp. 892–895.

[92] J. Kim and R. Harjani, "An ISM band CMOS integrated transceiver design for wireless telemetry system," in *Circuits and Systems, 2001. ISCAS 2001. The 2001 IEEE International Symposium on*, vol. 4, 6-9 May 2001, pp. 694–697.

[93] I. Kwon, Y. Eo, S.-S. Song, K. Choi, H. Lee, and K. Lee, "A fully integrated 2.4 GHz CMOS RF transceiver for IEEE 802.15.4," in *Radio Frequency Integrated Circuits (RFIC) Symposium, 2006 IEEE*, 11-13 June 2006, pp. 4–7.

[94] K. Lim, A. Obatoyinbo, A. Sutono, S. Chakraborty, C.-H. Lee, E. Gebara, A. Raghavan, and J. Laskar, "A highly integrated transceiver module for 5.8 GHz OFDM communication system using multi-layer packaging technology," in *Microwave Symposium Digest, 2001 IEEE MTT-S International*, vol. 3, 20-25 May 2001, pp. 1739–1742.

[95] H. Okabe, T. Ido, and T. Endo, "Compact radio system module for triple-band GSM cellular phones," in *Radio Frequency integrated Circuits (RFIC) Symposium, 2005. Digest of Papers. 2005 IEEE*, 12-14 June 2005, pp. 273–276.

[96] C. Woo, A. Podell, R. Benton, D. Fisher, and J. Wachsman, "A fully integrated transceiver chip for the 900 MHz communication bands," in *Gallium Arsenide Integrated Circuit (GaAs IC) Symposium, 1992. Technical Digest 1992., 14th Annual IEEE*, 4-7 Oct. 1992, pp. 143–146.

[97] M. Sanduleanu and J. Long, "CMOS integrated transceivers for 60GHz UWB communication," in *Ultra-Wideband, 2007. ICUWB 2007. IEEE International Conference on*, 24-26 Sept. 2007, pp. 508–513.

[98] H. Abe, M. Sato, K. Itoi, S. Kawai, T. Tanaka, T. Hayashi, Y. Saitoh, and T. Ito, "Microwave operation of on-chip antenna embedded in WL-CSP [RFID applications]," in *Antenna Technology: Small Antennas and Novel Metamaterials, 2005. IWAT 2005. IEEE International Workshop on*, 7-9 March 2005, pp. 147–150.

[99] M. R. N. Ahmadi, S. Safavi-Naeini, and L. Zhu, "An efficient CMOS on-chip antenna structure for system in package transceiver applications," in *Radio and Wireless Symposium, 2007 IEEE*, 9-11 Jan. 2007, pp. 487–490.

[100] F. Aquilino, F. Della Corte, M. Merenda, and F. Zito, "Fully-integrated wireless temperature sensor with on-chip antenna," in *Sensors, 2008 IEEE*, 26-29 Oct. 2008, pp. 760–763.

[101] A. Babakhani, X. Guan, A. Komijani, A. Natarajan, and A. Hajimiri, "A 77GHz 4-element phased array receiver with on-chip dipole antennas in silicon," in *Solid-State Circuits Conference, 2006. ISSCC 2006. Digest of Technical Papers. IEEE International*, 6-9 Feb. 2006, pp. 629–638.

[102] P. Bijumon, Y. Antar, A. Freundorfer, and M. Sayer, "Integrated dielectric resonator antennas for system on-chip applications," in *Microelectronics, 2007. ICM 2007. Internatonal Conference on*, 29-31 Dec. 2007, pp. 275–278.

[103] R. van Dijk, A. Neto, J. Akkermans, and J. Mills, "EBG-based 60 GHz on-chip antenna in passive silicon," in *Microwave Conference, 2008. EuMC 2008. 38th European*, 27-31 Oct. 2008, pp. 682–685.

[104] X. Guo, R. Li, and K. O, "Design guidelines for reducing the impact of metal interference structures on the performance on-chip antennas," in *Antennas and Propagation Society International Symposium, 2003. IEEE*, vol. 1, 22-27 June 2003, pp. 606–609.

[105] J.-J. Lin, A. Sugavanam, L. Gao, J. Brewer, and K. O, "On-wafer measurement setups for on-chip antennas fabricated on silicon substrates," in *ARFTG Microwave Measurements Conference, Fall 2004. 64th*, 2-3 Dec. 2004, pp. 221–225.

[106] M. Nezhad Ahamdi and S. Safavi-Naeini, "On-chip antennas for 24, 60, and 77GHz single package transceivers on low resistivity silicon substrate," in *Antennas and Propagation International Symposium, 2007 IEEE*, 9-15 June 2007, pp. 5059–5062.

[107] N. Varanasi, B. Jung, and D. Peroulis, "On-chip bond-wire antennas on CMOS-grade silicon substrates," in *Antennas and Propagation Society International Symposium, 2008. AP-S 2008. IEEE*, 5-11 July 2008, pp. 1–4.

[108] H. Yordanov and P. Russer, "Integrated on-chip antennas for chip-to-chip communication," in *Antennas and Propagation Society International Symposium, 2008. AP-S 2008. IEEE*, 5-11 July 2008, pp. 1–4.

[109] S. Padhi, N. Karmakar, C. Law, and S. Aditya, "A dual polarized aperture coupled circular patch antenna using a C-shaped coupling slot," *IEEE Transactions on Antennas and Propagation*, vol. 51, no. 12, pp. 3295–3298, Dec. 2003.

[110] R. Li, G. DeJean, M. Tentzeris, and J. Laskar, "Integrable miniaturized folded antennas for RFID applications," in *IEEE Antennas and Propagation Society International Symposium 2004*, June 2005, pp. 1431–1432.

[111] N. Behdad and K. Sarabandi, "Dual-band reconfigurable antenna with a very wide tunability range," *IEEE Transactions on Antennas and Propagation*, vol. 54, no. 2, pp. 409–416, Feb. 2006.

[112] S. Nikolaou, R. Bairavasubramanian, C. Lugo, Jr., I. Carrasquilli, D. Thompson, G. Ponchack, J. Papapolymerou, and M. Tentzeris, "Pattern and frequency reconfigurable annular slot antenna using PIN diodes," *IEEE Transactions on Antennas and Propagation*, vol. 54, no. 2, pp. 439–448, Feb. 2006.

[113] M. Fries, M. Grani, and R. Vahldieck, "Pattern and frequency reconfigurable annular slot antenna using PIN diodes," *IEEE Transactions on Antennas and Propagation*, vol. 13, no. 11, pp. 490–492, Nov. 2003.

[114] D. Peroulis, K. Sarabandi, and L. Katehi, "Design of reconfigurable slot antennas," *IEEE Transactions on Antennas and Propagation*, vol. 53, no. 2, pp. 645–654, Feb. 2006.

[115] N. Behdad and K. Sarabandi, "A varactor-tuned dual-band slot antenna," *IEEE Transactions on Antennas and Propagation*, vol. 54, no. 2, pp. 401–408, Feb. 2006.

[116] H. Wheeler, "Fundamental limitations of small antennas," *Proceedings of the IRE*, vol. 35, no. 12, pp. 1479–1484, Dec. 1947.